AD-A264 333

②

IENTATION PAGE

Form Approved
OMB No. 0704-0188

stimated to average 1 hour per response, including the time for reviewing instructions, searching existing data sources, and reviewing the collection of information. Send comments regarding this burden estimate or any other aspect of this this burden, to Washington Headquarters Services, Directorate for Information Operations and Reports, 1215 Jefferson Davis Highway, Suite 1204, Arlington, VA the Office of Management and Budget, Paperwork Reduction Project (0704-0188), Washington, DC 20503.

1. AGENCY USE ONLY *(Leave blank)*	**2. REPORT DATE** November 1992	**3. REPORT TYPE AND DATES COVERED** Final - February 1990 - May 1992

4. TITLE AND SUBTITLE
"Simulation, Characterization and Control of Forced Unsteady Viscous Flows Using Navier-Stokes Equations."

5. FUNDING NUMBERS
AFOSR 90-0249
2307/A3

6. AUTHOR(S)
K.N. Ghia and U. Ghia

AFOSR-TR

7. PERFORMING ORGANIZATION NAME(S) AND ADDRESS(ES)
University of Cincinnati
Department of Aerospace Engg. & Engineering Mechanics
Department of Mechanical, Industrial and Nuclear Engg.
Cincinnati, OH 45221

8. PERFORMING ORGANIZATION REPORT NUMBER
AFL Report No.
92-11-78

9. SPONSORING/MONITORING AGENCY NAME(S) AND ADDRESS(ES)
Air Force Office of Scientific Research/NA
Aerospace Sciences
Building 410
Bolling Air Force Base, DC 20332-6648

10. SPONSORING/MONITORING AGENCY REPORT NUMBER
AFOSR-
90-0249

DTIC
ELECTE
MAY 1 4 1993
S C D

11. SUPPLEMENTARY NOTES

12a. DISTRIBUTION/AVAILABILITY STATEMENT
Distribution of this report is unlimited.

93 5 13 047

93-10750

13. ABSTRACT *(Maximum 200 words)*

A two-and-a-quarter-year multi-tasked research project was pursued by the present investigators to study dynamic stall phenomenon under AFOSR sponsorship between February 1990 - May 1992.

The major objective of this study was to predict and control the dynamic stall phenomenon in 2-D and 3-D flows. In the process of achieving these objectives, significant effort was directed towards developing mathematical models and the corresponding computational methods which were made available to interested researchers and organizations involved in computational fluid dynamics (CFD) research. The analyses developed included a two-dimensional Navier-Stokes (NS) analysis for a general body undergoing arbitrary three-degree-of-freedom maneuvers; detailed results are provided for this class of flows. For enhancement of accuracy and efficiency, an adaptive-grid time-accurate flow solution technique has been developed to enable improved resolution of the various length scales in a vortex-dominated unsteady flow. A multi-block grid generation analysis is developed for a 3-D rectangular planform wing. For the corresponding flow analysis using velocity-vorticity variables and direct-solution philosophy, the difficulties experienced were clearly discussed in the annual report submitted a year ago in November 1991. This 3-D flow analysis was therefore temporarily set aside. It will be pursued further in a subsequent grant, and the progress made on it will be reported in a forthcoming annual report for that grant. In the current grant, the study of 3-D flows was continued, using an iterative solution methodology. Hence, a 3-D (Continued on attached sheet)

14. SUBJECT TERMS
Unsteady Flow
Separation
Dynamic Stall
Wing Rock
Vortex Burst
NACA 0015 Airfoil
Slender Delta Wing
2-D & 3-D Flows
Flow Control
Navier-Stokes Equations
Implicit/Iterative Techniques

15. NUMBER OF PAGES
141

16. PRICE CODE

17. SECURITY CLASSIFICATION OF REPORT Unclassified	**18. SECURITY CLASSIFICATION OF THIS PAGE** Unclassified	**19. SECURITY CLASSIFICATION OF ABSTRACT** Unclassified	**20. LIMITATION OF ABSTRACT** UL

unsteady Navier-Stokes analysis, again using velocity-vorticity variables, and an iterative solution technique with multi-grid acceleration have been developed. The procedure is validated by applying it to the model problem of shear-driven flow in a cavity for which experimental as well as other numerical results are available. In a parallel effort, the existing unsteady thin-layer NS analysis and CFL3D software were modified and flow past a delta wing at high angle of attack was studied. This is reported separately in a M.S. Thesis that has been completed on this work.

For the 2-D dynamic stall phenomenon, the mechanism responsible for the leading-edge stall is finally understood. An effective modulated suction/injection control strategy is devised to significantly delay the formation of the energetic stall vortex. The various analyses developed have provided further insight into the dynamic stall phenomenon; additional work is continued for 2-D flows to understand further the role of separation and, for 3-D flows, to further develop and validate the analysis for rectangular and delta wings.

ABSTRACT

A two-and-a-quarter-year multi-tasked research project was pursued by the present investigators to study dynamic stall phenomenon under AFOSR sponsorship between February 1990 - May 1992.

The major objective of this study was to predict and control the dynamic stall phenomenon in 2-D and 3-D flows. In the process of achieving these objectives, significant effort was directed towards developing mathematical models and the corresponding computational methods which were made available to interested researchers and organizations involved in computational fluid dynamics (CFD) research. The analyses developed included a two-dimensional Navier-Stokes (NS) analysis for a general body undergoing arbitrary three-degree-of-freedom maneuvers; detailed results are provided for this class of flows. For enhancement of accuracy and efficiency, an adaptive-grid time-accurate flow solution technique has been developed to enable improved resolution of the various length scales in a vortex-dominated unsteady flow. A multi-block grid generation analysis is developed for a 3-D rectangular planform wing. For the corresponding flow analysis using velocity-vorticity variables and direct-solution philosophy, the difficulties experienced were clearly discussed in the annual report submitted a year ago in November 1991. This 3-D flow analysis was therefore temporarily set aside. It will be pursued further in a subsequent grant, and the progress made on it will be reported in a forthcoming annual report for that grant. In the current grant, the study of 3-D flows was continued, using an iterative solution methodology. Hence, a 3-D unsteady Navier-Stokes analysis, again using velocity-vorticity variables, and an iterative solution technique with multi-grid acceleration have been developed. The procedure is validated by applying it to the model problem of shear-driven flow in a cavity for which experimental as well as other numerical results are available. In a parallel effort, the existing unsteady thin-layer NS analysis and CFL3D software were modified and flow past a delta wing at high angle of attack was studied. This is reported separately in a M.S. Thesis that has been completed

on this work.

For the 2-D dynamic stall phenomenon, the mechanism responsible for the leading-edge stall is finally understood. An effective modulated suction/injection control strategy is devised to significantly delay the formation of the energetic stall vortex. The various analyses developed have provided further insight into the dynamic stall phenomenon; additional work is continued for 2-D flows to understand further the role of separation and, for 3-D flows, to further develop and validate the analysis for rectangular and delta wings.

Contents

List of Tables

List of Figures

Section 1

OBJECTIVES

An analytical-numerical study was pursued by the present investigators under AFSOR sponsorship during February 1990 - May 1992. The primary objectives were: (i) To characterize the unsteady separation accompanying dynamic stall of an airfoil in constant-pitch-rate motion; (ii) To develop a flow-control strategy to optimize the instantaneous maximum lift and the sustained lift; (iii) To develop 3-D unsteady flow simulation capability to examine flow past a rectangular planform wing as well as a delta wing. In connection with the last primary objective, the secondary objectives of the development of a three-dimensional unsteady Navier-Stokes analysis using iterative schemes, as well as computational efficiency and management and post-processing of large data bases become very significant.

A multi-tasked research effort was undertaken to achieve these objectives. A physically consistent 2-D unsteady flow analysis for maneuvering airfoils is developed in theory and direct-simulation code, using the concept of circulation in a vorticity-based formulation. An unsteady flow-control strategy is developed for effective management of the associated lift. The analysis formulated for studying 3-D unsteady flow is also based on vorticity and velocity, but uses an iterative technique. In addition, to accelerate convergence, an efficient multi-grid algorithm is developed for the velocity problem emerging from this formulation. The issue of efficiency, at least for 2-D flows, is further addressed by developing a temporally adapting grid in which the adaption is based on the evolving flow solution. This adaptive grid technique has the potential to resolve very fine scales that are critical in the study of dynamic stall.

The significant accomplishments made toward achieving the above-stated objectives are briefly described next.

Section 2

DESCRIPTION OF SIGNIFICANT ACCOMPLISHMENTS

All of the areas of research pursued and the progress, as well as the specific achievements, made in these studies during the 27-month grant period are briefly summarized in the following sections.

2.A 2-D Dynamic Stall and Its Control

2.A.1 Introduction

The realization of supermaneuverable flight necessitates the use of unsteady non-equilibrium flow analyses and examination of a more comprehensive parameter envelope which can capture significant time-dependent effects. The numerous complex flow phenomena and interactions which might occur during a supermaneuver in the high-alpha (generally between 30° and 90°) flight regime are highly nonlinear primarily due to flow separation, presence of vortex dominated flows and unsteadiness. As a consequence, there is a strong coupling between the prevailing aerodynamics and flight dynamics, sometimes leading to chaotic flow and loss of control of the aircraft due to tail spin. To improve the maneuverability of high-performance military aircraft at very high angle of attack, researchers are currently developing analytical and experimental design tools that can take full advantage of unsteady aerodynamics. When achieved by operating in the post-stall flight regime, supermaneuverability permits improved combat capability.

The initiation of a high-alpha maneuver may involve large-amplitude deflections of control surfaces or rapid pitch-up motions of the lifting surface itself. During this post-stall maneuver, instead of experiencing massive flow separation and the resulting loss of lift, the lifting surface develops an energetic dynamic-stall vortex, which temporarily leads to a significant increase in lift and drag forces. Thus, during the time that the dynamic-stall vortex is created on the suction surface and convects over it, the flow field is characterized by a number of dominant flow features which include growth of boundary layer, separation, unsteadiness, primary and secondary shear layer instability, unsteady separation, shock/boundary-layer and inviscid-viscid interactions, and vortex-vortex and vortex-surface interactions. Thus, the dynamic stall event is richly endowed with many basic fluid mechanics phenomena. The understanding and control of this event is important not only for supermaneuverable aircrafts, but also for helicopter rotor blades, compressor blades, wind turbines, etc.

Towards the development of a supermaneuverable flight capability, Lang and Francis (1985) had articulated many of the research problems that are currently being pursued by researchers. Many of the concepts discussed by them are now being tested in the first international X-plane, namely, the X-31, known officially as the Enhanced Flight Maneuverability Demonstrator; see Lerner (1991). This is the first aircraft which has successfully maneuvered in the post-stall regime, thereby making this liability an asset. Thus, any insight gained in understanding the dynamics of the post-stall regime could be very valuable in improving the performance and flight envelope of this type of aircraft.

Since April 1990, there have been three major workshops/conferences, where the research issues as well as the results of the studies in the area of post-stall maneuvers have been discussed. References [A.2, A.6 and A.16] provide sources where current work is published and the reader would benefit immensely from them. In light of these references, together with recent excellent review articles by Carr (1985), Helin (1989) and Visbal (1990), it is decided to not include a review of the literature in the present paper.

The present authors have been studying forced unsteady separated flows, using the NACA 0015 airfoil for some time. Specifically, K. Ghia, Osswald and U. Ghia (1990) provided, for very low Re, results that very vividly showed four stages, as classified by Walker (1992), that describe the dynamic stall event. These are:

i. **triggering phase**, in which flow separation occurs near the leading edge (LE) on the suction surface due to adverse pressure gradient;
ii. **separation,** in which vorticity accumulates in the surface layer and the onset of interaction with the outer fluid is about to occur;
iii. **strong interaction**, in which a vorticity plane erupts; and finally,
iv. **inviscid interaction phase**, in which the dynamic-stall vortex is formed due to roll-up of the free shear layer, which entrains fluid from the boundary layer.

The details of the analysis were given by Osswald, K. Ghia and U. Ghia (1990). Subsequently, K. Ghia, Yang, Osswald and U. Ghia (1991) provided the results for higher-Re flows by treating the nonlinear convection terms using a third-order accurate biased upwind differencing scheme, while still retaining the central differencing scheme for all other spatial derivatives. Thereafter, K. Ghia, Yang, Osswald and U. Ghia (1992) demonstrated the suppression of the dynamic-stall vortex using an active control strategy of suction/injection. In addition, K. Ghia, Yang, U. Ghia and Osswald (1992) successfully studied the dynamic-stall phenomenon using a modified NACA 0012 airfoil undergoing sinusoidal oscillations. The primary objective in that investigation was to simulate and analyze the Grand Challenge Problem posed by Carr (1990). The experimental data for this problem was that of McAllister and Carr (1979). Further, Osswald, K. Ghia and U. Ghia (1992) extended the analysis to provide a more accurate far-field boundary condition, which required the coupling of viscous circulation $\Gamma(t)$ with the original analysis of the authors, Ref. [A.13], which used $(\bar{\omega}_I, \psi_I^D)$, thereby arriving at a $(\bar{\omega}_I, \psi_I^D, \Gamma(t))$ formulation. In addition, some results were provided for Re = 45,000 with constant pitch-rate $\dot{\alpha}^+ = 0.2$, and Re = 52000 with $\dot{\alpha}^+ = 0.072$.

The primary objective of the present study is to extend the analysis of K. Ghia, Yang, Osswald and U. Ghia (1992) to provide an accurate far-field boundary condition by correctly implementing the prevailing viscous circulation there. Although this analysis parallels that of Osswald, K. Ghia and U. Ghia (1992), it has some significant differences in the way the mathematical formulation is set up and particularly in the details of the numerical procedure. In addition, it is also the goal of this study to analyze the simulation results more fully in light of the available experimental data or numerical results, so as to assess the overall 2-D $(\bar{\omega}_I, \psi_I^D, \Gamma(t))$ formulation, where $\Gamma(t)$ is the viscous circulation at infinity.

2.A.2 Mathematical Formulation

The time-dependent flow around a maneuvering airfoil is governed by the unsteady Navier-Stokes (NS) equations. The selection of the specific forms of these nonlinear coupled, partial differential equations used in the present work is based primarily on two factors, namely, (i) dependent variables, and (ii) reference frame.

On the Choice of Dependent Variables

K. Ghia, Hankey and Hodge (1977) used a regular grid and solved the primitive-variable form of the NS equations in which the continuity equation was satisfied using the Poisson equation for pressure. Osswald (1981) examined various 2-D formulations of the NS equations and concluded that the 2-D primitive-variable formulation, with Poisson equation for pressure, should be discretized using a staggered grid, rather than a regular grid, if the discrete equations are to be exactly consistent with the continuous equations. U. Ghia and K. Ghia (1987) had reviewed various NS analyses for 3-D flows; their study included:

i. velocity-pressure $(\bar{V}, p)$,
ii. velocity-vorticity $(\bar{V}, \bar{\omega})$ and
iii. vector-potential-vorticity $(\bar{A}, \bar{\omega})$ formulations.

Osswald, K. Ghia and U. Ghia (1987) clarified further that, although primitive-variable formulations are widely used due to their popularity in compressible-flow analyses, the velocity-vorticity formulation is equally competitive and perhaps more advantageous because it directly provides the vorticity which is the most relevant quantity in the flow. In addition, it was pointed out that the $(\bar{V}, \bar{\omega})$ formulation leads to a natural decoupling of the governing equations, since the spin dynamics of a fluid particle governed by the vorticity-transport problem can be decoupled from the translational kinematics of the fluid particle represented by the elliptic velocity problem. This is not the case for the primitive-variable formulation. It was also pointed out that a careful analysis of the $(\bar{V}, \bar{\omega})$ formulation could reduce its computational requirements to match those of the $(\bar{V}, p)$ formulation. Finally, it was pointed out that the vector-potential-vorticity formulation required specification of a non-physical boundary condition to correctly set up the problem and that this poses numerical difficulties. Huang, U. Ghia and K. Ghia (1992) have revisited this issue and have provided some additional details. Gatski (1991) as well as Gresho (1991) have also reviewed the various NS formulations and have provided some insight into the selection process for the dependent variables.

On the selection of Reference Frame

Even for maneuvering bodies, it is possible to work with an inertial reference frame, with boundary-aligned coordinates being computed at every instant of time to provide for the body motion. Chyu (1981) as well as Salari and Roache (1990) have provided analyses using an inertial reference frame. The major advantage with this approach is that the far-field boundary conditions remain undisturbed. On the other hand, Mehta (1977), Sankar and Tassa (1980), Visbal and Shang (1989) and the present authors have elected to work with the body-fixed non-inertial reference frame. In this approach, although the grid remains undistorted, the far-field boundary conditions require special attention. In the present study of 2-D forced unsteady separated flow, the $(\bar{V},\bar{\omega})$ formulation is used in generalized coordinates in the body-fixed non-inertial reference frame. Osswald, K. Ghia and U. Ghia (1990) have shown that, for the $(\bar{V},\bar{\omega})$ formulation with divergence and curl operators expressed in the generalized-coordinate non-inertial reference frame, the inertial vorticity diffuses as for the case of a fixed body, but advects with apparent velocity rather than with inertial velocity. Thus, except for the appearance of the apparent velocity, the velocity-vorticity formulation of the unsteady NS equations is "nearly" form-invariant under a generalized non-inertial coordinate transformation. This offers a significant advantage, in that it leads to a unified algorithm for both non-maneuvering and maneuvering body flows. Thus, in the present study for 2-D flow past a maneuvering body, the $(\psi,\bar{\omega})$ formulation is used in a body-fixed non-inertial reference frame. This form has been shown by Osswald, K. Ghia, and U. Ghia (1988) to be equivalent to the $(\bar{V},\bar{\omega})$ formulation, but it is computationally more efficient. Speziale (1987) had also shown that, for the special case of rotation, the $(\bar{V},\bar{\omega})$ formulation is form-invariant and that, under this condition, non-inertial effects will enter the solution only through the initial and boundary conditions.

Governing Differential Equations

An arbitrary maneuver can be completely defined by specifying the trajectory $\bar{r}_{B/I}(t)$ of some point B fixed on the body, (see Fig. A.1), with respect to an inertial observer, together with the specification of the instantaneous angular velocity $\bar{\Omega}_B(t)$ of the body.

Kinematically, the translational velocity of the origin B of the body-fixed frame is then $\bar{V}_{B/I}(t) = d(\bar{r}_{B/I})/dt$, and the translational acceleration is $\bar{a}_{B/I}(t) = d^2(\bar{r}_{B/I})/dt^2$, while the angular acceleration is $\bar{\alpha}_B(t) = d(\bar{\Omega}_B)/dt$. In the present analysis, these functions, which define a specific maneuver, are assumed to be explicitly prescribed functions of time, and will be given in a later sub-section.

For an inertial reference frame, the unsteady incompressible Navier-Stokes equations are given in terms of the derived variables ($\bar{V}_I, \bar{\omega}_I$) as

Continuity Equation and Kinematic Definition of Vorticity :

$$\nabla_I \cdot \bar{V}_I = 0\,, \tag{A.1}$$

$$\nabla_I \times \bar{V}_I = \bar{\omega}_I\,. \tag{A.2}$$

Vorticity-Transport Equation :

$$\frac{\partial \bar{\omega}_I}{\partial t} + \nabla_I \times (\bar{\omega}_I \times \bar{V}_I) + \frac{1}{Re}(\nabla_I \times \nabla_I \times \bar{\omega}_I) = 0\,, \tag{A.3}$$

where $Re = \frac{cU_\infty}{\nu}$ such that U_∞ is the reference free-stream velocity and c is the airfoil chord length. Also, the subscript I on ∇_I denotes that the implied spatial differentiation is with respect to inertial coordinates. The transformation of Eqs. (A.1-A.3) to a generalized coordinate non-inertial body-fixed reference frame, as carried out by Osswald, K. Ghia and U. Ghia (1990), leads to the following form:

Continuity Equation and Kinematic Definition of Vorticity :

$$\nabla \cdot \bar{V}_I = 0\,, \tag{A.4}$$

$$\nabla \times \bar{V}_I = \bar{\omega}_I\,. \tag{A.5}$$

Vorticity-Transport Equation :

$$\frac{\partial \bar{\omega}_I}{\partial t} + \nabla \times (\bar{\omega}_I \times \bar{V}) + \frac{1}{Re}(\nabla \times \nabla \times \bar{\omega}_I) = 0\,, \tag{A.6}$$

where all divergence and curl operators are with respect to the generalized-coordinate non-inertial reference frame, the apparent velocity $\bar{V}$ is kinematically related to the inertial velocity as

$$\bar{V} = \bar{V}_I - \bar{V}_{B/I}(t) - \bar{\Omega}_B(t) \times \bar{r}\,, \tag{A.7}$$

and the position vector $\bar{r}$ is given as

$$\bar{r} = \bar{r}_I - \bar{r}_{B/I}(t)\,, \tag{A.8}$$

with $\bar{V}_{B/I}(t), \bar{\Omega}_B(t), \bar{r}_{B/I}(t)$ being the known functions which define a specific maneuver.

Hence, except for the appearance of the apparent velocity, the velocity-vorticity formulation of the unsteady Navier-Stokes equations is form-invariant under a generalized non-inertial coordinate formulation. Therefore, the algorithm developed to solve Eqs. (A.1-A.3) remains valid for the solution of Eqs. (A.4-A.6). The analysis described so far is valid for 3-D flows with six-degree-of-freedom maneuvers.

For the 2-D simulations of interest here, it is computationally more efficient to use the $(\psi, \bar{\omega})$ variables rather than the $(\bar{V}, \bar{\omega})$ variables. Further, due to the unbounded nature of the stream function in the far field at true infinity, it is essential that a deviational stream function be employed as the dependent variable; this is given as

$$\psi_I = y - y_{B/I}(t) + \psi_I^D(\xi^1, \xi^2, t) + \frac{\Gamma(t)}{2\pi} ln\left(\frac{r}{a}\right) \tag{A.9}$$

where $y - y_{B/I}(t)$ is the vertical inertial coordinate passing through the instantaneous location of the pitching axis. The viscous circulation $\Gamma(t)$ is positive in the clockwise direction and 'a' is the radius of the circle to which the airfoil is transformed. The inertial velocity then becomes

$$\bar{V}_I = \hat{i} + \left[\frac{Real(V^* \bar{e}_1)}{g_{11}} + \frac{1}{\sqrt{g}}\frac{\partial \psi_I^D}{\partial \xi^2}\right]\bar{e}_1 + \left[\frac{Real(V^* \bar{e}_2)}{g_{22}} - \frac{1}{\sqrt{g}}\frac{\partial \psi_I^D}{\partial \xi^1}\right]\bar{e}_2\,. \tag{A.10}$$

Here, V^* is the complex velocity defined as $i\frac{\Gamma(t)}{2\pi r}$ due to the generation of circulation, and $\hat{i}$ is the unit base vector of the inertial Cartesian reference frame shown in Fig. A.1. Further, $\bar{e}_1$ and $\bar{e}_2$ are the covariant base vectors of the generalized-coordinate (ξ^1, ξ^2) non-inertial body-fixed reference frame. The determinant of the metric tensor g appearing in Eq. (A.10) is given as

$$g = (g_{11}g_{22} - g_{12}g_{21})$$

where

$$g_{ij} = \sum_{k=1}^{2}\left(\frac{\partial x^k}{\partial \xi^i}\right)\left(\frac{\partial x^k}{\partial \xi^j}\right)\,. \tag{A.11}$$

The independent variables (x^1, x^2) represent the body-fixed Cartesian coordinates whose unit base vectors are $\hat{e}_1$ and $\hat{e}_2$ as shown in Fig. A.1.

In light of Eqs.(A.7) and (A.10), the contravariant components of the apparent velocity are

$$\begin{aligned}\sqrt{g}V^1 &= \frac{1}{g_{11}/\sqrt{g}}[\{\cos\theta_B(t) - V^1_{B/I}(t) + x^2\Omega_B(t)\}\hat{e}_1 \cdot \bar{e}_1 + \\ &\quad \{\sin\theta_B(t) - V^2_{B/I}(t) - x^1\Omega_B(t)\}\hat{e}_2 \cdot \bar{e}_1 + Real(V^*\bar{e}_1)] + \frac{\partial\psi_I^D}{\partial\xi^2} \quad \text{(A.12)}\end{aligned}$$

and

$$\begin{aligned}\sqrt{g}V^2 &= \frac{1}{g_{22}/\sqrt{g}}[\{\cos\theta_B(t) - V^1_{B/I}(t) + x^2\Omega_B(t)\}\hat{e}_1 \cdot \bar{e}_2 + \\ &\quad \{\sin\theta_B(t) - V^2_{B/I}(t) - x^1\Omega_B(t)\}\hat{e}_2 \cdot \bar{e}_2 + Real(V^*\bar{e}_2)] - \frac{\partial\psi_I^D}{\partial\xi^1}, \quad \text{(A.13)}\end{aligned}$$

where [-$\theta_B(t)$]= $\alpha_f(t)$ is the instantaneous pitch angle of the airfoil and $\bar{V}_{B/I}(t) = \bar{V}^1_{B/I}(t)\hat{e}_1 + \bar{V}^2_{B/I}(t)\hat{e}_2$.

Hence, the unsteady Navier-Stokes equations in generalized orthogonal non-inertial body-fixed coordinates take the following form.

Stream Function Equation:

$$\frac{\partial}{\partial\xi^1}\left(\frac{g_{22}}{\sqrt{g}}\frac{\partial\psi_I^D}{\partial\xi^1}\right) + \frac{\partial}{\partial\xi^2}\left(\frac{g_{11}}{\sqrt{g}}\frac{\partial\psi_I^D}{\partial\xi^2}\right) = -\sqrt{g}\omega_I . \quad \text{(A.14)}$$

Vorticity Transport Equation:

$$\begin{aligned}&\sqrt{g}\frac{\partial\omega_I}{\partial t} + \frac{\partial}{\partial\xi^1}\left(\omega_I[\sqrt{g}V^1]\right) + \frac{\partial}{\partial\xi^2}\left(\omega_I[\sqrt{g}V^2]\right) = \\ &\qquad \frac{1}{Re}\left\{\frac{\partial}{\partial\xi^1}\left(\frac{g_{22}}{\sqrt{g}}\frac{\partial\omega_I}{\partial\xi^1}\right) + \frac{\partial}{\partial\xi^2}\left(\frac{g_{11}}{\sqrt{g}}\frac{\partial\omega_I}{\partial\xi^2}\right)\right\} . \quad \text{(A.15)}\end{aligned}$$

In Eqs. (A.14) and (A.15), the elliptic problem for the deviational stream function is coupled with the temporally parabolic vorticity-transport equation. The mathematical formulation can be completed by providing the boundary and intitial conditions. However, before discussing these, the control strategy developed for this study will be examined. The boundary and initial conditions can then be presented in their final form.

Active Control Using Suction and Injection

From a theoretical consideration, Osswald (1992) has pointed out that the vorticity created at the surface drives some of the unsteady flow phenomena. Thus, flow phenomena such as incipient separation and subsequent development of vortical structure near the surface perhaps can be controlled by managing the creation of surface vorticity, which is governed by the vorticity boundary condition at the surface and, hence, is external to the governing equation. Thus, modulated suction/injection(MSI) control is developed. The active control model developed is based on the principal objective of delaying the unsteady separation to suppress the formation of the dynamic-stall vortex. A secondary goal is to increase the lift and reduce drag. In additition to these objectives, the constraints used in developing the active control model are that

i. the maximum non-dimensionalized main flow rate be atmost 1%,
ii. the net mass addition be zero and, finally,
iii. the control model for MSI be as simple as possible.

Constraint (ii) is not critical; however, if employed, it allows the downstream boundary condition for the basic flow without MSI to remain valid for the flow even with the implementation of active control.

The active control model depends on a large number of variables, some of which are location, magnitude, suction/injection rate, duration, etc. A careful numerical optimization led to a trapezoidal profile for the MSI velocity, with the key parameters being depicted in Fig. A.22. In the present study, the suction velocity is taken to be between 3.5% and 4.5% of the free-stream velocity, and is applied on the upper surface of the airfoil over approximately 9% of the chord starting from the leading edge (LE). The physical injection velocity is slightly smaller in magnitude as compared to the physical suction velocity. It should also be pointed out that the segment of the airfoil surface in the computational plane over which suction is applied is the same as that over which injection is applied. Then, to satisfy the constraint of zero net mass addition, injection is applied over 14% of the chord on the lower surface near the trailing edge (TE) of the airfoil. In fact, the constraint can be expressed as follows. In the physical plane, for suction applied over the upper surface near the LE segment (a-b), and injection over the lower surface near the TE segment (c-d), zero net mass addition requires

$$\int_a^b \frac{1}{\sqrt{g_{22}}}(\bar{V}\cdot\bar{e}_2)dl\,|_{suc.} + \int_c^d \frac{1}{\sqrt{g_{22}}}(\bar{V}\cdot\bar{e}_2)dl\,|_{inj.} = 0\,, \qquad \text{(A.16)}$$

where the apparent velocity $\bar{V}$ on the surface can be written as

$$\bar{V} = T(\xi^1,\xi^2_w,t)\hat{t} + N(\xi^1,\xi^2_w,t)\hat{n} = T(\xi^1,\xi^2_w,t)\frac{\bar{e}_1}{\sqrt{g_{11}}} + N(\xi^1,\xi^2_w,t)\frac{\bar{e}_2}{\sqrt{g_{22}}}\,. \qquad \text{(A.17)}$$

In the non-inertial reference frame of the generalized-coordinates (ξ^1, ξ^2), Eq. (A.16) is given as

$$\int_{\xi^1{}_{np}} \sqrt{g_{11}} N(\xi^1, \xi^2_w, t) d\xi^1 = 0 \,. \tag{A.18}$$

where ξ^1_{np} represents the non-porous segments of the airfoil surface in the computational plane.

Boundary Conditions

Using Eqs. (A.12) and (A.13), the apparent velocity $\bar{V}$ can be expressed as

$$\begin{aligned} \bar{V} = &\left[\cos\theta_B(t) - V^1_{B/I}(t) - x^2\Omega_B(t)\right]\hat{e}_1 + \left[\sin\theta_B(t) - V^2_{B/I}(t) + x^1\Omega_B(t)\right]\hat{e}_2 \\ &+ \left[\frac{Real(V^*\bar{e}_1)}{g_{11}} + \frac{1}{\sqrt{g}}\frac{\partial\psi^D_I}{\partial\xi^2}\right]\bar{e}_1 + \left[\frac{Real(V^*\bar{e}_2)}{g_{22}} - \frac{1}{\sqrt{g}}\frac{\partial\psi^D_I}{\partial\xi^1}\right]\bar{e}_2 . \end{aligned} \tag{A.19}$$

From Eqs.(A.17) and (A.19),

$$\begin{aligned} \frac{g_{22}}{\sqrt{g}}\frac{\partial\psi^D_I}{\partial\xi^1}\,|_{body} = &[\{\cos\theta_B(t) - V^1_{B/I}(t) + x^2\Omega_B(t)\}\hat{e}_1 + \\ &\{\sin\theta_B(t) - V^2_{B/I}(t) - x^1\Omega_B(t)\}\hat{e}_2]\cdot\bar{e}_2 \\ &+ Real(V^*\bar{e}_2) - \sqrt{g_{22}}N(\xi^1, \xi^2_w, t) \,. \end{aligned} \tag{A.20}$$

Eq. (A.20) leads to the boundary condition for the stream function at the surface as

$$\begin{aligned} \psi^D_I(\xi^1, \xi^2_w, t) = &\{x^2[V^1_{B/I}(t) - \cos\theta_B(t)] - x^1[V^2_{B/I}(t) - \sin\theta_B(t)] \\ &- \frac{\Omega_B(t)}{2}[(x^1)^2 + (x^2)^2]\} - \frac{\Gamma(t)}{2\pi} ln\left(\frac{r}{a}\right) \\ &- \int_{\xi^1_{np}} \sqrt{g_{11}} N(\xi^1, \xi^2_w, t) d\xi^1 \,, \end{aligned} \tag{A.21}$$

where ξ^1_{np} represents the non-porous segments of the body surface. Now, the surface vorticity can be evaluated from the following equation:

$$\omega_I\,|_{body} = -\frac{1}{\sqrt{g}}\left[\frac{\partial}{\partial\xi^1}\left(\frac{g_{22}}{\sqrt{g}}\frac{\partial\psi^D_I}{\partial\xi^1}\right) + \frac{\partial}{\partial\xi^2}\left(\frac{g_{11}}{\sqrt{g}}\frac{\partial\psi^D_I}{\partial\xi^2}\right)\right]_{body} , \tag{A.22}$$

subject to the constraint of zero slip, which leads to

$$\begin{aligned} \frac{g_{11}}{\sqrt{g}}\frac{\partial\psi^D_I}{\partial\xi^2}\,|_{body} = &-[\{\cos\theta_B(t) - V^1_{B/I}(t) + x^2\Omega_B(t)\}\hat{e}_1 + \\ &\{\sin\theta_B(t) - V^2_{B/I}(t) - x^1\Omega_B(t)\}\hat{e}_2]\cdot\bar{e}_1 \\ &- Real(V^*\bar{e}_1) + \sqrt{g_{11}}T(\xi^1, \xi^2_w, t) \,. \end{aligned} \tag{A.23}$$

Eq. (A.20) is also used in the evaluation of Eq. (A.22). The corresponding condition in the far field can be written as

$$\psi^D_I = 0, \tag{A.24}$$

$$\omega_I = 0. \tag{A.25}$$

The examination of this boundary condition reveals that the viscous circulation $\Gamma(t)$ is still not determined; its determination is described in the next sub-section.

Viscous Circulation and Necessary Condition for Its Determination

The inviscid circulation $\Gamma_{in}(t)$ is given as

$$\Gamma_{in}(t) = 4\pi a \sin \alpha_f(t) \tag{A.26}$$

where 'a' is the radius of circle to which the airfoil is transformed(see Fig. A.3(d, e)) and α_f is the flow angle at the given instant of time. The circulation $\Gamma(t)$ for the overall viscous flow is related to the inertial velocity $\bar{V}_I$ as

$$\Gamma(t) = \oint_{\infty} \bar{V}_I \cdot d\bar{l} = -\oint_{C_\infty} \bar{V}_I \cdot d\bar{l}, \tag{A.27}$$

taken around a circle C_∞ with its radius equal to infinity. The use of the Stokes' theorem leads to

$$\Gamma(t) = -\int_{S_o} (\nabla \times \bar{V}_I) \cdot \bar{n} ds = -\int_{S_o} \bar{\omega}_I \cdot \bar{n} ds, \tag{A.28}$$

where S_o is the corresponding area of the entire flow domain whose boundary curve is C_∞. Even with this condition, the stream-function and vorticity equations, Eqs. (A.14-A.15), still constitute a singular system of equations due to the linear dependence amongst these equations. This led to imposing the condition that the pressure in the multiply-connected flow domain be single valued and continuous along the body surface, i.e.,

$$\oint_{body} (\nabla p) \cdot d\bar{l} = 0. \tag{A.29}$$

For flow past a square cylinder in a channel, again a multiply-connected domain, Matlda, Kuwahara and Takami (1975) had used Eq. (A.29) to close the equation set for their internal flow problem. This has provided the impetus to use this equation in the present analysis also. Indeed, Eq. (A.29) is used in the present analysis and serves to close the equation set. This condition is an alternative statement of the Kutta condition for viscous unsteady flow, namely, that the pressure at the TE has to be continuous and single valued. Osswald, K. Ghia and U. Ghia (1992) have pointed out that the only influence that pressure has on an incompressible flow is that it controls the creation and distribution of surface vorticity. Further, this condition helps to close the problem thereby implying that advanced wall vorticity can now be accurately determined. Next, the initial conditions used in the present analysis are discussed.

Initial Conditions

To determine the flow field past a maneuvering body, initially the simulation of the flow past a stationary airfoil at fixed angle of attack is carried out. For this latter stationary configuration, the motion is started impulsively from rest at t=0 and the corresponding inviscid solution is used as the initial condition. The viscous flow past a stationary body at a given angle of attack is determined. Next, up to an asymptotic time, $\tilde{t} = T$, the maneuvering motion is inititated at $\tilde{t} = T$ and the viscous circulation at the start is taken as

$$\Gamma(t)\,|_{t=0} = \Gamma_o(T) \tag{A.30}$$

where $\lim_{\tilde{t} \to T} \Gamma(\tilde{t}) = \Gamma_o(T)$ is the asymptotic value of the circulation computed by accounting for the angular acceleration $\vec{\alpha}_{B/I}(t)$ due to manuevering motion in the value of the circulation around a stationary airfoil.

Pressure and Force Coefficients

The analysis to be discussed here follows the development provided by Yang (1992). In the present $(\omega_I, \psi_I^D, \Gamma(t))$ formulation, pressure does not appear and, as such, to determine pressure, it is necessary to revert back to the linear-momentum equation given as

$$\frac{\partial \vec{V}_I}{\partial t} + \left(\nabla \times \vec{V}_I\right) \times \vec{V}_I + \frac{1}{Re}\left(\nabla \times \nabla \times \vec{V}_I\right) = -\nabla\left(p + \frac{|\vec{V}_I|^2}{2}\right). \tag{A.31}$$

The pressure field in the incompressible flow can be evaluated accurately using the pressure Poisson equation obtained by taking the divergence of the linear-momentum equation, Eq. (A.31). If, on the other hand, only surface pressure is desired, it can be determined more readily by carefully evaluating Eq. (A.31), along the surface; this leads to

$$\begin{aligned}\frac{\partial(p+q)}{\partial \xi^1}\Big|_{body} = & \underbrace{-\sqrt{g_{11}}\frac{\partial T(\xi^1,\xi^2_w,t)}{\partial t}}_{\substack{\text{Tangential Acceleration}\\ \text{due to circulation control}\\ \text{along the body surface}}} -(\vec{\alpha}_{B/I}(t)\times\vec{r})\ \vec{e}_1 \\ & + \underbrace{\sqrt{g_{11}}N(\xi^1,\xi^2_w,t)\omega_I}_{\substack{\text{Pressure gradient due to}\\ \text{mass transfer along the}\\ \text{body surface as a result}\\ \text{of MSI}}} - \frac{1}{Re}\frac{g_{11}}{\sqrt{g}}\frac{\partial \omega_I}{\partial \xi^2},\end{aligned} \tag{A.32}$$

where

$$q = \frac{1}{2}\underbrace{\left\{T^2(\xi^1,\xi^2_w,t) + N^2(\xi^1,\xi^2_w,t)\right\}}_{\text{Addition of kinetic energy due to MSI}} + a^1_{B/I}(t)x^1 + a^2_{B/I}(t)x^2 - \frac{1}{2}\left\{(x^1)^2 + (x^2)^2\right\}\Omega^2_B(t). \tag{A.33}$$

For evaluation of the terms involving apparent velocity on the surface, not all terms are zero and, for some additional details, see Yang (1992). Careful examination of Eq. (A.32) reveals that the temporal increase of the tangential control velocity can accelerate the flow, since $\frac{\partial p}{\partial \xi^1} < 0$ and, for suction with $N(\xi^1,\xi^2_w,t) < 0$, as implemented in the unsteady separation region where $\omega_I > 0$, $\sqrt{g_{11}}N(\xi^1,\xi^2_w,t)\omega_I$ will also produce favorable pressure gradient and will lead to reduction in the boundary layer thickness. Thus, integrating Eq. (A.32) leads to

$$p\,\Big|^{f_{TE}}_{i_{TE}} = -q\,\Big|^{f_{TE}}_{i_{TE}} + \int_{\xi^1_0}^{\xi^1_1}\left\{\sqrt{g_{11}}N(\xi^1,\xi^2_w,t)\omega_I - \sqrt{g_{11}}\frac{\partial T(\xi^1,\xi^2_w,t)}{\partial t}\right\}d\xi^1$$

$$- \int_{\xi^1_0}^{\xi^1_1}\left\{(\bar{\alpha}_{B/I}(t)\times\bar{r})\cdot\bar{e}_1 + \frac{1}{Re}\frac{g_{11}}{\sqrt{g}}\frac{\partial\omega_I}{\partial\xi^2}\right\}d\xi^1\,. \tag{A.34}$$

This then permits the determination of the surface pressure.

The force and moment coefficients as well as the surface force due to viscosity are now calculated using the surface pressure from Eq. (A.34), and the definition of the coefficient of pressure as

$$C_p = \frac{p^*}{\frac{1}{2}\rho U^2_\infty} = 2p\,, \tag{A.35}$$

where p^* is the dimensional pressure.
Further, the force coefficient $\bar{C}_{F_p}$ is defined as

$$\bar{C}_{F_p} \triangleq \frac{\bar{F}_p}{\frac{1}{2}\rho U^2_\infty cb}\,, \tag{A.36}$$

where the spanwise length b is taken as unity.
Substituting Eq. (A.34) into Eq. (A.35), Eq. (A.36) is then written as

$$\bar{C}_{F_p} = -\oint_{body}\left\{\frac{\sqrt{g_{11}}}{\sqrt{g_{22}}}C_p\bar{e}_2\right\}d\xi^1\,. \tag{A.37}$$

Similarly, the net dimensional force $\bar{F}_v$ due to viscosity is given as

$$\bar{F}_v = \oint_{body} 2\mu^*\left\{\frac{1}{2}\left[(\nabla^*\bar{V}^*_I) + \bar{V}^*_I\nabla^*)\right] - \frac{1}{3}(\nabla^*\bar{V}^*_I)\bar{I}\right\}\cdot\hat{n}ds^*\,, \tag{A.38}$$

where μ^* is the dynamic viscosity and $\bar{\bar{I}}$ is the identity tensor.

The coefficient of the viscous shear force is defined as

$$\bar{C}_{F_v} \triangleq \frac{\bar{F}_v}{\frac{1}{2}\rho U_\infty^2 cd}. \tag{A.39}$$

Use of the expression for apparent velocity, Eq. (A.7), permits Eq. (A.39) to be expressed as

$$\bar{C}_{F_v} = \frac{2}{Re}\oint_{body}\left[(\nabla\bar{V}) + (\bar{V}\nabla)\right]\cdot\hat{n}ds. \tag{A.40}$$

For flows with MSI, an expression for Eq. (A.40) can be obtained in non-inertial body-fixed generalized coordinates (ξ^1, ξ^2) as

$$\bar{C}_{F_v} = \frac{2}{Re}\oint_{body}\left\{\bar{e}^1\frac{\partial\bar{V}}{\partial\xi^1} + \bar{e}^2\frac{\partial\bar{V}}{\partial\xi^2} + \frac{\partial\bar{V}}{\partial\xi^2}\bar{e}^2\right\}\cdot\bar{e}_2\frac{\sqrt{g_{11}}}{\sqrt{g_{22}}}d\xi^1, \tag{A.41}$$

where $\bar{e}^1$ and $\bar{e}^2$ are the contravariant base vectors of the generalized coordinates (ξ^1, ξ^2). In addition, by defining

$$\frac{\partial\bar{V}}{\partial\xi^1} \equiv A^1\bar{e}_1 + A^2\bar{e}_2 \qquad and \qquad \frac{\partial\bar{V}}{\partial\xi^2} \equiv B^1\bar{e}_1 + B^2\bar{e}_2, \tag{A.42}$$

Eq. (A.41) can be rewritten as

$$\bar{C}_{F_v} = \frac{2}{Re}\oint_{body}\left\{\left(\frac{\sqrt{g_{22}}}{\sqrt{g_{11}}}A^2 + \frac{\sqrt{g_{11}}}{\sqrt{g_{22}}}B^1\right)\bar{e}_1 + 2\frac{\sqrt{g_{11}}}{\sqrt{g_{22}}}B^2\bar{e}_2\right\}d\xi^1. \tag{A.43}$$

Along the non-porus body surface, Eq. (A.41) is simplified to give

$$\bar{C}_{F_v} = \frac{2}{Re}\oint_{body}\left\{\frac{\sqrt{g_{11}}}{\sqrt{g_{22}}}\frac{\partial}{\partial\xi^2}(V^1)\bar{e}_1\right\}d\xi^1. \tag{A.44}$$

A similar analysis leads to the moment coefficients $\bar{C}_{M_p}$ and $\bar{C}_{M_v}$ as

$$\bar{C}_{M_p} = \oint_{body}\left[\frac{\sqrt{g_{11}}}{\sqrt{g_{22}}}C_p(\xi^1)\left\{x^1(\hat{e}_1\times\bar{e}_2) + x^2(\hat{e}_2\times\bar{e}_2)\right\}\right]d\xi^1, \tag{A.45}$$

and

$$\begin{aligned}\bar{C}_{M_v} = -\frac{2}{Re}\oint_{body}&\left[\left\{\frac{\sqrt{g_{22}}}{\sqrt{g_{11}}}A^2 + \frac{\sqrt{g_{11}}}{\sqrt{g_{22}}}B^1\right\}\left\{x^1(\hat{e}_1\times\bar{e}_1) + x^2(\hat{e}_2\times\bar{e}_1)\right\}\right]d\xi^1\\ &-\frac{4}{Re}\oint_{body}\left[\frac{\sqrt{g_{11}}}{\sqrt{g_{22}}}B^2\ \ x^1(\hat{e}_1\times\bar{e}_2) + x^2(\hat{e}_2\times\bar{e}_2)\}\right]d\xi^1.\end{aligned} \tag{A.46}$$

For non-porus body surface,

$$\bar{C}_{M_v} = -\frac{2}{Re}\oint_{body}\left[\frac{\sqrt{g_{11}}}{\sqrt{g_{22}}}\frac{\partial V^1}{\partial\xi^2}\left\{x^1(\hat{e}_1\times\bar{e}_1) + x^2(\hat{e}_2\times\bar{e}_1)\right\}\right]d\xi^1. \tag{A.47}$$

To calculate the lift and drag coefficients from $\bar{C}_{F_p}$ and $\bar{C}_{F_v}$, it is convenient to define the force vector $\bar{F}$ as a complex variable such that

$$\bar{F} = Real(\bar{F})\hat{e}_1 + Imag(\bar{F})\hat{e}_2\,, \tag{A.48}$$

With this definition in Eq. (A.44), as shown in Fig. A.2, the lift and drag coefficients become

$$\begin{aligned} C_{L_p} &= Imag(\bar{C}_{F_p}) \times \cos\theta_B(t) - Real(\bar{C}_{F_p}) \times \sin\theta_B(t), \\ C_{D_p} &= Real(\bar{C}_{F_p}) \times \cos\theta_B(t) + Imag(\bar{C}_{F_p}) \times \sin\theta_B(t), \\ C_{L_v} &= Imag(\bar{C}_{F_v}) \times \cos\theta_B(t) - Real(\bar{C}_{F_v}) \times \sin\theta_B(t), \\ C_{D_v} &= Real(\bar{C}_{F_v}) \times \cos\theta_B(t) + Imag(\bar{C}_{F_v}) \times \sin\theta_B(t). \end{aligned} \tag{A.49}$$

Further,

$$C_L = C_{L_p} + C_{L_v}\,, \tag{A.50}$$

$$C_D = C_{D_p} + C_{D_v}\,, \tag{A.51}$$

$$C_M = C_{M_p} + C_{M_v}\,. \tag{A.52}$$

2.A.3 Analytical Grid Generation Technique

The mathematical problem formulated in Section A.2 is governed by a set of partial differential equations which can be solved efficiently using an advanced numerical technique. The overall solution technique will require a carefully generated grid that satisfies numerous criteria as far as quality of the grid is concerned. The grid should also provide the resolution of dominant length scales in the various critical regions that evolve in the flow field. The use of appropriate grid topology with a given mathematical formulation is also critical, since certain Navier-Stokes operators may turn out to be singular on a specific grid topology. The generalized Schwarz-Christoffel grid generation technique originally described by Davis (1979) and further developed by Osswald, K. Ghia and U. Ghia (1989) for flow past an arbitrary airfoil is used in this study.

Conformal Transformation

The generalized mapping technique used here is conformal and provides analytic metric information, guarantees orthogonality, and has the capability of handling arbitrary bodies with sharp corners that occur for example at TE, etc. As shown in Fig. A.3(a), a conformal mapping from the physical z-plane permits the airfoil to be transformed into a line segment in the upper half ζ-plane, as shown in Fig. A.3(b). A second conformal transformation permits this line segment in the upper half ζ-plane to be transformed to the complex potential plane P, as shown in Fig. A.3(c). This is subsequently transformed using the Joukowski transformation to a circle in the Z-plane, as shown in Fig. A.3(d). For lifting cases at non-zero incidence α_f, the Z-plane can be rotated by the effective angle of attack, $\alpha_e = \alpha_f + \beta$ to the circle-R plane, as shown in Fig. A.3(e), where 'a' is the flow incidence angle and -β is the angle of zero lift. The complex potential P for a uniform stream at incidence α_f past an arbitrary airfoil is obtained from the knowledge of the complex potential for flow past a circular cylinder. The complex potential P-plane is depicted in Fig. A.3(f) and, if used as a final plane, it leads to a mesh with H-grid topology in the physical plane. This H-type grid does not provide sufficient resolution in the rounded-LE region. Therefore, yet one more parabolic conformal transformation is used to transform the airfoil to the complex η-plane, as shown in Fig. A.3(g). This now leads to a C-grid topology in the physical plane. Even though the C-grid will provide some clustering the LE region, the far-field boundary condition to be placed at infinity will lead to numerical difficulties if η-plane is used. Hence, the final transformation contracts this η-plane to the computational plane and is described in the next sub-section.

Clustering Transformations

One-dimensional clustering transformations are used to transform the upper-half stagnation point η-plane to a unit square in the computational ξ-plane. Osswald, K. Ghia and U. Ghia (1989) as well as Rohling (1991) have provided the details of the general cubic-spline functions used. In the streamwise direction, independent cubic-spline functions are used to achieve streamwise grid clustering along the suction and pressure surfaces and in the mid-wake and near-wake regions, both above and below the streamline which emanates from the trailing edge. The far-wake regions above and below the TE streamline are contracted using 1-D inverse tangent transformations. Similarly, 1-D cubic-spline transformations are also used in the normal directions in two zones, namely, (i) boundary layer and (ii) massively separated region which also includes the LE shear layer. Finally, a 1-D inverse tangent transformation is again required to map the far-field infinity boundary to a unit distance in the computational ξ-plane. The various regions discussed here are depicted in Fig. A.4. A typical grid distribution for a NACA 0015 airfoil with (444 × 101) mesh points is shown in Fig. A.5. An attempt has been made to resolve as many of the dominant scales as possible; these include the boundary layer scale of $O(Re^{-1/2})$ for attached flow, the streamwise and normal scales of $O(Re^{-3/8})$ and $O(Re^{-5/8})$, respectively, near the separation point, the separated free shear layer with the scale of the order of its thickness, the massively separated zone of $O(1)$ and the scale of $O(Re^{-5/11})$ for the boundary layer eruption in the separated region. This is important in order to ensure that the simulation results truly preserve the physics of the problem. The way in which this is partially achieved is by generating a grid with zonal attributes with continuous metrics across all of the zones both in streamwise and normal directions. Not only is the clustered conformal grid generated here by an analytical-numerical procedure, but the evaluation of the metric tensor and base vectors is also carried out analytically once the transformations have been defined.

2.A.4 Numerical Method

The basic numerical technique for maneuvering motion was developed by Osswald, K. Ghia and U. Ghia (1990). Variations of this approach have been used by the present researchers in some of their earlier papers. It is a fully implicit finite-difference method involving direct matrix inversion methodology. All of the spatial derivatives are approximated using second-order accurate central difference approximations, except for the convective terms. These latter nonlinear terms are approximated using a biased, third-order accurate, upwind differencing-scheme to be able to simulate higher Reynolds number flows. The vorticity transport equation, Eq. (A.15), is solved using a variation of the alternating-direction implicit (ADI) technique of Douglas and Gunn (1964). When this technique is cast in delta form, it is computationally efficient. The elliptic stream function equation, Eq. (A.14), is solved by a direct block Gaussian elimination (BGE) technique. No explicit artificial dissipation is added in the implementation of the overall ADI-BGE method.

The algorithm consists of a forward elimination sweep for the vorticity and stream function equations. This is followed by the determination of advanced wall vorticity, together with the computation of the viscous circulation. This is achieved with the help of Eq. (A.29) which requires continuity of the pressure at the trailing edge. Both the wall vorticity and $\Gamma(t)$ are determined using an iterative technique and by maintaining a strict convergence criterion, such that the relative percentage error is less than 10^{-6}, and the residue in the instantaneous wall vorticity is negligible. Subsequently, the back substitution sweep for the vorticity and stream function equations is carried out to achieve the final solution. It should be noted that, due to the use of the third-order biased upwind differencing, the discretized problem leads to a penta-diagonal matrix which can be solved using a generalized Thomas algorithm.

One final comment corresponds to the determination of the pressure field. The analysis provided so far is adequate if only surface pressure is of interest. On the other hand, if the entire pressure field is desired, the solution of a Neumann Poisson problem for pressure can be carried out as given by K. Ghia, Yang, Osswald and U. Ghia (1992a). The results obtained in the present study are discussed next.

2.A.5 Results and Discussion

The continuous and discrete analysis developed in the earlier sub-sections is used to study the motion past maneuvering NACA airfoils. In this sub-section, first the constant-rate pitch-up motion studied will be outlined, followed by validation and verification studies. Finally, some detailed results will be provided for constant-rate pitch-up motion; these results are computed without and with modulated suction/injection. Simulation results are also obtained in the form of a color video animation and, while discussing the results, the present authors have taken the liberty to use these animations to clarify various research issues and provide further insight into the prevailing flow phenomena.

A total of three flow configurations have been studied;
these are as listed below.

Configuration	Re	$\dot{\alpha}^+/K$	Remarks
I	5,000	1.0	for verification study
II	45,000	0.2	without flow control
III	45,000	0.2	with modulated suction/injection

In addition, results have been obtained for a flow configuration with Re=52,000 and $\dot{\alpha}^+ = 0.072$. These results have been discussed by Yang (1992).

Constant-Rate Pitch-Up Manuever

In all the earlier studies by the authors, the constant-rate pitch-up motion used is the one defined by Visbal and Shang (1989) as:

$\bar{r}_{B/I}(t) = 0,$

$$\theta_B(t) = \Omega_o[t - \frac{t_o}{(4.6)}(1 - e^{-(4.6/t_o)t}] \qquad \text{(A.53)}$$

where $\Omega_o = \dot{\alpha}^+ = \frac{\Omega c}{U_\infty}$ is the non-dimensional pitch rate and $\theta_B(t)$ is the instantaneous pitch angle of the airfoil. In the present study, $t_o = 0.5$, $\Omega_o = 0.2$ and the airfoil is pitched about the axis through the quarter-chord point (QCP).

Verification Study

The earlier studies of the authors in Refs. [A.11, A.12, A.13, A.14 and A.28] have already established that the mathematical model is accurate and that the modification in the far-field boundary condition which necessitates the use of viscous circulation $\Gamma(t)$ has indeed given better results, as shown by Osswald, K. Ghia and U. Ghia (1992). Thus, the main emphasis here is on the verification study, rather than on validation of the mathematical model. In this verification study, the accuracy of the numerical solutions obtained is examined critically, and the influence of the discretized parameters of the problem on the solution is assessed.

Flow Configuration II described above is used for the verification study. The parameters for this basic flow configuration II are Re = 45,000, $\dot{\alpha}^+ = 0.2$. Three different grid sizes, namely (i) coarse grid with (330x75) points, (ii) medium (standard) grid with (444 × 101) points, and (iii) fine grid (544 × 121) points are used. The minimum grid spacings for the standard grid in the streamwise and normal diretions near the leading edge were 0.54×10^{-3} and 0.26×10^{-4}, respectively. To resolve the temporal scale of this unsteady separated flow problem and to achieve time consistency of the solution, a value of $\Delta t = 0.001$ was chosen. The code has been fully vectoized and requires 7.5 micro-seconds per time step, per mesh point, using a single processor of the CRAY Y-MP 8/864 of The Ohio Supercomputer Center.

Effect of Grid Stretching on the Solution

Unique to the present analysis is the fact that the far-field boundary condition is implemented at true infinity. As discussed earlier in the Section A.3.2, 1-D clustering transformations are used to treat the infinite domain numerically. It is the arc tangent transformation that permits the mapping of the boundary at infinity to a finite location in the computational plane. This implies that the grids are stretched exponentially and it is important to examine the variation of the dependent variables in the far field and, specifically, their approach to the imposed far-field boundary conditions, if the solutions are to be accurate. Due to the clustering transformation, cells of semi-infinite extent occur in the physical plane. The effect of large grid stretching on the solution can be seen best in the computational plane, and is discussed now.

Vorticity attenuates exponentially away from the surface where it is created. Fig. A.6(a-b) shows the vorticity contours for flow past a NACA 0015 airfoil undergoing constant-rate pitch-up motion with $\dot{\alpha}^+ = 0.2$, for two different instantaneous positions, $\alpha = 20.54^\circ$ and 36.58°, respectively. The global views for both instants are shown in this figure, as are the enlarged views in the far-field, which clearly show that the vorticity approaches smoothly to the far-field boundary condition of $\tilde{\omega}_I = 0$. The effect of grid stretching on the corresponding stream function is shown in Fig. A.7. A close look at Fig. A.7(a-b) clearly shows that the far-field boundary is reached as the value of the deviational (i.e., the disturbance) stream function approaches zero, i.e., as $\psi_I^D = 0$.

A round-off error study was also performed, and the procedure is as follows. In the Dirichlet Poisson equation for ψ_I^D, Eq. (A.14), ψ_I^D is assumed to be known analytically as any one of the two functions prescribed in Fig. A.9. With this function, the source term involving ω_I is computed numerically using a finite-difference stencil, with extended precision. The computed values of ω_I are used to solve the stream function equation, Eq. (A.14), and the numerically computed values of ψ_I^D are compared with the corresponding known analytical values. The difference in the two solutions represents the round-off error on the present (444 × 101) grid. Fig. A.9 clearly shows that the maximum error never exceeds 10^{-7} for a solution field which lies between 0 and 1. The error also does not exceed the maximum truncation error of $O(10^{-4})$. In addition, the metric coefficients used in the calculations are shown in Fig. A.8; these are well behaved as expected.

Grid-Refinement Study

The grid distribution for all of the three grids mentioned earlier, in the proximity of the NACA 0015 airfoil are depicted in Fig. A.10. For the airfoil at zero angle of attack in flow configuration II, the instantaneous vorticity contours near the TE and, subsequently, in the near wake, are presented here. They show that the flow structure consisting of nearly symmetric vortices at the TE prevails for all of the grids at t = 3.5. As t increases to 4.5, the results of the finer grid show that the vortex symmetry is broken, that is the Hopf bifurcation has just occurred forming the asymmetric needle-type vortical structures of opposite sign in the flow field. At still larger time t = 5.5, the flow field results of medium grid show the vortex shedding process which is not only lagging the fine grid results but it also is out of phase with the latter results. The coarser results still continue to show further growth of the symmetric vortical structures near the TE. For truly unsteady flow, it is difficult to carry out this grid refinement study, but in light of present results the degree to which the differences are observed is clarified.

Once the asymptotic state is achieved for the flow field with the airfoil at zero angle of attack, the constant-rate pitch-up motion with $\dot{\alpha}^+ = 0.2$ was initiated. The results in terms of the instantaneous vorticity contours for $15.96^\circ \leq \alpha \leq 35.44^\circ$ are delineated in Fig. A.11. The coarse-grid results are quantitatively different. It should also be stated that, as compared to the results in Fig. A.10, the results for the medium grid do show departure from the fine-grid results, although qualitatively the two structures are very similar. Thus, the results in Fig. A.11 suggest to further refine the grid and see if the changes are smaller than the previous refinement in which grid size was changed from (444 × 101) to (544 × 121). Unfortunately, the results with the (544 × 121) are computationally very costly, with the total CPU time for the fine grid case nearly 5 times higher than for the medium grid case using a single processor on the CRAY Y-MP 8/864 at the Ohio Supercomputer Center. Next, the C_p-distribution at the surface as well as wall vorticity are plotted in Figs. A.12(a-b) for $\alpha = 14.81^\circ$ and 29.71°, respectively. For $\alpha = 14.81^\circ$, where the flow is mostly attached, the surface C_p-distribution for all three grids is in conformity and it even agrees well with the experimental data of Walker, Helin and Strickland (1985). The corresponding wall vorticity has a similar behavior, as shown in Fig. A.12(a); however, there are no experimental data available for wall vorticity. On the other hand, at $\alpha = 29.71^\circ$, with massively separated flow regions, the surface C_p-distributions show significant changes, although qualitatively they do conform to the experimental results given by Walker, Helin and Strickland (1985). In Fig. A.12(b), the wall vorticity on the suction surface does show significant departures, again questioning the grid independence of the results between the medium and fine grid at this level of the grid size. The only satisfactory comparison is that for C_L, as shown in this figure. It depicts that the coarse-grid results compare well with the experimental data of Walker, Helin and Strickland (1985). However, the medium- and fine-grid results predict higher C_L-distribution in the massively separated flow regime. A careful examination of the experimental set-up reveals that Walker et al. (1985) had only 36 surface static pressure taps, as compared to about 207 grid points in the present simulation with (444 × 101) grid points. Thus, better resolution in the computational simulation permits determination of each of the individual vortices that evolve and carries with it somewhat higher values for C_L-distribution as compared to the corresponding experimental values. Hence, for the finest grid used present, still larger values of C_L are seen in this figure. *

Comparison with Available Navier-Stokes Results

Simulation results are also obtained for a sinusoidally pitching NACA 0012 airfoil with Re = 5,000, $\alpha = 10^\circ(1 - \cos kt)$, and reduced frequency based on chord length, k = 1.0. Some experimental data is available for this configuration from Werlé (1976). Also, Mehta (1977) has provided carefully simulated Navier- Stokes results using the NS equations in terms of $(\bar{\omega}, \bar{\psi})$. He has used an O-grid topology and provided detailed results. As seen in Fig. A.13, the streaklines for the present results compare favorably with the experimental data of Werlé (1976) and show a flow structure representative of unsteady flows. The flow is separated over the entire suction surface. Also shown in this figure are the contours of instantaneous vorticity and the velocity vectors. The better resolution of the present results is clear and these results conform well with those of Mehta (1977). For this sinusoidally pitching airfoil, the instantaneous stream-function contours are compared in Fig. A.14. The results first show one instant for $\alpha = 18.59^\circ$ in the upward stroke, which goes up to $\alpha = 20^\circ$, and then four values of α for the return stroke. For the stream function, which is not very sensitive, the agreement is good. For the same values of α, comparison is also provided for the instantaneous vorticity contours in Fig. A.15. The qualitative agreement between the two sets of results is very good, although the better resolution of the present results due to the use of a finer grid, made possible by a better and larger computer is very evident. The complete evolution of the dynamic stall event is vivid, and some of the interactions that take place can be inferred from this figure. Finally, the C_L-distribution, as well as the surface pressure coefficients for two values of α, namely, $\alpha = 18.57°$ during pitch-up and $\alpha = 11.11°$ during pitch down, are shown in Fig. A.16. Also shown in this figure are the results of Sankar and Tassa (1980). In general, C_L compares qualitatively with the existing results, but there are significant deviations. For the time being, this completes the verification study; additional verification with experimental data is provided in the next sub-section.

Influence of Initial State on the Flow Field

For flow configuration II, results are initially obtained to determine the asymptotic state at fixed angle of attack. Since this asymptotic state is not unique, the effect of the initial state of flow will prevail in the final solution. To determine this effect, three different asymptotic states are selected, and correspond to states (b), (c) and (d) on the C_L-history curve in Fig. A.17 corresponding to $\alpha = 0°$. With these states as the starting solutions, three different calculations are made for constant-rate pitch-up motion and the results are compared in Fig. A.17. The lift coefficient distribution, as well as the viscous circulation, for all three cases do conform with each other and do not show strong influence of the initial state. The instantaneous vorticity contours are also shown in this figure and, although there is a phase difference in the development of the wake, the overall influence is minimal.

Flow Structure for Configuration II: Re = 45,000, No Suction

For this configuration, Walker, Helin and Strickland (1985) have provided flow visualization photographs for six selected values for angle of attack. These photographs very vividly show initially the region of separated flow near LE and TE and, subsequently, the formation of a highly energetic dynamic stall vortex. Streaklines are plotted in Fig. A.18 at $\alpha = 24°, 27°, 30°, 40°$ and $47°$ and they compare well with the flow visualization data. Further, the C_L-history, as well as the surface distribution of C_p are compared with the experimental data in Fig. A.19(a,b). As seen in Fig. A.19(a), the C_L-distribution agrees qualitatively, but shows higher values of C_L. It was also pointed out that better agreement with experimental data is obtained for the coarse-grid simulation using (330 × 75) points. Also shown here is C_L-distribution predicted by Visbal and Shang (1989); this too agrees better with the experimental data. In the opinion of the present authors, this is again due to their relatively somewhat coarser grid of (203 × 101) points, coupled with their treatment of the far-field boundary condition. Next, the coefficient of surface pressure distribution is compared for two values, $\alpha = 14.81°$ and $29.71°$, in Fig. A.19(b). As seen here, the comparison with the experimental data of Walker, Helin and Strickland (1985) is good for $\alpha = 14.81°$, whereas, for $\alpha = 29.71°$, the two-distributions depart significantly at the suction surface. It is again the opinion of the authors that this is due to three-dimensionality in the flow field. The results presented so far, provide additional verification of the present analysis.

Next, the detailed flow structure is depicted in Figs. A.20-A.21 using the instantaneous vorticity contours with α varying from 11.37° to 29.71°. Here, global flow structure information is made available, along with an enlarged view showing the LE flow structure. As the airfoil is pitched-up, flow reversal takes place near the LE as shown in this figure. Subsequently, the flow reversal evolves into secondary, tertiary and quaternary vortices. The eruption of this secondary vortex structure initiates the formation of the energetic dynamic-stall vortex. K. Ghia, Yang, Osswald and U. Ghia (1992) have provided further details of this behavior.

Flow Structure for Configuration III: Re = 45,000 with Modulated Suction/Injection

In an attempt to control the formation of the dynamic stall vortex, two specific MSI controls were used. These are Case 1 with $v_s/U_\infty = 0.045$ and Case 2 with $v_s/U_\infty = 0.035$, as presented in Fig. A.22. The ramp functions used for these two configurations to bring the magnitude of suction velocity to its final magnitude are shown in this figure; these magnitudes are held constant thereafter. Also shown in this figure is the viscous circulation for configuration III as well as for both cases of configurations II. The start of the MSI is also indicated. In addition, the velocity vectors are shown for both cases for three different values, $\alpha = 23.98°, 25.12°$ and $26.27°$. Also shown here are the velocity vectors as well as C_p-distribution on the suction surface for flow without and with MSI. In Fig. A.23, the instantaneous vorticity contours as well as the wall vorticity are shown for configurations II and III. In this figure, results are also plotted for one additional value of $\alpha = 22.83°$. The instantaneous vorticity contours for various a show that the dynamic stall vortex does not develop with MSI activated. Further, the controlled wall vorticity does not show sharp spikes leading to suppresion of the formation of the stall vortex. The results showing the effect of MSI on C_L, C_D, C_M and L/D are most significant, since they show directly whether or not the desired control is achieved. Fig. A.24(a) shows that there is not much significant change in C_L , but as seen in Fig. A.24(b), C_D is considerably reduced by MSI for Case 1 at higher α. Although C_M distribution does not show a clear trend, in Fig. A.24(c), L/D in Fig. A.24(d) increases rapidly as compared to that for the flow without MSI. Finally, controlled modulated suction/injection is also attempted using configuration III, with a more gradual application of MSI control as shown in Fig. A.25. Compared to Case 1, the viscous circulation is sufficiently reduced, for this new Case 3. As before, the velocity vectors as well as C_p-distribution on the suction surface are also plotted. The corresponding instantaneous vorticity contours and wall vorticity are shown in Fig. A.26. The results for Case 3 with its gradually implemented MSI are very similar to those for Case 1. Finally, the effect of gradually applying MSI does not show any significant changes as compared to the standard Case 1.

2.A.6 Conclusion

An unsteady NS analysis is developed using the $(\bar{\omega}_I, \psi_I^D, \Gamma(t))$ formulation. Inclusion of viscous circulation permits accurate treatment of the far-field boundary condition. The implicit ADI-BGE numerical technique provides a uniformly second-order accurate solution, with higher accuracy for the nonlinear convective terms. The grid-independence study showed that, for this constant-rate pitch-up motion in the regimes where the flow is massively separated, the finest-grid solutions still show more than desired deviation from those of the medium grid used here to obtain all the solutions. Also, since the experimental pressure distribution is measured using a limited number of pressure taps, the coarse-grid C_L-distribution agrees well with these results. The role of unsteady separation was discussed by the authors in detail in Ref. [A.12] and is therefore not described here. Based on that earlier description, a modulated suction/injection control strategy was developed and used in this study. The suppression of LE-flow separation provides a very effective means of controlling the formation of the dynamic stall vortex, even with small volumetric suction rate S = -0.00237.

The authors believe that the 2-D analysis developed here is accurate and that any further discrepancies observed are due to three-dimensionality effect. An effort should be made to accurately simulate the three- dimensional flow past this 2-D geometry. Effort is also necessary to incorporate an adaptive-grid refinement in this analysis, in order to obtain higher-Re solutions and also resolve the time scale of the eruption of the secondary structure of $O(Re^{-2/11})$. The three-dimensional analysis should also be coupled with a large-eddy simulation technique in order to obtain higher-Re solutions of greater practical interest.

2.B Three-Dimensional Iterative Technique with Multi-Grid Acceleration

2.B.1 Introduction

Three-dimensional unsteady incompressible flows are of general practical and computational interest. Modern computers have enabled simulation of more complex flows occurring in engineering applications. A number of numerical algorithms have been developed to solve incompressible 3-D Navier-Stokes equations, using either primitive variables or vorticity-based formulations (Refs. [B.6, 11, 21, 22, 23, 24]).

Efforts are regularly pursued for the optimization of numerical simulation techniques to obtain enhanced computational accuracy and efficiency. The present study, thus, is aimed at developing an efficient algorithm for the velocity problem emerging from the vorticity-velocity formulation of 3-D Navier-Stokes equations, using fine grids. Multigrid (MG) techniques have provided an efficient methodology to achieve this. The present sub-section describes the development of an MG method and its application in unsteady three-dimensional incompressible flow simulation using the vorticity-velocity ($\vec{\omega}$-$\vec{V}$) formulation of the Navier-Stokes equations. Second-order accuracy, both in time and space, is obtained via central-differencing the vorticity-transport equations and the elliptic velocity problem.

2.B.2 Vorticity-Velocity Formulation of 3-D Navier-Stokes Equations

The vorticity-velocity ($\vec{\omega}$-$\vec{V}$) formulation, as opposed to the primitive-variable ($\vec{V}$-p) formulation, is selected in the present study because the former has the impressive feature that the spin dynamics of a fluid particle (represented by the vorticity-transport equations) is naturally separated from the kinematic motion of the fluid particle (represented by the elliptic velocity problem). It is recognized that the vorticity is a linear function of velocity, whereas the pressure is a nonlinear function of velocity. Therefore, the resultant numerical methods are easier to deal with, from a computational point of view. Furthermore, with appropriate interpretation of the variables, the vorticity-velocity formulation retains its form even in non-inertial coordinate systems.

As discussed in Refs. [B.13, 18, 19], the non-dimensionalized incompressible Navier-Stokes equations can be written as follows in terms of vorticity-velocity variables in general vector conservation form:

$$\frac{\partial \vec{\omega}}{\partial t} + \nabla \times (\vec{\omega} \times \vec{V}) = -\frac{1}{Re}\nabla \times (\nabla \times \vec{\omega}) \tag{B.1}$$

where Re=$L_R V_R/\nu$ is the Reynolds number, based on an appropriate reference length L_R and velocity V_R.

The kinematic velocity problem (KVP) is formulated directly from the continuity equation and the definition of the vorticity vector:

$$\nabla \bullet \vec{V} = 0, \tag{B.2}$$

$$\nabla \times \vec{V} = \vec{\omega} \tag{B.3}$$

subject to constraints:

$$\iint \vec{V} \bullet \vec{n} dS = 0 \tag{B.4}$$

and

$$\nabla \bullet \vec{\omega} \equiv 0. \tag{B.5}$$

Eqs. (B.4) and (B.5) are necessary and sufficient conditions for the existence of a unique solution for Eqs. (B.2) and (B.3). Consequently, the 3-D velocity problem is completely described and determined by Eqs. (B.2-B.5) and the boundary conditions. It is important to note that the constraint Eq. (B.5) is time-invariant, whereas applying the divergence operator on Eq. (B.1) yields that $\partial(\nabla \bullet \vec{\omega})/\partial t = 0$; together, these ensure that the velocity is determined uniquely for $t > 0$.

The governing equations and constraints, Eqs. (B.1-B.5), are then expressed in a general curvilinear orthogonal coordinate system (ξ^1,ξ^2,ξ^3). Covariant components of both velocity and vorticity are employed. This permits the strong conservation-law form of the governing equations to be maintained and the constraints to be satisfied analytically in the generalized coordinate system. Another significant consequence of the covariant decomposition of both velocity and vorticity vectors is that the generalized form of the curl Eq. (B.3) contains no variable coefficients. Furthermore, the components of the vorticity-transport equation are characterized by the fact that mixed derivatives appearing in the equation for one component (e.g., ω_1-equation) involve only the other two components of vorticity (ω_2 and ω_3); this allows implicit treatment of these terms within an approximately-factored solution scheme (Refs. [B.13, 18, 19]).

2.B.3 Numerical Scheme

Second-order finite differencing is used in the discretization of both vorticity-transport equations and the kinematic velocity problem on a staggered grid. The velocity components are defined at the centroid of, and perpendicular to, the cell surfaces. The vorticity components are tangent to the grid lines and are located at the mid-point of the cell edges. This particular staggered arrangement has the advantage that a set of physically consistent algebraic equations may be derived, that satisfy the constraint Eqs. (B.4) and (B.5).

First of all, The boundary conditions on velocity must be such that the global mass is conserved (Eq. (B.4)). Strong conservation-law form of Eq. (B.2) guarantees that the integral constraint (Eq. (B.4)) will be satisfied if the equation of continuity at each computational cell is satisfied.

Secondly, the discrete counterpart of Eq. (B.5) will be satisfied at any time during the evolution of the flow if it is satisfied initially and the algebraic vorticity-transport equation is solved by a direct method. However, in the present work, the vorticity-transport equations are solved by a modified ADI method developed by Osswald et al. (1988). The approximate factorization creates a splitting error of order $\mathcal{O}(\Delta t^2)$; the time-marching solution of the vorticity field will then be divergence-free up to the same order. Consequently, the convergence of the iterative solution for velocity field will be limited by this error.

For the velocity problem, Osswald et al. (1987) had employed a direct solver, Block Gaussian Elimination (BGE), to compute the velocity field. Due to the limitation of the current core memory of the available supercomputers, application of the direct solver is restricted by the allowable grid size. Therefore, iterative schemes, widely utilized in the solutions of PDE's (Refs. [B.1, 3, 9, 10, 17]) are explored in the present study. Table B.1 compares the requirements of storage between the direct solver BGE and the Multi-Grid Distributive Gauss-Seidel (MG-DGS) iterative algorithm developed in the present study for the velocity problem. It is evident that the iterative method will ease the memory demands. However, iterative methods frequently exhibit slow convergence rates.

Multigrid Method

Multigrid methods can help to accelerate the convergence of the iterative process for the discretized system of Eqs. (B.2-B.3), because the system is of elliptic type Refs.([B.3, B.8]). It is known that any iterative scheme is only effective in its initial stage, when oscillatory (high frequency) error components are dominant. The slowdown thereafter is caused by the ineffectiveness of the relaxation to smooth (low frequency) errors on the current fine-grid. By switching to a coarser grid level, these low-frequency error components will become oscillatory on the coarse grid, and will be smoothed out efficiently by the relaxation.

Although variable coefficients are possible due to coordinate transformation in Eq. (B.2), the system of Eqs. (B.2-B.3) is always linear. As a result, the Correction Scheme (CS) of Brandt (1979, 1984) is employed in the current study. A stable and efficient Distributive Gauss-Seidel relaxation scheme is developed to smooth out oscillatory errors. Only the residuals on the fin~~d~~e grid need be restricted to the coarse grid. The correction is obtained by relaxation on the coarse grid; it is then interpolated (prolongated) back to the fine grid to correct the old fine grid approximation. The restriction, interpolation and coarse-grid operators will be discussed later in the sub-section.

Standard full coarsening is used to define coarser grids. As a result, one coarse computational cell contains eight fine cells. Because of the staggered grid arrangement, the coarse-grid function locations never coincide with the locations of the fine-grid functions. The Multigrid cycles used in the present study are interacted adaptively (Accommodative Cycle). Since the flow in the present study is time dependent, the iterative solution of the velocity field is repeated at each temporal step. The solution at the previous time step serves as a good approximation for the solution at the new time step. Thus, the MG cycle starts at the finest grid, visiting the coarser grids successively to obtain the correction.

Relaxation Scheme

To arrive at a fast MG algorithm, the discretization of the boundary-value problem should be stable in the first place. The central differencing scheme on the staggered grid used in the present study for the velocity leads to finite-differenced equations that are stable and elliptic (Ref. [B.3]).

The standard pointwise Gauss-Seidel (GS) relaxation is usually efficient for a single equation. However, the discretized system for the velocity problem does not contain a one-to-one correspondence between the unknowns and the equations. The equations are coupled to each other, and therefore, a pointwise GS scheme would not work effectively. An alternate scheme, Distributive Gauss-Seidel (DGS) scheme, is thus recommended for systems of equations (Ref. [B.1]). In the DGS scheme, each discretized equation in the system is satisfied in turn by *distributing* its residual to all the unknown variables associated with this equation. This is done in such a way that the residuals of the remaining equations are kept unaltered. Mathematically , the system for Eqs. (B.2-B.3), can be written symbolically as a matrix operator form $L\vec{V} = \vec{f}$ with $L = (\nabla\bullet, \nabla\times)^T$. It is then reformulated as follows:

$$L\overline{L}\vec{w} = \vec{f}, \tag{B.6}$$

where the operator $L\overline{L}$, preferably, has a diagonal (or block diagonal) structure. The Gauss-Seidel iteration is then formulated with respect to the new unknown $\vec{w}$ (called "ghost unknown" by Brandt (1984). A new iteration $\vec{V} = \overline{L}\vec{w}$ will yield the original-grid function $\vec{V}$. In fact, the new unknown w is neither stored nor calculated in the actual program.

The advantage that the DGS scheme gains is that $L\overline{L}$ usually possesses better smoothing rate than L itself. For the present velocity problem, the operator $L\overline{L}$ will become

$$L\overline{L} = \begin{bmatrix} \nabla^2 & 0 \\ 0 & \nabla\times\nabla\times \end{bmatrix} \tag{B.7}$$

if $\overline{L}$ is chosen as $(\nabla, \nabla\times)$. It is seen that the operator $L\overline{L}$ contains the second-order Laplacian; better smoothing rate is expected when relaxing Eq. (B.6).

Specifically, the continuity equation is scanned and satisfied, while keeping unchanged the residuals of all neighboring curl equations. The distributed amount should be suitably modified for boundary cells where only interior velocities are updated to satisfy the continuity equation for the boundary cells. Red-Black ordering is employed for the relaxation of the continuity equation to achieve vectorization.

For the curl equations, the present DGS scheme groups all three curl equations and relaxes them simultaneously in the prescribed order, keeping all the residuals of the neighboring continuity equations unchanged. Although the scheme turns out to be a little cumbersome algebraically, the principle is exactly the same as for relaxing the continuity equation. Four-color ordering is used to eliminate data dependence, and achieve vectorization of the relaxation sweep for all three curl equations.

Lexicographic ordering is also used in the present study as well as red-black/four-color ordering. It is found that the smoothing rates for both orderings differ very little for the present velocity problem.

Interpolation I_{M-1}^{M}

The operator I_{M-1}^{M} interpolates the coarse-grid $(M-1)$ function to the fine grid (M). The order of the interpolation should be dictated by the order of the difference (or differential) equations (Refs. [B.1, B.8]). In addition, the integral constraint, Eq. (B.4), must be satisfied on all grid levels so that consistency is maintained. Trilinear interpolation for the interior grid points and linear interpolation for the near-boundary points are constructed to fulfill these requirements. Each of the three velocity components is interpolated separately. Then, the interpolation for $V1$ follows:

$$I_{M-1}^{M} V1_{ijk}^{M-1} = \frac{1}{16}(9V1_{ijk}^{M-1} + 3V1_{ij+1k}^{M-1} + 3V1_{ijk+1}^{M-1} + V1_{ij+1k+1}^{M-1}), \quad \text{(interior)}$$

$$I_{M-1}^{M} V1_{ijk}^{M-1} = \frac{1}{4}(3V1_{ijk}^{M-1} + V1_{ij+1k}^{M-1}), \quad \text{(boundary)}$$

$$I_{M-1}^{M} V1_{ijk}^{M-1} = V1_{ijk}^{M-1} \quad \text{(corner)} \quad \text{(B.8)}$$

for the fine-grid variables on the coarse-grid plane, and

$$I_{M-1}^{M} V1_{i+1jk}^{M-1} = \frac{1}{2}(I_{M-1}^{M} V1_{ijk}^{M-1} + I_{M-1}^{M} V1_{i+2jk}^{M-1}) \quad \text{(B.9)}$$

for the fine-grid points on the plane between two coarse-grid planes. Similar expressions are developed for the $V2$ and $V3$ components. In case of variable coefficients as a result of non-uniform grid, the variable $V1$ in Eqs. (B.8-B.9) should be taken as the product of the V_1 and the corresponding coefficient. Such a scheme ensures that the integral constraint is satisfied on all grid levels.

Restriction I_{M}^{M-1}

In the Correction Scheme, only residuals need to be transferred to coarser grids. Full weighting, which averages all of the neighboring fine-grid residuals, is especially important for difference equations with varying coefficients. This is exactly the case for the velocity problem in the present study. Thus, full weighting (FW) residual transfer is constructed for all the residuals in the study.

As the finite-difference equations for the velocity problem are centered at different locations, residuals are transfered separately for each equation. Specifically, for the continuity equation, the restriction operator is:

$$I_M^{M-1}(r_d)_{ijk}^M = \mu_i^M \mu_j^M \mu_k^M (r_d)_{ijk}^M, \tag{B.10}$$

where $\mu_i^M f_{ijk}^M = \frac{1}{2}[f_{i-\frac{1}{2}jk}^M + f_{i+\frac{1}{2}jk}^M]$ is the mid-point average operator for any grid function f_{ijk}^M at level M, and r_d is the residual of the continuity equation. The coarse-grid source term for the continuity equation is thus the average of the neighboring eight fine-grid residuals.

Similarly, the full weighting for the residual transfer of $W1$ (discretized ω_1) component of the curl equation is written symbolically as:

$$I_M^{M-1}(r_{W1})_{ijk}^M = \mu_j^M \mu_k^M \mu_j^M \mu_k^M \mu_i^M (r_{W1})_{ijk}^M. \tag{B.11}$$

This says that the coarse-grid source term $W1_{ijk}^{M-1}$ is the weighted average of the eighteen neighboring fine-grid residuals. The residuals for $W2$ and $W3$ components of the curl equation are treated in a similar manner.

The above restriction operator also preserves the two compatibility conditions, given by Eqs. (B.4) and (B.5), throughout all the coarse-grid levels, as long as they are met on the finest grid.

Coarse-Grid Operator L^{M-1}

The guideline in constructing the coarse-grid matrix operator L^{M-1} is that L^{M-1} should be a proper homogenization of the fine-grid operator L^M. One way to achieve this is to define L^{M-1} in the same manner as L^M from the corresponding differential operators. This approach is employed in the present study. Therefore, no additional computations are needed for defining L^{M-1}, except when varying coefficients occur in Eq. (B.2) because of coordinate transformation. In this case, some appropriate averaging is needed to define the coarse-grid coefficients. Since the varying coefficients for the fine-grid are due to the coordinate transformation, the weighted average of the fine-grid coefficients is naturally a proper definition for the coarse-grid coefficients, and thus for the coarse-grid operator L^{M-1}. The so-called minimal weighting (Ref. [B.3]) is employed for forming the coarse-grid coefficients, as for example,

$$G11_{ijk}^{M-1} = \mu_j^M \mu_k^M G11_{ijk}^M \tag{B.12}$$

where $G11_{ijk}$ is the discretized metric coefficient occurring in Eq. (B.2) due to coordinate transformation.

2.B.4 Model Velocity Problem

Numerical experiments have been conducted using the DGS relaxation scheme developed together with the MG procedure. A test function $cos(sin(xyz))$ is used to generate a 'velocity' field in the Cartesian domain. The divergence and curl of this vector field are then computed using the discretized form of the governing equations (Eqs. (B.2-B.3)) and provide the appropriate source terms for these equations. Then, the multigrid method developed is used to solve these equations with modified source terms and determine 'velocity' field, starting with an appropriate initialization (zero is taken in the present test case), until the prescribed convergence criterion is satisfied. Both uniform and non-uniform grids have been used. The non-uniform grids were generated by algebraic clustering.

Figures B.1-B.3 demonstrate graphically how the MG-DGS scheme improves the convergence rate, relative to the single-grid (SG) results, for both uniform and clustered (25 x 25 x 25) grids. Table B.2 gives some numerical values for the MG-DGS scheme for several uniform and non-uniform grids.

It is seen that the CPU time increases linearly and the convergence rate is maintained at about $0.42/WU$ for uniform grids with the size increasing from $(25\times25\times25)$ to (33 x 33 x 33) to (49 x 49 x 49). Similar results are obtained for non-uniform (25 x 25 x 25) and (33 x 33 x 33) grids with moderate clustering. The expected multigrid convergence rate is obtained. The convergence rate μ in Table B.2 is the average of the total rate defined by:

$$\mu = \left(\frac{\| r \|_{final}}{\| r \|_{initial}}\right)^{1/WU}$$

where the norm $\| \cdot \|$ is defined as the root-mean-square of the residuals and WU is the number of work units executed.

It is seen that when varying coefficients occur, as a result of grid clustering, the asymptotic convergence rate degrades slightly. Grid spacings for non-uniform grids used in Table B.2 have differences of one order of magnitude. The deterioration is greater for the case with more highly varying coefficients. This is demonstrated in Fig. B.3, where the minimal spacing is of order $\mathcal{O}(10^{-3})$ and maximal spacing is of $\mathcal{O}(10^{-1})$; i.e., a difference of two orders of magnitude exists in the coefficients. Further numerical experiments with different test functions indicate that the convergence also depends upon the nature of the velocity field itself. It is noted that the clustering is strong near the boundary (wall) of the domain because high gradients of the flow variables (vorticity and velocity) are expected here in the actual viscous flows. Figure B.4 shows the convergence history obtained from the actual flow simulation for the 3-D shear-driven cavity of aspect ratio unity using the same clustering as in Fig. B.3. Desirable convergence rate is observed for this strongly clustered grid (two orders of magnitude difference), thereby demonstrating the robustness of the MG-DGS scheme.

2.B.5 Some Physical Aspects of Unsteady 3-D Shear-Driven Flow

Shear-driven flow in a cavity has drawn much attention in the fluid dynamics community because of its richness of flow structure and complexity of dynamical phenomena, as well as the simplicity of its geometry and well-defined boundary conditions. Careful experiments have been conducted by Koseff and Street (1984), among others, to study the characteristics of this flow. The cavity has also been chosen as a benchmark test by many CFD practitioners; for example, Refs. [B.7] and [B.21], for both 2-D and 3-D flow simulations.

The shear-driven cavity flow has many complex flow structures. Multiple recirculation ~~zones~~ exist as a result of strong viscous effects exerted by the walls and the sharp corners in the geometry. Of special interest are the three dimensionality and the longitudinal vortices. Efforts are made in the present study to investigate the 3-D cavity flow using the MG-DGS method to validate the method as well as to study the flow itself.

Figure B.5 depicts the configuration of the 3-D shear-driven cavity flow. The upper wall $ABFE$ is impulsively set in motion in the direction parallel to itself. The flow is thus symmetric with respect to the mid-span plane. The typical time-averaged flow pattern in the symmetry plane is shown, schematically, in Fig. B.6. The flow exhibits three significant recirculation regions, in addition to the primary vortex: the downstream secondary vortex, the upstream secondary vortex and the upper-surface secondary vortex. These features make this flow a benchmark model for testing numerical methods for incompressible viscous flows.

The formation of these recirculation regions is the result of the wall friction and the stagnation induced by the corner. Moreover, the separation zone downstream provides a *concave* boundary for the primary flow coming down from above. This suggests the occurrence of the Taylor-Görtler-like (TGL) vortex above the separation surface. The phenomenon was, indeed, observed in the experimental study by Koseff et al. (1983, 1984). These vortices are susceptible to instability; they may eventually lead to transition at higher Reynolds number.

Examination of TGL Vortices

In an attempt to capture the TGL vortices, a case with higher Reynolds number $Re = 3300$ is investigated. The spanwise aspect ratio is 3:1. This corresponds to the experimental setup used in Ref. [B.14]. Figure B.7 shows the visualization results obtained by Koseff et al. (1983). The TGL vortices in the lateral plane at $x^1 = 0.8$ are clearly seen in Fig. B.7(b).

To resolve the viscous boundary layer near the wall and the shear layer at the upper surface, a non-uniform ($65 \times 65 \times 33$) grid is generated, with clustering in the x^1 and x^2 directions. The total core storage requirement for this grid size, using the ADI+MG-DGS method, is about 5 megawords. A time step of $\Delta t = 0.01$ is used in the marching solution for the unsteady flow. The convergence criterion for the finest grid for the MG-DGS method for the velocity problem is taken to be 5×10^{-7}. Table 3 lists the CPU index for the flow simulation; comparison is also made with the BGE method (Ref. [B.19]) for the ($25 \times 25 \times 25$) uniform grid at $Re = 400$.

Figures B.8-B.9 show the results of the flow simulation for the 3-D cavity with 3:1 spanwise aspect ratio and $Re = 3300$. The flow is computed until characteristic time

$T = 21$. The steady state has not yet been reached; it is also likely that a steady state may not exist for this Reynolds number.

The flow pattern shown in Fig. B.6 in the symmetry plane is recovered numerically in Fig. B.8. It is evident that major recirculation zones are developing at the downstream lower endwall, upstream lower endwall and upper surface corner. However, the separation at the upper surface is not strong at this stage. It is found that the viscous boundary layer and the upper surface shear layer are resolved well with the clustered (65×65) grid in the symmetry plane for $Re = 3300$. Table B.4 lists the sizes of the downstream secondary eddy at $T = 15, 17$ and 21; the corresponding time-averaged experimental result (Ref. [B.15]) is also included.

Figure B.9 shows the temporal development of the longitudinal vortices at the lateral planes $x^1 = 0.5$. The results show strong 3-D effects developing in the flow. Two pairs of TGL vortices have obviously developed above the bottom wall. It is noted that these vortices started near the endwall and developed towards the central region. This indicates that, in addition to the downstream concave separation surface, three-dimensionality is influential in the formation and development of the longitudinal vortex. It can also be seen in these figures that, to counteract these TGL vortices, sub-vortices of smaller sizes are generated very close to the wall. Moreover, longitudinal vortices also develop near the upper surface. It is deemed that the strong viscous shear layer and three-dimensionality are responsible for the occurrence of these longitudinal vortices. It is observed that the spanwise grid size (33) is not sufficient to resolve both the boundary layer near the endwalls and the shear layers forming thereafter in the interior of the flow. Evidently, the spanwise grid should also be clustered near the walls.

Examination of Streamwise-Vorticity Transport

Amongst the physical phenomena associated with the 3-D flow in a driven-cavity with finite span is the transport of streamwise vorticity, which is very important in helping understand the fundamental physics of the interaction between the main flow and the secondary flows. Therefore, effort was directed at carefully examining the flow structure in the spanwise direction, in an attempt to gain meaningful information about the flow.

To help reduce CPU time and core storage, the computational domain used consists of only one half of the cavity (see Fig. B.9) with a non-uniform staggered grid ($65 \times 65 \times 49$). Symmetry boundary conditions are used at the symmetry plane $z = 0$. The Reynolds number of 3200 is based on the velocity (V_R) of the top surface in x-direction and the depth (L_R) of the cavity. The flow is started impulsively from rest with the time-step $\Delta t = 0.005$.

Symmetry Plane $z = 0$

The 2-D flow will develop in the symmetry plane $z = 0$ when a cavity of infinite span is used and Taylor-Görtler instability associated with a rotating flow is neglected. Numerous 2-D simulations are available. Examination of the 3-D flow pattern in this plane will reveal and compare the fundamental differences between the symmetry-plane results for 3-D and 2-D flow.

The results are illustrated in Fig. B.10 using tangential velocity and contours of normal vorticity ω_z in the symmetry plane, for the time instants t = 20, 25, 30, 35, 45 and 50.

As of $t = 20$, the flow pattern in the symmetry plane shows 2-D characteristics. A primary vortex forms in the central region and three major secondary eddies near the upper back-wall, lower back-wall and lower front-wall. The three-dimensional effect has not yet influenced the flow in this plane.

Between time $t = 20$ and $t = 25$, a threshold has evidently been past. The flow pattern at $t = 25$ clearly demonstrates the 3-D effects. Three spanwise 'jets' in the positive z-direction, representing the Taylor-Görtler-like (TGL) vortices, impinge onto the symmetry plane. They interact with the already-formed primary vortex and the three seconday vortices in the symmetry plane and drastically change the flow pattern. It is seen that these three spanswise streams are, respectively, near the three secondary vortices in the symmetry plane, with the one near the lower front-wall being the strongest. This suggests that the three-dimensionality is strongest near the wall and three secondary eddies. It follows that these effects have resulted from the relatively large shear stresses and adverse pressure gradients in these regions. As the secondary vortex near the lower front-wall and the primary flow above it are the strongest among the three secondary eddies in the symmetry plane, the generation and transport of the 'streamwise' vorticity, namely, the vorticity with its axis aligned approximately with the primary (dominant) flow direction, is expected to be the most significant. The interference of the spanwise motion reshapes the flow characteristics in the symmetry plane, enhancing the momentum transfer in some region and depressing it in others.

As the flow evolves to $t = 30$ and, further, to $t = 35$, the effects of three-dimensionality become more obvious and significant, particularly near the lower front-wall. It is noted that the spanwise stream near the lower front-wall vortex is moving towards the front wall. This reflects the fact that the size of the secondary vortices near the lower front-wall is decreasing with the increase of the spanwise motion during this period. It suggests that the streamwise vortices are generated and transported in such a way that they adjust themselves to the strength of primary flow and the location of the separation. Experimental results of Prasad et al. (1988) have also shown this strong interaction between the secondary eddies and the TGL vortices. It should be noted that the mesh in the central region of the symmetry plane is not refined enough to resolve the shear layers that develop there at these two times, as shown by the vorticity contours.

At $t = 45$, the 3-D pattern is not as significant as seen during $t = 25 - 35$. This reveals the unsteady nature of the TGL vortices. At $t = 50$, the 3-D flow pattern takes on a different look. The primary flow near the bottom wall is more leveled. A saddle point has formed near the lower back-wall as a result of the interaction of this flat primary flow stream, the back-wall and spanwise motion of the fluid. The spanwise motion at this stage near the lower front-wall is not as strong as at $t = 35$.

Although the above analysis deals with the flow structure in the symmetry plane, the emphasis has been stressed on the interaction of the spanwise motion (streamwise vortices) with the flow-field in the symmetry plane. The flow pattern in the symmetry plane is completely different from that of 2-D simulations. Spanwise motion of the fluid evolve and interact actively with the primary and the secondary flows in the symmetry plane (as well as all x-y planes).

Vertical Spanwise Planes $x = 0$ and $x = .265$

The flow in the vertical spanwise planes (y-z planes) is solely due to three-dimensionality, namely, the end-wall effects and the Taylor-instability mechanism. Prasad et al. (1988) has shown that a sufficiently larger spanswise aspect ratio is also a necessary condition for the existence of TGL vortices. The experiment of Koseff and Street (1984) indicated that unsteady nature of TGL vortices were obvious for the cavity with a spanwise aspect ratio of 3 : 1.

For separated flows with end-walls in the spanwise direction, it is known that "corner vortices" appear near the end-walls. These vortices are created by an adjustment of the shear and pressure forces acting on the recirculating fluid to the no-slip condition imposed by the solid boundaries (Ref. [B.4]). The spanwise motion of the fluid within the secondary eddies in the x-y planes is driven by these corner vortices. Observations of the flow pattern in the symmetry plane in the previous sub-sub-section have confirmed that the TGL vortices are very strong near the wall and the secondary eddies in the symmetry plane.

Figure B.11 depicts the normal vorticity (ω_x) contours in the vertical spanwise planes $x = 0$ and $x = .265$ for times $t = 20$ through $t = 50$. It is clearly seen that the corner vortices have originated near the end-wall $z = -\frac{3}{2}$ at $t = 20$. The vortices also began shedding towards the center region. But they have not yet penetrated into the symmetry plane ($z = 0$). This is consistent with the observation of the 2-D flow structure in the symmetry plane in the previous sub-sub-section. Although some vortices are present near the symmetry plane at this stage, they are not strong enough to affect the flow pattern in the symmetry plane.

At $t = 25$, one and half pair of TGL vortices are seen near the symmetry plane. Three-dimensional effect has arrived at the symmetry plane. The 2-D pattern in the plane has been disrupted. It is true, as anticipated, that the TGL vortices at $x = .265$ are stronger than those at $x = 0$ since the location $x = .265$ is in the vicinity of the lower front-wall secondary eddy in the $x - y$ plane. It is also observed that there are some very weak vortices in the middle sub-section of the plane, suggesting that the vortices near the symmetry plane might have transported from 'upstream' locations like $x = .265$, where the TGL vortices developed earlier. It is interesting to note that one and half pair of vortices also appear near the top surface and that their axes align with those near the bottom wall approxmately in the x-y planes at $x = 0$ for $t = 25$. This may imply that the primary vortex in the x-y planes possesses a structure called a 'cell' observed experimentally by Mochizuki et al. (1990) at this stage. The 'cell' consists of a pair of counter-rotating vortex rings of the primary vortex and the horseshoe-like secondary vortex ring near the bottom wall. However, this structure is not obvious at later times. This is due to the fact that the experimental setup employed a larger span (aspect ratio as large as 12) and lower Reynolds number ($Re = 1000$). It is then concluded that the 'cell' structure will not sustain for the cavity with an aspect ratio 3 : 1 at $Re = 3200$.

The sizes and the locations of the streamwise vortices change with time, as presented by the vorticity contours in those two planes through $t = 50$. The number of vortices are increasing in both planes. The vortices in the plane $x = .265$ seem stronger than those in the plane $x = 0$. At the same characteristic time, there are more pairs of vortices in the plane $x = .265$ than in the plane $x = 0$. It is shown again that streamwise vortices near the secondary eddies in x-y planes are stronger. Unsteadiness of the flow at this Reynolds number $Re = 3200$ is again vividly illustrated by the streamwise vorticity changes.

SUMMARY

A multigrid distributive Gauss-Seidel (MG-DGS) method has been developed and successfully applied to the simulation of unsteady three-dimensional incompressible flow in the shear-driven cavity. The MG-DGS method for the velocity problem has proved to be efficient and robust. The DGS relaxation scheme itself is very efficient for smoothing the high-frequency errors for the first-order elliptic system for the velocity problem. For uniform grids, convergence rate of about 0.5 is achieved using accommodative multigrid procedures.

Three-dimensional shear-driven cavity flow at Reynolds number $Re = 3300$ has been simulated using the presently developed MG-DGS scheme together with an ADI algorithm. The longitudinal vortices occurring in cavity-flow experiments have been captured numerically. Driven-cavity flow with finite span is definitely three-dimensional. End-walls play a dominant role in creating streamwise vortices (TGL vortices). The streamwise TGL vortices interact strongly with primary and secondary vortices in the x-y planes. The evolution and transport of streamwise vorticity alters the structure and sizes of the primary and secondary vortices in the symmetry plane (and all other x-y planes). The flow is persistently unsteady for $Re = 3200$ through $t = 50$. The flow structure observed in the numerical simulation is in good agreement with available experimental observations.

2.C Adaptive Grid Technique for Higher-Re Flows

2.C.1 Abstract

The **objective** of this study is to efficiently simulate vortex-dominated highly unsteady flows. In such flows, the locations as well as the extent of the regions requiring fine-mesh resolution vary with time. A technique has been developed to simulate these flows on a temporally adapting grid in which the adaption is based on the evolving flow solution. The flow in an axisymmetric constriction has been selected as an illustrative problem. The multiple and disparate length scales inherent in this complex flow make this problem ideally suited for evaluating the adaptive-grid technique. Adaption is based on the equidistribution of a weight function, through the use of forcing functions. The significance of this is that the method can be implemented into existing flow-analysis systems with minimal changes. The grid-generation equations developed are viewed as grid-transport equations. The time-dependent control functions perform the role of the convective speed in this transport mechanism. The equations provide the efficiency and flow tracking capability of parabolic equations, while maintaining the smoothness of computationally expensive elliptic equations. The efficiency and flow tracking capability of the approach is demonstrated for both steady and unsteady flows.

2.C.2 Background

The use of appropriate coordinates in the mathematical formulation of a problem has a dominant effect on the accuracy and computational resource requirements of analysis and numerical simulation of fluid flow problems. In addition to requiring that the coordinates be boundary-oriented, it is desirable that they also reflect some of the significant features of the flow. Traditional grid-generation methods rely on the experience of the user and only partial a priori knowledge of localized or transient physical phenomena which require a fine mesh for their accurate representation. The objective of the present work is to develop an efficient flow-simulation technique, which automatically resolves critical regions of widely disparate length scales. A major advantage of a time-dependent mapping incorporating the evolving flow physics is its ability to cluster coordinate lines only where necessary at that instant, thus reducing meshpoint requirements. This feature is particularly useful for strongly unsteady flows, in which the same flow regions do not require fine resolution at all instants of time. For flows requiring fine resolution throughout the domain, such as intensely mixing turbulent flows, the advantage is greatly diminished, if not eliminated. Several review papers such as by Thompson (1985), Eiseman (1985) and Anderson (1987) present applications where significant improvements in accuracy and efficiency have been obtained through the use of adaptive-grid procedures. Many of the procedures require the solution of elliptic systems for each grid regeneration, as done, for example, by Kim and Thompson (1990) and in the variational approach of Brackbill and Saltzman (1982), rendering the procedure rather costly for truly transient problems. Bockelie (1988) and Trompert (1990) have developed techniques for transient problems based on iterative procedures requiring multiple grid subdivisions for each grid regeneration or time level advancement. The present adaptive-grid technique draws on the error-equidistribution concept of Anderson (1987), together with the widely used Poisson generation system of Thompson (1974), with the important modification that the equations governing the grid evolution are parabolic in time. These grid-transport equations fit well into the flow solution procedure and allow grid regeneration at every time level, with reasonable computational requirements.

In the following sections, the equations governing the flow are expressed in generalized time-dependent coordinates, and the grid-transport equations and weight functions are derived. The numerical procedure is described briefly and results are presented and discussed for a model problem of an axisymmetric internal flow.

2.C.3 Flow Governing Equations in Generalized Time-Dependent Coordinates

The present analysis considers time-dependent flows of incompressible, Newtonian and constant-viscosity (ν) fluids. Therefore, the incompressible unsteady Navier-Stokes equations are the appropriate governing equations. Written in terms of the vorticity vector $\overline{\omega}$ and the velocity vector $\overline{v}$, these equations consist of a temporally parabolic vorticity-transport equation given as

$$\frac{\partial \vec{\omega}}{\partial t} + (\vec{v}\cdot\nabla)\,\vec{\omega} = (\vec{\omega}\cdot\nabla)\,\vec{v} - \frac{1}{Re}(\nabla\times\nabla\times\vec{\omega}), \tag{C.1}$$

with the following kinematic definition for vorticity:

$$\vec{\omega} = \nabla\times\vec{v}. \tag{C.2}$$

Equations (C.1) and (C.2) have been non-dimensionalized using L_R as the characteristic length, U_R as the characteristic speed, L_R/U_R as the characteristic time, and U_R/L_R as the characteristic unit of vorticity. The Reynolds number, Re, is based on U_R and L_R to be defined later for the flow problem studied.

The axisymmetric flows considered involve only two independent spatial dimensions. Hence, the mass-conservation equation is identically satisfied by the introduction of the Stokes stream function, ψ, related to the local velocity vector as

$$\vec{v} = \nabla\psi \times \vec{e}^{3}, \qquad (C.3)$$

where $\vec{e}^3$ is the fundamental contravariant base vector locally normal to the (x,r) meridional plane, (Fig. 1).

The governing equations (C.1)-(C.3) are in general vector form. For application purposes, a coordinate system must be selected and Eqs. (C.1)-(C.3) represented in scalar component form. The boundary-oriented time-dependent 'computational coordinates' (ξ^1,ξ^2,ξ^3,τ) to be employed are defined through an admissible coordinate transformation T. The implementation of axisymmetry is simplified by using a transformation of the following form,

$$\begin{aligned} x^1 &= x^1(\xi^1,\xi^2,\tau) \\ x^2 &= r(\xi^1,\xi^2,\tau)\cos(\xi^3) \\ x^3 &= r(\xi^1,\xi^2,\tau)\sin(\xi^3)\,. \end{aligned} \qquad (C.4)$$

The physical space is represented by the basic Cartesian coordinate system, (x^1,x^2,x^3) or (x,y,z), while ξ^1 and ξ^2 represent the generalized curvilinear coordinates in a given meridional plane, and ξ^3 represents the transverse or azimuthal coordinate ϕ describing the various meridional planes, (Fig. C.1).

In terms of the stream function defined in Eq. (C.3), the definition of vorticity given by Eq. (C.2) expressed in generalized coordinates (Osswald [1983]) becomes:

$$\frac{1}{\sqrt{g}}\left[\frac{\partial}{\partial\xi^1}\left(\frac{-g_{21}}{\sqrt{g}}\frac{\partial\psi}{\partial\xi^2}+\frac{g_{22}}{\sqrt{g}}\frac{\partial\psi}{\partial\xi^1}\right)+\frac{\partial}{\partial\xi^2}\left(\frac{g_{11}}{\sqrt{g}}\frac{\partial\psi}{\partial\xi^2}-\frac{g_{12}}{\sqrt{g}}\frac{\partial\psi}{\partial\xi^1}\right)\right] = -\omega^3, \qquad (C.5)$$

where

$$g_{i,j} = \sum_{k=1}^{3}\left(\frac{\partial x^k}{\partial\xi^i}\right)\left(\frac{\partial x^k}{\partial\xi^j}\right), \qquad g = \det(g_{i,j})\,. \qquad (C.6)$$

The defining equation (C.5) for ω^3 constitutes an elliptic partial differential equation governing the development of the axisymmetric-flow stream function.

The vorticity-transport equation, Eq. (C.1), expressed in terms of the generalized coordinates and written in strong conservation-law form, is as follows (Thornburg [1991]):

Equations (C.5)-(C.7) comprise the flow governing equations in generalized time-dependent coordinates. The next section presents the grid-transport equations used to define the coordinate transformation given by Eq. (C.4).

2.C.4 Grid-Transport Equations

To facilitate the determination of accurate flow solutions, the physical domain of arbitrary shape is transformed into a computational domain of regular rectangular shape, such that a uniform

$$
\begin{aligned}
&\frac{\partial}{\partial \tau}(\sqrt{g}\,\omega^3) - [(x_\tau r_\eta r - r_\tau x_\eta r)\,\omega^3]_\xi + [(x_\tau r r_\xi - r_\tau r x_\xi)\,\omega^3]_\eta \\
&\quad + \frac{\partial}{\partial \xi^1}\left(\omega^3 \frac{\partial \psi}{\partial \xi^2}\right) - \frac{\partial}{\partial \xi^2}\left(\omega^3 \frac{\partial \psi}{\partial \xi^1}\right) \\
&\quad = \frac{1}{Re}\left\{ \frac{\partial}{\partial \xi^1}\left[\frac{g_{22}}{\sqrt{g}} \frac{\partial}{\partial \xi^1}(g_{33}\omega^3) - \frac{g_{21}}{\sqrt{g}} \frac{\partial}{\partial \xi^2}(g_{33}\omega^3)\right] \right. \\
&\quad \left. + \frac{\partial}{\partial \xi^2}\left[\frac{g_{11}}{\sqrt{g}} \frac{\partial}{\partial \xi^2}(g_{33}\omega^3) - \frac{g_{12}}{\sqrt{g}} \frac{\partial}{\partial \xi^1}(g_{33}\omega^3)\right] \right\} .
\end{aligned}
\tag{C.7}
$$

computational mesh corresponds to an appropriately distributed physical grid. The goal is to incorporate the developing solution variables into the evolving transformation such that the available grid points are distributed in a manner that represents the physical solution with the 'best' possible accuracy. This leads to the search for the relationship between the developing physical solution and the corresponding grid distribution. Unlike the well defined conservation laws governing fluid flow, there is no unique physical law governing the relationship between the solution and the best grid.

The requirement of strong smoothing properties and tendency towards uniformity suggests that a law elliptic in nature would be most appropriate. However, Laplace's equation, the simplest elliptic equation, provides no control over grid spacing. Grids generated by Poisson equations achieve non-uniform spacing enforced by the non-homogeneous terms, called forcing functions in this context; for examples, see Thompson (1985b). To develop a time-dependent transformation, these forcing functions can be based on the evolving flow solution. For each time step, grid regeneration would require the solution of an elliptic system. This does not seem practical for a truly unsteady flow situation.

For unsteady flow problems, such as the one considered in the present study, the flow-transport equations are parabolic in time and elliptic in space. Thus, a parabolic law governing the grid motion, that could be integrated in time along with the flow transport equations, would fit well with the solution procedure. Grid generation methods based on parabolic systems provide computational efficiency, but often sacrifice grid smoothness and control over clustering.

Ghia, Ghia and Shin (1983) developed a grid generation system by setting to zero the coefficient of the convective term in the two-dimensional Navier-Stokes equations in the transformed plane. The equations thus obtained have the form of a transport equation. Their procedure then employed the time-dependent method in order to march both the flow and the grid equations to steady state. In that work, the flow velocities were used to drive the grid movement. It has been recognized (Anderson [1987]) that the Poisson equation of Thompson (1974) in the transformed plane can be rearranged into a transport-equation form by the addition of a temporal derivative. Therefore, the grid equations are written as follows:
The time-dependent control functions perform the role of the convective speed for the grid-transport mechanism. This allows the grid to be advanced in time, along with the parabolic flow-transport equation. The grid equations are dynamically coupled with the evolving flow field through the P and Q terms.

$$
\begin{aligned}
-J^2[Px_\xi + Qx_\eta + x_\tau] &= \alpha x_{\xi\xi} - 2\beta x_{\xi\eta} + \gamma x_{\eta\eta}, \\
-J^2[Pr_\xi + Qr_\eta + r_\tau] &= \alpha r_{\xi\xi} - 2\beta r_{\xi\eta} + \gamma r_{\eta\eta}.
\end{aligned}
\qquad (C.8)
$$

Approximate Equidistribution through Forcing Functions

The equidistribution of a weight function on a mesh is the main concept of the present adaptive grid scheme. It has been recognized (Anderson [1987]) that a one-dimensional equidistribution law may be written as a Poisson system,

$$x_{\xi\xi} + Px_\xi = 0, \quad with \quad P = \frac{w_\xi}{w}. \qquad (C.9)$$

Using variational calculus, equidistribution laws may be similarly written for higher dimensions. In order to simplify the equations and reduce the computational requirements, the problem is viewed as a series of one-dimensional equidistribution schemes. The individual forcing functions are combined to yield the forcing function for multiple dimensions as

$$P^k = \frac{w_\xi^k}{w}, \qquad k = 1,2,3. \qquad (C.10)$$

Equations (C.8) and (C.10) provide an approximate equidistribution law based upon the individual weight functions. The development of the weight functions for the individual coordinate directions is described in the following section.

Derivation of Weight Functions

Grid spacing is inversely proportional to the weight function, and hence, the weight function determines the grid distribution. The weight function used in the present work is an approximation to the truncation error. Determination of this function is one of the most challenging areas of adaptive grid generation. It is believed that the function developed in the present work represents a significant contribution in this area. For a kth-order accurate simulation, the leading term in the truncation error for convective-like derivatives is of the form $h^k \phi^{(k+1)}$, where h is the local mesh spacing, ϕ is the solution variable and $\phi^{(k+1)}$ is the (k+1)th derivative of ϕ; similarly for diffusion-like derivatives it is of the form $h^k \phi^{(k+2)}$. If a flow simulation is to benefit from non-uniform spacing, the flow must contain regions of non-uniform derivatives. An equidistributional scheme will result in non-uniform spacing when $\phi^{(k+1)}$ varies over the solution domain. Non-uniform spacing will lead to the greatest benefit when the variation in $\phi(k+1)$ is largest. This suggests the use of derivatives in developing the weight function. Evaluation of higher-order derivatives from discrete data is progressively less accurate and subject to noise. However, variation in the derivative $\phi^{(k+1)}$ implies that lower-order derivatives also vary. In fact, if $\phi^{(k+1)}$ varies rapidly, ϕ^k can be large. When $\phi^{(k+1)}$ varies widely, the lower-order derivatives must be non-zero in the vicinity of wide variation, and are proportional to the rate of variation. Therefore, it is possible to employ some lower-order derivatives as a proxy for the truncation error.

Experience with flow simulation also sheds light on flow regions requiring fine resolution. Thus, Flow regions of large gradients require finer resolution than more uniform flow regions, as can be deduced from the above discussion. Also, regions of large solution variable curvature, which necessarily occur between regions of high and low gradients, require resolution. Many researchers have successfully employed weight functions composed of solution variable gradient and curvature (Anderson [1987], Thompson [1985]). Ghia, Ghia and Shin (1983) have clearly demonstrated the importance of properly resolving regions of large solution variable curvature for some model problems. The present weight functions employ higher-order derivatives of the physical velocity variables u and v through the derived variable of vorticity. The choice of vorticity is logical, as vorticity provides a physical description of the rotational intensity of the flow. One difficulty in the use of vorticity for constructing the weight function is that it may vary over several orders of magnitude. This can result in a grid equation system that is very stiff and, hence, difficult to solve numerically and, in fact, has historically limited its application. In addition, important information can be lost as derivatives in regions of large vorticity swamp important derivatives in regions of lower vorticity, much as the 'convective' terms of a transport equation can swamp out important diffusion terms at higher Reynolds number. The newly derived weight functions overcome these difficulties by an appropriate normalization procedure, resulting in well behaved grid equations as well as adaption in lower vorticity regions that demand fine-mesh resolution for accurate numerical simulation.

The weight functions have been developed using a component-by-component approach. Each component has been designed to increase grid clustering in regions where a certain flow situation occurs. The component-by-component approach also facilitates the inclusion of additional terms, if the need arises in future studies. The weight functions formulated are as follows:

$$\begin{aligned} w^k_{i,j} \;=\; 1.0 &+ a^k \frac{|\omega_{i,j}|}{|\omega_{i,j}|_{\max}} + b^k \frac{\left|\dfrac{(\omega_{\xi^k})_{i,j}}{\omega_{i,j}}\right|}{\left|\dfrac{(\omega_{\xi^k})_{i,j}}{\omega_{i,j}}\right|_{\max}} \\ &+ c^k \frac{\left|\dfrac{(\omega_{\xi^k\xi^k})_{i,j}}{\omega_{i,j}}\right|}{\left|\dfrac{(\omega_{\xi^k\xi^k})_{i,j}}{\omega_{i,j}}\right|_{\max}}, \qquad k = 1,2. \end{aligned} \tag{C.11}$$

The first term is the constant 1.0 and is employed to ensure that the weight function is always non-zero positive. A zero weight function would imply infinite grid spacing. If the weight function were to become negative, equidistribution would require a negative volume of the computational cell. The second term is the normalized magnitude of the vorticity and results in grid clustering in regions of large vorticity, or large velocity gradients. This term does not account for resolution needed in regions of large vorticity gradient or slope but small vorticity magnitude. Such a region can be a source of significant truncation error. In fact, this is often the case in unsteady or higher Reynolds number flows.

The second term is the normalized relative derivative of the vorticity with respect to the coordinate ξ^k. The contribution of this term is from regions of large vorticity gradients that need resolution, such as those adjoining high-vorticity regions..

The third term is the normalized relative second-order derivative of vorticity with respect to the coordinate ξ^k. The use of this term is an attempt to resolve regions of large vorticity curvature near the periphery of large vorticity-gradient regions. The use of the relative derivative is important to eliminate domination by large vorticity gradients present in high-vorticity regions. Thus, the relative derivative is a better measure of the local truncation error than the absolute derivative.

Evaluation of Weight Function Coefficients

The weight functions are determined by the vorticity distribution as well as by the coefficients a^k, b^k, and c^k, in Eq. (C.11). A wide range of values for these coefficients has been tested. The choice of values has been based primarily on numerical experimentation. In general, a fairly wide range of values for these parameters yields acceptable results.

The contribution of each weight-function component is determined by its coefficients. A 10 percent contribution from the magnitude of the vorticity, 50 percent from the relative first-derivative and 40 percent from the relative second-derivative of vorticity has been found to provide the best resolution for the flows studied. This distribution determines the relative magnitude of a^1, a^2, b^1, b^2, c^1, and c^2. Theoretically, the ratio of the minimum value of the weight function to its maximum value is equal to the ratio of maximum cell volume to minimum cell volume. The present method is approximately equidistributional and, as such, this relation is not exact. However, estimates of the maximum and minimum values of the weight functions can be used to predict the ratio of maximum to minimum cell volume. Hence, a limit may be placed on the maximum allowable cell size variation. The present work uses a value of 200, so that

$$\frac{(W^i)_{\min}}{(W^i)_{\max}} = \frac{(\Delta x^i)_{\max}}{(\Delta x^i)_{\min}} \approx 200. \tag{C.12}$$

The massive grid migration necessary to maintain this theoretically optimum grid distribution in the streamwise direction requires a time step much smaller than is needed to resolve the temporal scales of the physical problem. This is not efficient. A trade-off exists between larger values and greater adaption, versus overall efficiency. Stronger adaption produces greater grid-point migration, resulting in slower convergence of the stream-function equation, as the initial guess is then further away from the true solution. A reduction in time step may also be required for very large grid movement. Thus, with the present adaptive method, and likely with others, the smallest possible number of grid points may not necessarily lead to the greatest efficiency. For flows with widely spaced and rapidly moving flow structures requiring resolution, such as a vortex-ring convecting downstream, it is more efficient to use a few additional grid points and moderate adaption. Thus, the parameters should be chosen such that the time step limitation is imposed by the time scales of the flow, and not by the degree of grid movement. These comments apply primarily to the streamwise direction, where the large extent of the domain permits grid points to travel large distances. The confined nature of the geometry in the normal direction, combined with the spatially elliptic equations governing grid movement, tends to moderate movement in the normal direction.

Hence, for the current work, the coefficients are scaled by a factor of 1000 in the streamwise direction. The values employed for the weight function coefficients are $a^1 = 20$, $b^1 = 100$, $c^1 = 80$, $a^2 = .02$, $b^2 = .1$ and $c^2 = .08$. For the family of geometries studied, simulations indicate that the values of these coefficients can be held constant, independent of Re, $\Delta\tau$ or streamwise extent of physical domain.

The most important coefficient in the expression for the weight function is that of the first-derivative. The contribution of the vorticity magnitude term is primarily in regions of large flow acceleration and/or shear, such as near the throat. The importance of this term decreases as the unsteadiness of the flow increases. The first-derivative term, in conjunction with the magnitude, has been sufficient to resolve all but the most severe cases. For the latter, additional resolution was required in regions of large vorticity curvature. Therefore, the second-order derivative term was implemented to successfully resolve these regions. This is particularly important for the near-wall region, where resolution is important but both magnitude and first derivatives of the solution flow variables may be moderate. Also, this term was found to be crucial for appropriate resolution of the region of low-speed flow along the wall and upstream of the constriction and, to avoid contamination of the flow downstream of this region.

2.C.5 Model Internal Flow Problem

The geometry of the test problem chosen was a family of axisymmetric constrictions described by a cosine function, and is illustrated schematically in Fig. C.2. For this geometry, experimental data is available for the Reynolds number range 500-15,000 and for constrictions of 25-75 percent by area (Ahmed and Giddens [1983] and Deshpande and Giddens [1980]). The asymptotic state of the flow is steady or unsteady, depending upon the severity of the constriction and the value of the Reynolds number.

Numerical Solution

Equations (C.5), (C.7) and (C.8) are written in computational coordinates. The implied transformation maps the general region of interest R in the physical (x,r) plane, to the unit square $\Box$ in the computational plane defined as $\Box \blacktriangle [(\xi,\eta) \mid 0 \leq \xi \leq 1, 0 \leq \eta \leq 1]$. A uniformly spaced finite difference grid Δ of size (N x M) is employed to discretize the unit computational region $\Box$.

The three coupled equations, two for the grid and one for the vorticity, are integrated in time. The grid equations share some of the 'stiffness' of the flow transport equations through the velocity-like forcing functions P and Q. In fact, the transformation may be viewed as transferring the difficulty usually encountered in solving the flow equations, to that now experienced in solving the grid equations. The 'stiffness' of the flow equations is reduced through the scaling of the transformation metrics appearing in their coefficients. The equations are discretized and solved numerically. Time derivatives are approximated using a first-order accurate backward difference. The discretized non-linear terms are quasi-linearized. Extrapolation in time is employed to generate an initial guess for the iterative solution of the stream function. In addition, a local iteration procedure is employed to update the coefficients of the 'convective' terms in the vorticity-transport equation. For further details of the procedure, see Thornburg (1991). The location and spacing of the mesh points, not the accuracy with which the grid equations are evaluated, affects the accuracy and stability of the discretized flow equations. Therefore, in order to produce a numerically stable solution to the grid equations, the idea of upwind differencing is used in these equations. Upwind differencing of the flow equations adversely affects the accuracy of the flow solution through the introduction of numerical diffusion, which lowers the local effective Reynolds number. However, this very property is beneficial for the grid equations. It is desirable for the grid to vary smoothly near regions of large gradients where grid clustering occurs. Thus, the numerical diffusion introduced by first-order upwind differencing of the grid equations not only adds to the stability of the grid-transport process, but actually improves the grid quality, and, hence, the flow simulation accuracy. The biased differencing is based on the velocity-like P and Q forcing functions.

The source terms of the discretized equations require the values of P and Q at discrete locations, and must also be evaluated from discrete weight function data. The weight functions contain values of the vorticity field at time level (n+1) and represent the dynamic coupling between the grid and the flow solution. The simplest technique to decouple the equations would be to lag the vorticity appearing in the grid forcing functions. This approach was implemented and found to be less than optimal. A very small time step was needed to adequately track the temporally evolving flow even for moderate Reynolds number cases. Another contribution of the present work lies in addressing this shortcoming, by using temporal extrapolation to obtain a guessed value for vorticity ω^{n+1}, as:

$$\omega_{i,j}^{n+1} = 2\omega_{i,j}^{n} - \omega_{i,j}^{n-1} + O(\Delta\tau)^2. \qquad \text{(C.13)}$$

These extrapolated values for the vorticity are used to evaluate the forcing functions.

High-Reynolds number flows often exhibit localized regions of intense variation of vorticity. Hence, the variation of the weight function can become severe and localized in this region, resulting in rapid localized variation in grid spacing. The interval of influence of these localized regions is increased by smoothing the forcing functions, resulting in smoother variation of mesh size.

In order to control the truncation error associated with the grid speed terms, as well as provide stability for the grid evolution, it is necessary to control the magnitude of grid movement. The unsteady nature of the present flow at higher Re produces vortical structures which convect out of a finite solution domain. This can cause excessive and unnecessary grid movement at the outlet, because as a structure leaves the solution domain, its associated grid points rapidly migrate to the next structure upstream. In practice, it was found beneficial to create a buffer region at the outlet for the grid solution. The buffer region is created by exponentially damping the forcing functions to zero over the last 25 points of the domain in the streamwise direction. The buffer region is used to eliminate the rapid grid movement in this region of relatively quiescent flow, thus removing the time step constraint imposed by this movement.

Overhead Associated with Adaption

For the unsteady flow cases examined, the adaption procedure is enabled throughout the simulation. By monitoring the residence time of each subroutine associated with the adaption, the direct overhead is found to be of the order of 15-30 percent for the unsteady cases studied. The overhead for steady-flow cases is much less, as the adaption procedure is active for only a small fraction of the total simulation time. The iterative method employed for the steady problems studied exhibits rapid convergence initially. The grid-transport equations do not represent physical laws, and hence, the level of convergence required for acceptable accuracy is much less than that for the flow-transport equations. For steady-flow or even quasi-steady flow, no further accuracy is achieved in the flow solution by adaption after the general flow structure has developed and the grid adapted to it. Hence, for steady-flow calculations, the grid movement is stopped before a fully converged flow solution has been achieved. For a steady problem where the initial transients are not of interest, it seems wasteful to spend resources to adapt and resolve these transients. Therefore, the most efficient procedure for steady-flow problems has been found to consist of starting the calculation with some initial static grid and running the simulation until the gross structure has developed. Then the adaption procedure is activated for approximately 50-100 iterations, and deactivated thereafter as grid movement becomes small. This is also a sufficient number of time integrations for the adaption procedure to sense and automatically resolve flow structures appearing due to the increased resolution provided by the adapting grid in certain regions. The simulation is then continued, using the static but adapted grid, to the desired level of convergence for the flow solution. This approach greatly reduces the overhead of the adaptive procedure for steady-flow problems.

Resolution of Scales

The resolution of the length and time scales prevailing in a flow is the most important factor for an accurate simulation. Time-accurate simulations of unsteady flow, such as those performed in the present work, must employ a spatially constant time step. For the flows studied, it is believed that the reduction in the required number of grid points due to adaption is greatest in the streamwise direction, where the reduction has been as much as 50 percent. The reduction of points in the normal direction is not as dramatic. The regions of intense flow gradients requiring normal resolution travel over a shorter distance and their locations are easily predicted. For example, the oscillating shear layer, which requires the greatest normal resolution, is confined to a location only several times its thickness. In addition, the wall region always requires normal resolution. Using this a priori information, an initial grid with a fairly efficient normal grid-point distribution can be constructed, lessening the need for an adaptive procedure in this coordinate direction. Thus, the reduction in the number of grid points required in the normal direction is estimated to be 20-30 percent, as compared with a static clustered grid, depending on the particular case.

Proper resolution of the time scales was a much more difficult problem than anticipated. The time scales of the flows in the more severe geometries were very short. For the configurations studied, the severity of the flow was primarily due to the geometric configuration. The most important consideration being the area constriction ratio (ACR), followed by the half-length (XSL), over which the constriction occurred. Plots of the truncation error associated with the time derivative, based on static grid cases, showed that the shear layer immediately downstream of the obstruction exhibited the largest of these truncation errors and the shortest time scale.

It is not straightforward to analyze the truncation errors associated with time derivatives for moving- grid simulations and, hence, to determine if the $\Delta\tau$ used provides sufficient temporal resolution for the method employed. The most reasonable method for determining temporal resolution consists of carrying out several simulations with various time steps, constant for a given simulation. Time-step independence suggests sufficient temporal resolution. For ACR = 0.75 with XSL = 2.0, the flow with Re = 2000 has been analyzed extensively. This case was chosen for study due to the fact that much experimental data was available for it. A simulation using first-order accurate time discretization was performed, and progressively smaller time steps were employed until successive calculations showed no qualitative variation. Time step independence was observed for $\Delta\tau < 0.001$. In addition, a simulation using second-order accurate time differencing was also performed for this case. No qualitative difference was observed between the two sets of results. It is therefore believed that the first-order accurate temporal discretization with a time step of 0.001 provides adequate temporal resolution for this flow situation. This procedure is similar to varying grid sizes to evaluate grid independence and, hence, spatial resolution. For less severe geometries such as the one with ARC= 0.50, XSL = 2.0 and Re = 2000, the time scales are much less severe. For this case, no qualitative differences were observed in the results using either first-order accurate or second-order accurate temporal discretization, so long as the time step employed was smaller than 0.002. However, small scale differences were observed under quantitative analysis.

2.C.6 Simulation Results and Discussion

Results are presented for various constriction ratios and Reynolds numbers. The severity of the geometry triggers separation at very low Reynolds number. For example, for the configuration with ACR = 0.75 and XSL = 1.0, separation occurs at a Reynolds number of 10 (Lee and Fung [1970]). The flows simulated are grouped in two categories. The first category deals with steady flows, while the second deals with unsteady flows. The category to which a given flow belongs depends on the values of the three parameters, namely, area constriction ratio (ACR), physical half-length (XSL) of constriction and Reynolds number (Re).

Steady-Flow Results

A series of calculations were performed in order to validate solutions on non-uniform, non-orthogonal grids and to demonstrate grid independence. The geometrical configuration with ACR = 0.50, XSL = 2.0 and Re = 500 was chosen, due to the availability of experimental data for it. The first result presented is a simulation with a large (450 x 45), essentially uniform, orthogonal grid, and was undertaken to obtain a benchmark set of data. The grid as well as the vorticity and stream-function contours are presented in Fig. C.3. It can be observed that the grid used for the calculation is quite fine and should provide adequate spatial resolution. The grid is generated using a Laplacian generation system, with orthogonality enforced on the boundaries. A second simulation was performed with identical parameters, but with the inlet and the outlet locations placed 50 percent further upstream and downstream ($-7.5 < x < 15.0$ vs. $-5 < x < 10$), respectively, and the grid increased to (675 x 45), to maintain the same grid spacing as for the shorter configuration. For subsonic flows, such as those studied in the present work, the importance of the placement of inflow/outflow boundaries is well known. However, as no visual difference is observed in the results of these two calculations, it can be concluded that the solution domain of the shorter configuration is sufficiently long. Next, simulation results were obtained for the case of a (300 x 30) initial grid and are shown in Fig. C.4. Comparing these results with the finer-grid results shown in Fig C.3, it can be observed that the separation streamline is not as smooth for the coarser (300 x 30) grid as for the (450 x 45) grid case. Further, it is noted that the reattachment point is not as far downstream, nor is it as sharply defined as for the fine grid case. Hence, grid adaption was then activated and the simulation continued in time. Figure C.5 clearly shows the grid adaption, as well as the smoothness of the separating streamline and the regaining of the separation bubble length.

Two simulations with fewer grid-points were also performed in order to test the procedure for yet coarser grids. Figures C.6 and C.8 present results for (100 x 20) and (50 x 15) fixed grids, respectively. The results were difficult to obtain; very small convergence tolerances were required for the stream-function equation throughout the calculation. Stalled convergence, with oscillatory behavior of vorticity residuals, was often encountered, necessitating an adjustment of the time step and a restart of the calculation. Then, for both of these grids, the adaption procedure was activated for 100 time steps and the simulation advanced to steady state. The results obtained using the adaptive technique are presented in Figs. C.7 and C.9 for (100 x 20) and (50 x 15) adapted grids, respectively. In both instances, the convergence behavior was improved, with the adapted grid eliminating the need for user intervention. The accuracy of the simulation improved markedly with the adaption. Separation and reattachment points became more sharply defined and the separation streamline became more smooth. The vorticity contours show no visible difference for these calculations, and hence, are not repeated for each grid size. The axial distribution of vorticity is presented for two grid sizes, namely, (300 x 30) and (50 x 15) in Fig. C.10. The variation due to grid size is greatest in the vicinity of the separation point. The length of the separation bubble gradually decreases as the number of grid points is decreased, reflecting the decreased resolution. The (100 x 20) grid size provides satisfactory results; the contour plots presented differ only slightly from the larger (300 x 30) adapted-grid results, in the region immediately surrounding the reattachment point. The (50 x 15) grid size is believed to provide insufficient resolution even with the adaption, as the separation streamline is non-smooth. However, the adapted grid is believed to provide near optimal resolution for the available number of grid points.

The same geometric configuration was also studied with a flow Reynolds number of 1000. Simulations for two grid sizes, namely, (300 x 30) and (100 x 20) were performed and the results are presented in Figs. C.11 and C.12, respectively. The two sets of results agree well with each other, demonstrating that the adapted (100 x 20) grid is adequate for this flow. The calculated velocity profiles at various streamwise locations are compared with the experimental data of Ahmed and Giddens (1983) in Fig. C.13. The agreement is close. For this flow situation, the flow is indeed axisymmetric. It can be observed that for the steady-state flow results presented in Figs. C.1-C.12, the reattachment point is one of the most sensitive quantities with respect to grid size and grid-point distribution. Table 1 summarizes the reattachment lengths calculated and compares the results with experimental data for various configurations. The sensitive quantity of reattachment length clearly benefits from the increased resolution capability of the adaptive procedure. It is observed that the relationship between flow Reynolds number and reattachment length for this range of Reynolds number is linear, as theoretically predicted (Smith [1977]).

In summary, results for steady flow have been demonstrated to be grid independent. Various geometrical configurations with ACR varying from 0.2 to 0.89 and XSL = 1.0, 2.0 and 4.0 were studied; none maintained attached flow for Reynolds number greater than 200. The grid-adaption procedure has also been shown to re-distribute grid points, such that relatively coarse grids provide results comparable to those with much finer non-adapted grids. Typically, the calculations required 400-600 iterations for convergence of the vorticity to residuals less than 1×10^{-10}. In addition, the grid adaption is activated for only 100 of these iterations. Hence, the overhead for these calculations is less than 10 percent. Further, the numerical simulation has nearly reproduced the available measured velocity profiles.

Unsteady Flow Results

Simulation results are presented for two different flow Reynolds numbers for a geometric configuration with XSL = 2 and ACR = 0.75 employing a (600 x 85) grid. These configurations exhibit inherently unsteady flow. For Re = 2000, Figs. C.14a-g present the grid, vorticity and instantaneous stream-function contours for various instants of time in the region of the obstruction, while Figs. C.15a-g present the same data corresponding to the region immediately downstream of this location. The non-uniform adapted grid is obvious in the sequence of these figures. The adaption is most apparent in the normal direction, with the largest clustering occurring near the shear layer, as expected. The clustering in the normal direction gradually decreases with distance downstream, as the fluid mechanics processes distribute the vorticity more uniformly in the normal direction. The clustering near the wall to resolve the boundary layer is quite pronounced.

Grid clustering in the streamwise direction is less obvious, but analysis of the results simulated using various values for the weight function coefficients, and hence, various grid distributions, has indicated that the distribution attained is appropriate. The clustering is clearly visible in the rapidly accelerating and turning region near the throat. Following this region, the streamwise distribution of the grid is nearly uniform, up to approximately $x = 5$, as vortical structures appear throughout this region. In the region $5 < x < 8$, the streamwise distribution is less constant with time, as pairing of vortical structures often occurs in this region. The distribution varies from nearly uniform when several structures are present, to a more clustered distribution when these structures have combined to form one larger structure. For $x > 8$, the streamwise distribution is much less uniform, as discrete vortical structures have developed with regions of relatively smooth vorticity between them. The difference between this region and the region immediately upstream is that the former region always contains discrete structures and, hence, a non-uniform grid.

Figure C.16 presents the flow results for the region near the outlet. It is observed that, for flow at the relatively low Re of 2000, viscous diffusion has smoothed the gradients of the vortical structures as they convect downstream. The reduced vortical intensity of the flow is reflected in the streamwise sparsity of the grid in the downstream region.

Simulations were also performed for Re = 10,000. However, the time step required for temporal resolution was such that tracking the flow for any meaningful intervals of time was computationally very expensive. Figure C.17 shows the flow results for the region near the outlet. For Re = 10,000, the flow structures convect quickly downstream, and hence, maintain their intensity for a greater streamwise distance. This is reflected in the finer spacing of the grid in the downstream region. It should be noted that the results presented for this configuration with Re = 10,000 are not completely resolved in time, particularly in the region near the shear layer. In addition, it is believed that the axisymmetric assumption is no longer appropriate at this Reynolds number. Currently, work is being undertaken in order to successfully simulate these higher Reynolds number flows.

2.C.7 Conclusion

An automated flow-adaptive grid procedure for efficient use of grid points to resolve temporally varying regions of high vorticity and high vorticity gradients and curvature has been developed. The technique is based on the well known elliptic grid-generation procedures and advances the grid in time along with the flow solution, as the current grid equations are parabolic in nature. Therefore, the present technique has the advantage of being computationally more efficient than a purely elliptic-equation-based technique. In fact, the grid-transport equations fit well into unsteady viscous flow solution procedures. The procedure uses the most recent flow information to adapt the grid, not information from previous time levels, and does not require interpolation. The relatively small overhead associated with grid migration in the present method makes the technique computationally practical for truly unsteady flow problems. The relative derivative contribution to the weight function prevents regions of large vorticity magnitude from swamping regions of lower vorticity which may also require resolution. This is necessary in order to resolve structures downstream of the obstruction, where viscous diffusion has diminished the gradients appearing in these structures. Finally, many of the existing codes employing elliptic grid-generation systems may be modified to include the current adaptive grid technique. The equations combine some of the most desirable features of several types of grid generators, without added complexity or computational expense. They exhibit the efficiency and flow-tracking capability of parabolic equations, while maintaining the smoothness of computationally expensive elliptic equations.

The use of the full unsteady equations combined with the moving grid capability make the code very versatile, allowing the straightforward implementation of procedures to handle pulsatile flow and/or deforming boundaries. These capabilities are essential in studies of flow-structure interactions as well as passive and active flow control. The capabilities developed here are also of interest to the biomechanics community for the study of flow through flexible configurations.

Section 3

REFERENCES

Note: Superscript (*) designates work supported, in part, by AFSOR Grant 90-0249.

[A.1] Carr, L.W., (1985), "Dynamic Stall: Progress in Analysis and Prediction," *AIAA Paper No. 85-1769.*

[A.2] Carr, L.W., (1990), Editor: "Physics of Forced Unstedy Separation," *Proc. of NASA/AFOSR/ARO Workshop*, Moffett Field, California, April, pp. 17-19.

[A.3] Chyu, W.J., Davis, S.S. and Chang, K.S., (1981), "Calculation of Unsteady Transonic Flow Over an Airfoil," *AIAA Journal*, Vol. 19, No. 6, pp. 684-690.

[A.4] Davis, R.T., (1979), "Methods for Coordinate Generation and Potential Flow Solution Based on Schwarz-Christoffel Transformations," *AIAA CP 799*, pp. 180-194.

[A.5] Douglas, J. and Gunn, J.E., (1964), "A General Formulation of Alternating Direction Methods, Part I. Parabolic and Hyperbolic Problems," *Numerische Mathematik*, Vol. 6, pp. 428-453.

[A.6] Fant, D.B., and Rockwell, D., (1992), Editors: *Proceedings of Workshop on Supermaneuverability: Physics of Unsteady Separated Flow at High Angle-of-Attack*, Lehigh University, Bethlehem, Pennsylvania, April.

[A.7] Gatski, T.B., (1991), "Review of Incompressible Fluid Flow Computations Using the Vorticity-Velocity Formulation," *Applied Numerical Mathematics*, Vol. 7, pp. 227-239.

[A.8] Gresho, P.M., (1991), "Incompressible Fluid Dynamics: Some Fundamental Formulation Issues," *Annu. Rev. Fluid Mech.*, Vol. 23, pp. 412-453.

*[A.9] Ghia, K.N., (1992), "Analysis of Two-Dimensional Flow Structures of Forced Unsteady Separated Flows," see Fant and Rockwell, (1992), pp. 157-173.

[A.10] Ghia, K.N., Hankey, W.L. and Hodge, J.K. (1977), "Study of Incompressible Navier-Stokes Equations in Primitive Variables Using Implicit Numerical Techniques," *AIAA Paper No. 77-0648*; also AIAA Journal, Vol. 17, pp. 298-301.

*[A.11] Ghia, K.N., Ghia, U. and Osswald, G.A., (1990), "Characterization of Dynamic Stall Phenomenon Using Two-Dimensional Unsteady Navier-Stokes Equations," *Proc. NASA/AFOSR/ARO Workshop on Physics of Forced Unsteady Separation*, Moffett Field, CA, April; also NASA CP 3144, Edited by L. W. Carr, 1992, pp.129-147.

*[A.12] Ghia, K.N., Yang, J., Osswald, G.A. and Ghia, U., (1991), "Study of the Dynamic Stall Mechanism Using Simulation of Two-Dimensional Navier- Stokes Equations," *AIAA Paper No. 91-0546*, also see "Physics of Forced Unsteady Flow for a NACA 0015 Airfoil Undergoing Constant Pitch- Up Motion," Journal of Fluid Dynamic Research, 1992.

*[A.13] Ghia, K.N., Yang, J., Ghia, U., and Osswald, G.A. (1992), "Analysis of Dynamic Stall Phenomenon Through Simulation of Force Oscillatory Flows," *Proc. of 5th Symp. on Numerical and Physical Aspects of Aerodynamics*, Long Beach, CA, January.

*[A.14] Ghia, K.N., Yang, J., Osswald, G.A. and Ghia, U., (1992), "Study of the Role of Unsteady Separation in the Formation of Dynamic Stall Vortex," *AIAA Paper No. 92-0196.*

[A.15] Ghia, U. and Ghia, K.N., (1987), "Navier-Stokes Equations for Incompressible Flow," section of Chapter in *Handbook of Fluids and Fluid Machinery*, Editor: A. Fuchs, McGraw Hill.

[A.16] Gustafson, K. and Wyss, W., (1990), Editors: *Proceedings of IMACS 1st International Conference on Computational Physics*, University of Colorado at Boulder, Boulder, Colorado, June, pp. 11-15.

[A.17] Helin, H.E., (1989), "The Relevance of Unsteady Aerodynamics for Highly Maneuverable and Agile Aircraft," *Proc. of 4th Symposium on Numerical and Physical Aspects*, Long Beach, CA, January.

*[A.18] Huang, Y., Ghia, U. and Ghia, K.N., (1992), "Development of a 3-D Unsteady Navier-Stokes Analysis for Submarine Afterbody Flows," *Aerospace Engineering Report*, AFL 92-8-77; University of Cincinnati, Cincinnati, Ohio.

[A.19] Lang, J.D. and Francis, M.S., (1985), "Unsteady Aerodynamics and Dynamic Aircraft Maneuverability," *AGARD Symposium on Unsteady Aerodynamics-Fundamentals and Applications to Aircraft Dynamics*, AGARD, Gottingen, Germany, May.

[A.20] Lerner, P., (1991), "Stall Tactics, The X-31 is Teaching Old Dogfighters New Tricks," *Air And Space*, April-May, pp. 29-37.

[A.21] Matlda, Y., Kuwahara, K. and Takami, H., (1975), "Numerical study of Steady Two-Dimensional Flow Past a Square Cylinder in a Channel," *Journal of the Physical Society of Japan*, Vol. 38, No. 5, May 1975.

[A.22] McAllister, K.W. and Carr, L.W., (1979), "Water Tunnel Visualizations of Dynamic Stall," *Journal of Fluids Engineering*, Vol. 101, pp. 376- 380.

[A.23] Mehta, U.B., (1977), "Dynamic Stall of an Oscillating Airfoil," *AGARD CP* 227, Paper No. 23, pp. 1-32.

[A.24] Osswald, G.A., (1981), "Analysis and Numerical Solutions of Unsteady Two-Dimensional Navier-Stokes Equations in Primitive and Derived variables," *Master's Thesis*, University of Cincinnati.

[A.25] Osswald, G.A., Ghia, K.N. and Ghia, U., (1987), "A Direct Algorithm for Solution of Incompressible Three-Dimensional Unsteady Navier-Stokes Equations," *AIAA CP 874*, pp. 408-421.

[A.26] Osswald, G.A., Ghia, K.N. and Ghia, U., (1988), "Direct Solution Methodologies for the Unsteady Dynamics of an Incompressible Fluid," *Computational Mechanics '88*, Vol. 2, Editors: S.N. Atluri and G. Yagawa, Springer-Verlag, pp. 5351-5354, April.

[A.27] Osswald, G.A., Ghia, K.N. and Ghia, U., (1989), "Analysis of Potential and Viscous Flows Past Arbitrary Two-Dimensional Bodies with sharp Trailing Edges," *AIAA CP 895*, pp. 668-677.

*[A.28] Osswald, G.A., Ghia, K.N. and Ghia, U., (1990), "Simulation of Dynamic Stall Phenomenon Using Unsteady Navier-Stokes Equations," *Proc. of IMACS 1st International Conf.*, Boulder, CO, pp. 252-261, June; also, Computer Physics Communications, Vol. 65, pp. 209-218.

*[A.29] Osswald, G.A., Ghia, K.N. and Ghia, U., (1992), "A Direct Implicit Methodology for the Solution of the Rapid Pitch-Up of an Airfoil with and without Leading Edge Flow Control," *Proc. of 13th Int. Conf. on Numerical Meth.*, Rome, Italy, July.

*[A.30] Osswald, G.A., (1992), "Some Critical Issues Associated with the Physics of Unsteady Flows During Maneuvers to High Angles of Attack," see Fant and Rockwell, (1992), pp. 223-224.

[A.31] Salari, K. and Roache, P.J., (1990), "The Influence of Sweep on Dynamic Stall Produced by a Rapidly Pitching Wing," *AIAA Paper 90-0581.*

*[A.32] Rohling, T.C., (1991), "Simulation of Chaotic Flow Past Airfoils at High Incidence Using the Unsteady Navier-Stokes Equations," *Master's Thesis*, University of Cincinnati.

[A.33] Sankar, N.L and Tassa, Y., (1980), "Reynolds Number and Compressibility Effects on Dynamic Stall of a NACA 0012 Airfoil," *AIAA Paper No. 80- 0010.*

[A.34] Speziale, C.G., (1987), "On the Advantages of Vorticity-Velocity Formulation of the Equations of Fluid Dynamics," *J. Comput. Phys.*, Vol. 73, pp. 476-480.

[A.35] Visbal, M.R. and Shang, J.S., (1989), "Investigation of the Flow Structure Around a Rapidly Pitching Airfoil," *AIAA Journal*, Vol. 27, No. 8, pp. 1044-1055; also *Proc. of AFOSR/FJSRL/DRAM/UC Workshop II on Unsteady Separted Flows*, FJSRL-TR-88-084, pp. 91-108.

[A.36] Visbal, M.R., (1990), "On Some Physical Aspects of Airfoil Dynamic Stall," *Proc. of Int. Symp. on Nonsteady Fluid Dynamics*, Editor: Miller, J.A. and Telionis, D.P., June 1990, Toronto, Ontario, Canada, pp. 127-147.

[A.37] Walker, J.D.A., (1992), "Unsteady Boundary-Layer Separation in Two-Dimensional Flows," see Fant and Rockwell, (1992), pp. 131-156.

[A.38] Walker, J.M., Helin, H.E. and Strickland, J.H., (1985), "An Experimental Investigation of an Airfoil Undergoing Large Amplitude Pitching Motions," *AIAA Journal*, Vol. 23, No. 8, pp. 1141-1142, August; also, AIAA Paper NO. 85-0039.

[A.39] Werlé, H., (1976), "Visualization Hydrodynamique de L'écoulement Autour d'une Pale Oscillante," *ONERA Rapport Technique* No. 56/1369 AN, January.

[A.40] Yang, J., (1992), "Study of Dynamic Stall Phenomenon and Its Control Using Vorticity, Stream Function and Circulation Form of the Unsteady Navier-Stokes Equations," *Doctoral Disseration under preparation*, University of Cincinnati, Cincinnati, Ohio.

[B.1] Brandt, A., (1984), "A Guide to Multi-grid Development," *GMD Studien Nr. 85, GMD-AIW, Postfach 1240, D-5205,* St. Augustin 1, W.Germany.

[B.2] Brandt, A., (1979), "Multi-Level Adaptive Computations in Fluid Dynamics," *AIAA No. 79-1455, AIAA 4th Comp. Fluid Dynamics Conf.*, Williamsburg, Virginia, July.

[B.3] Brandt, A. and Dinar, N., (1979), "Multigrid Solutions to Elliptic Flow Problems," *Num. Methods Partial Differential Eqs.* (S. Parter, ed.), Academic Press pp. 53-147.

[B.4] de Brederoede, V. and Bradshaw, P., (1972), "Three-Dimensional Flow in Norminally Two-Dimensional Separation Bubbles: Part I. Flow Behind a Rearward Facing Step," *Imperial College Aero Report 72-19*, Aug.

[B.5] Dick, E., (1988), "A Multi-Grid Method for Steady Incompressible Navier-Stokes Equations Based on Flux-Difference Splitting," *in Multigrid Methods*, Marcel Dekker, Inc.

[B.6] Freitas, C. J., Street, R. L., Findikakis, A. N. and Koseff, J. R., (1985), "Numerical Simulation of Three-Dimensional Flow in a Cavity," *Int. J. Num. Methods Fluids*, Vol. 5, pp. 561-575.

[B.7] Ghia, U., Ghia, K. N. and Shin, C. T., (1982), "High-Re Solutions for Incompressible Flow Using the Navier-Stokes Equations and a Multigrid Method," *J. Comp. Physics*, V. 48, No. 3, pp. 387-411.

[B.8] Hackbusch, W., (1985), *Multigrid Methods and Applications*, Springer-Verlag.

[B.9] Hackbusch, W. and Trottenberg, U., (eds), (1982), *Multigrid Methods*, Springer-Verlag.

[B.10] Hackbusch, W. and Trottenberg, U., (eds.), (1987), *Multigrid Methods*, Springer-Verlag.

[B.11] Hafez, M. and Soliman, M., (1989), "A Velocity Decomposition Method for Viscous Incompressible Flow Calculations, Part II," *AIAA No. 89-1966-CP.*

*[B.12] Huang, Y. and Ghia, U., (1991), "A Multigrid Method for Solution of Vorticity-Velocity Form of 3-D Navier-Stokes Equations," *Proc. Fifth Copper Mtn. Conf. Multigrid Techniques,* Copper Mountain, Colorado, April.

*[B.13] Huang, Y., Ghia, U., Osswald, G. A. and Ghia, K. N., (1991), "Unsteady Three-Dimensional Simulation Using Vorticity-Velocity Form of the Navier-Stokes Equations and ADI+MG+DGS Method," *AIAA No. 91-1562, Proc. AIAA 10th Comp. Fluid Dynamics Conf.*, Honolulu, Hawaii, June.

[B.14] Koseff, J. R., Rhee, H. S. and Street, R. L., (1983), *private communication.*

[B.15] Koseff, J. R. and Street, R. L., (1984), "Visualization Studies of Shear Driven Three-Dimensional Recirculating Flow," *J. Fluids Engr.*, V.106, pp. 21-29, March.

[B.16] Mochizuki, O., Kiya, M., Ono, T. and Tsukasaki, T., (1990), "Three-Dimensional Vortical Structure in Lid-Driven Square Cavity Flows," *J. JSME, B*, 56:524, No. 89-1034 A, April.

[B.17] McCormick, S. F., (ed.) (1988), *Multigrid Methods*, Marcel Dekker, Inc.

[B.18] Osswald, G. A., Ghia, K. N. and Ghia, U., (1987), "Direct Algorithm for Solution of Three-Dimensional Unsteady Navier-Stokes Equations," *AIAA No. 87-1139, AIAA 8th Comp. Fluid Dynamics Conf.*, Honolulu, Hawaii, June.

[B.19] Osswald, G. A., Ghia, K. N. and Ghia, U., (1988), "Direct Method for Solution of Three-Dimensional Unsteady Incompressible Navier-Stokes Equations," *Proc. 11th Int. Conf. Num. Methods Fluid Dynamics,* Williamsburg, Virginia, July.

[B.20] Prasad, A. K., Perng, C-Y. and Koseff, J. R., (1988), "Some Observations on the Influence of Longitudinal Vortices in a Lid-Driven Cavity Flow," *AIAA Paper 88-3654-CP.*

[B.21] Perng, C-Y. and Street, R. L., (1989), "Three-Dimensional Unsteady Flow Simulations: Alternative Strategies for a Volume-Averaged Calculation," *Int. J. Num. Methods Fluids*, Vol. 9, pp. 341-362.

[B.22] Rosenfeld, M. and Kwak, D. and Vinokur, M., (1991), "A Fractional Step Solution Method for the Unsteady and Incompressible Navier-Stokes Equations in Generalized Coordinate Systems," *Journal of Computational Physics*, Vol. 94, No. 1, pp. 102-137..

[B.23] Vanka, S. P., (1986), "A Calculation Procedure for Three-Dimensional Steady Recirculating Flows Using Multigrid Methods," *Comp. Methods Applied Mech. Engr.*, Vol. 55, pp. 321-338.

[B.24] Vanka, V. P., (1986), "Block-Implicit Multigrid Solution of Navier-Stokes Equations in Primitive Variables," *J. Comp. Physics*, Vol. 65, pp. 138-158.

[C.1] Ahmed, S.A. and Giddens, D.P., (1983), "Velocity Measurements in Steady Flow Through Axisymmetric Stenoses at Moderate Reynolds Numbers," *Journal of Biomechanics*, Vol. 16, No. 7, pp. 505-516.

[C.2] Anderson, D.A., (1987), "Equidistribution Schemes, Poisson Generators, and Adaptive Grids," *Applied Mathematics and Computation*, Vol. 24, pp. 211-227.

[C.3] Bockelie, M.J., (1988), "Adaptive Grid Movement Schemes and the Numerical Simulation of Shock Vortex Interaction," *Ph.D. Thesis*, Columbia University, New York.

[C.4] Brackbill, J.U. and Saltzman, J., (1982), "Adaptive Zoning for Singular Problems in Two Dimensions," *Journal of Computational Physics*, Vol. 46, pp. 342-368.

[C.5] Deshpande, M.D. and Giddens, D.P., (1980), "Turbulence Measurements in a Constricted Tube," *Journal of Fluid Mechanics*, Vol. 97, pp. 65-89.

[C.6] Eiseman, P., (1985), "Grid Generation for Fluid Mechanics Computations," *Annual Review of Fluid Mechanics*, Vol. 17, pp. 487-522.

[C.7] Ghia, K.N., Ghia, U. and Shin, C.T., (1983), "Adaptive Grid Generation for Flows with Local High Gradient Regions," *Advances in Grid Generation*, ASME Publication, New York.

[C.8] Kim, H.J. and Thompson, J.F., (1990), "Three-Dimensional Adaptive Grid Generation on a Composite-Block Grid," *AIAA Journal*, Vol. 28, No. 3, pp. 470-477.

[C.9] Lee, J.S. and Fung, Y.C., (1970), "Flow in Locally Constricted Tubes at Low Reynolds Number," *Journal of Applied Mechanics*, Vol. 37, pp. 9-16.

[C.10] Osswald, G.A., (1983), "A Direct Numerical Method for the Solution of Unsteady Navier-Stokes Equations in Generalized Orthogonal Coordinates," *Ph.D. Thesis*, Dept. of Aerospace Engineering and Engineering Mechanics, University of Cincinnati, Cincinnati, Ohio.

[C.11] Smith, F.T., (1977), "Upstream Interactions in Channel Flows," *Journal of Fluid Mechanics*, Vol. 79, pp. 631-655.

[C.12] Thompson, J.F., (1985), "A Survey of Dynamically-Adaptive Grids in the Numerical Solution of Partial Differential Equations," *Applied Numerical Mathematics*, Vol. 1, pp. 3-27.

[C.13] Thompson, J.F., Warsi, Z.U. and Mastin, C.W., (1985b), *Numerical Grid Generation: Foundations and Applications*, North-Holland, Amsterdam.

[C.14] Thompson, J.F., Thames, F.C. and Mastin, C.W., (1974), "Automatic Numerical Generation of Body-Fitted Curvilinear Coordinate System for Fields Containing any Number of Arbitrary Two-Dimensional Bodies," *Journal of Computational Physics*, Vol. 15, pp. 299-319.

*[C.15] Thornburg, H.J., (1991), "An Adaptive-Grid Technique for Simulation of Complex Unsteady Flows," *Ph.D. Thesis*, Dept. of Mechanical, Industrial and Nuclear Engineering, University of Cincinnati, Cincinnati, Ohio.

[C.16] Trompert, R.A. and Verwer, J.G., (1990), "A Static-Regridding Method for Two-Dimensional Parabolic Partial Differential Equations," *Report NM-R8923, Center for Mathematics and Computer Science*, Amsterdam, The Netherlands.

Section 4

JOURNAL PAPERS PUBLISHED AND IN PREPARATION

Books and Monographs

Ghia, K.N., and Ghia, U., "Computational Fluid Dynamics," section in 1992 Yearbook of Science and Technology, Publisher S.P. Parker, McGraw Hill Inc., NY.

Celik, I., Kobayashi, T., Ghia, K.N., Editors: Advances in Numerical Simulation of Turbulent Flows, FED-Vol. 117, ASME, June 1991.

Journal Articles and Papers

Thornburg, H.J., Ghia, U., Osswald, G.A. and Ghia, K.N., "Efficient Computation of Unsteady Vortical Flow Using Flow-Adaptive Time-Dependent Grids," to appear in Journal of Fluid Dynamics Research, December 1992.

Ghia, K.N., Yang, J., Osswald, G.A. and Ghia, U., "Physics of Forced Unsteady Flow Over a NACA 0015 Airfoil Undergoing Constant Pitch-up Motion," to appear in Journal of Fluid Dynamics Research, December, 1992.

Osswald, G.A., Ghia, K.N. and Ghia, U., "Direct Simulation of Unsteady Two-Dimensional and Axisymmetric Incompressible Internal Flows Using Navier-Stokes Equations," to appear in Transactions of IMACS, December 1992.

Huang, Y., Ghia, U., Osswald, G.A. and Ghia, K., "Velocity-Vorticity Simulation of Unsteady 3-D Viscous Flow Within a Driven Cavity," to appear as Proceedings of GAMM Workshop, June 1992.

Ghia, K.N. and Ghia, U., "Study of Forced Separation and Its Control," Developments in Mechanics, Editors: R.C. Baha and B.F. Armaly, Vol. 16, October 1991, pp. 281-282.

Mittal, M.L. and Ghia, U., "Turbulent Mixing for Coal Combustion," Combustion Fundamentals and Applications, The Combustion Institute, Central States Division, Spring Meeting, pp. 65-71, April 1991.

Huang, Y., Ghia, U., Osswald, G.A. and Ghia, K.N., "Unsteady Three-Dimensional Flow Simulation Using Vorticity-Velocity Form of Navier-Stokes Equations and ADI+MG-DGS Method," AIAA CP 914, pp. 380-392, June 1991.

Bishnoi, P., Ghia, U., and Ghia, K.N., "Prediction of Normal Reynolds Stresses with Nonlinear k-ε Model of Turbulence," Advances in Numerical Simulation of Turbulent Flows, FED Vol. 117, ASME, June 1991.

Ramamurti, R., Ghia, U. and Ghia, K.N., "A Semi-Elliptic Analysis for Two-Dimensional Viscous Flows Through Cascade Configurations," International Journal of Computers and Fluids, Vol. 20, No. 3, 1991, pp. 223-242.

Osswald, G.A., Ghia, K.N. and Ghia, U., "Simulation of Dynamic Stall Phenomenon Using Unsteady Navier-Stokes Equations," Computer Physics Communications, Vol. 65, pp. 209-218, 1991.

Ghia, K.N., Ghia, U. and Osswald, G.A., "Dynamic Stall," insert in Stall Tactics Air and Space Smithsonian, Vol. 6, No. 1, pp. 29-37, April/May 1991.

Huang, Y. and Ghia, U., "A Multi-Grid Method for Solution of Vorticity-Velocity Form of 3-D Navier-Stokes Equations," Proceedings of Fifth Copper Mountain Conference on Multi-Grid Methods, Copper Mountain, Colorado, April 1991; also accepted for publication in Communications in Applied Numerical Methods, SIAM.

Ghia, U. and Osswald, G.A., "Low-Dimensional Modeling and Prediction in Fluid Mechanics," Annual Report of the Health Monitoring Technology Center, University of Cincinnati, Cincinnati, Ohio, January 1991.

Ghia, K.N., Osswald, G.A and Ghia, U., "Chaotic Behavior in High-Incidence Low-Reynolds Number Flows," Chaotic Dynamics in Fluid Mechanics, FED Vol. 70, pp. 183-192, ASME, December 1990.

Ghia, U., Osswald, G.A. and Noll, C., "Low-Dimensional Modeling and Prediction in Fluid Dynamics," Proceedings of Second Annual Conference of Health Monitoring Technology Center, University of Cincinnati, Cincinnati, Ohio, November 1990.

Osswald, G.A., Ghia, K.N. and Ghia, U., "Flow Over Arbitrary Axisymmetric Multi-Body Configurations Using Direct Navier-Stokes Simulations," Lecture Notes in Physics, Vol. 371, pp. 215-218, September 1990.

Osswald, G.A., Ghia, K.N. and Ghia, U., "Direct Simulation of Unsteady Two-Dimensional and Axisymmetric Incompressible Internal Flows Using Navier-Stokes Equations," Proceedings of IMACS 1st International Conference on Computational Physics, University of Colorado at Boulder, Boulder, Colorado, pp. 252-262, June 1990.

Ghia, K.N., Ghia, U. and Osswald, G.A., "Characterization of Dynamic Stall Phenomenon Using Two-Dimensional Unsteady Navier-Stokes Equations," Proceedings of NASA/AFOSR/ARO Workshop on Physics of Forced Unsteady Separation, Moffett Field, California, April 1990.

Reports

Ghia, K.N. and Ghia, U., "Simulation Characterization and Control of Forced Unsteady Viscous Flow Using Navier-Stokes Equations," Aerospace Engineering and Engineering Mechanics Report AFL 91-11-76, University of Cincinnati, Cincinnati, Ohio, November 1991.

Ghia, K.N. and Ghia, U., "Direct-Solution Techniques for Viscous Flows and Their Control," Department of Aerospace Engineering and Engineering Mechanics, Report AFL 91-5-75, University of Cincinnati, Cincinnati, Ohio, May 1991.

Section 5

SCIENTIFIC INTERACTIONS-SEMINARS AND PAPER PRESENTATIONS

Professional Presentations:

Invited Lectures:

Ghia, K.N., Overview Lecture presented at OAI Workshop of Fluid Dynamics and Propulsive Systems Focus Group on Needs Assessment, Sandusky, OH, March 6-7, 1992.

Ghia, K.N., presented at University of Tokyo, Tokyo, Japan, August 30, 1991.

Ghia, U., presented at University of Tokyo, Tokyo, Japan, August 30, 1991.

Ghia, K.N., presented at Aeronautical Development Agency, Bangalore, India, August 16, 1991.

Ghia, U., presented at Aeronautical Development Agency, Bangalore, India, August 16, 1991.

Ghia, K.N., presented at University of Taiwan, Taipei, Taiwan, August 13, 1991.

Ghia, U., presented at University of Taiwan, Taipei, Taiwan, August 13, 1991.

Ghia, K.N., presented at National Chenkung University, Tainan, Taiwan, August 12, 1991.

Ghia, U., presented at National Chenkung University, Tainan, Taiwan, August 12, 1991.

Ghia, K.N., presented at ICASE/NASA Langley Workshop on Transition and Turbulence, Hampton, VA, July 1991.

Ghia, U. and Osswald, G.A., presented at General Electric Company, Evendale, Ohio, March 19, 1991.

Ghia, U., Seminar presented at Department of Aeronautical and Astronautical Engineering, Ohio State University, Columbus, Ohio, March 6, 1991.

Ghia, K.N., presented at NSF Workshop on Advances in Computational Methods for Transport Phenomena, University of Kentucky, Lexington, Kentucky, January 7-9, 1991.

Ghia, K.N.," presented at The Institute of Applied Mathematics and Scientific Computing, Indiana University - Bloomington, Bloomington, Indiana, November 1990.

Invited Papers:

Ghia, K.N., "Analysis of Two-Dimensional Flow Structure of Forced Unsteady Separated Flows," Leadoff talk presented at AFOSR Workshop on Supermaneuverability: Physics of Unsteady Flows Past Lifting Surfaces at High Angle of Attack," Lehigh University, Bethlehem, PA, April 9-10, 1992.

Ghia, U., "," Leadoff talk presented at AFOSR Workshop on Supermaneuverability: Physics of Unsteady Flows Past Lifting Surfaces at High Angle of Attack," Lehigh University, Bethlehem, PA, April 9-10, 1992.

Ghia, K.N., Yang, J., Ghia, U., Osswald, G.A., "Analysis of Dynamic Stall Phenomenon Through Simulation of Forced Oscillatory Flows," presented at Fifth Symposium on Numerical and Physical Aspects of Aerodynamic Flows, California State University, Long Beach, CA, January 13-15, 1992.

Osswald, G.A., Ghia, K.N. and Ghia, U., "Study of Forced Unsteady Separation and Its Control," presented at 22nd Midwestern Mechanics Conference, University of Missouri-Rolla, MO, October 6-9, 1991.

Ghia, K.N. and Rohling, T., "Dynamical Systems Characterization of Unsteady Flow," presented at Fourth International Symposium on CFD, University of California, Davis, Davis, CA, September 1991.

Ghia, U. and Huang, Y., "Evolution and Transport of Streamwise Vorticity in Incompressible Flow," presented at Fourth International Symposium on CFD, University of California, Davis, Davis, CA, September 1991.

Ghia, K.N., Yang, J., Osswald, G.A. and Ghia K.N., "Analysis of Structure of Force Unsteady Separated Flows and Its Correlation to Dynamic Stall Vortex Using Vorticity Dynamics," presented at 4th International Symposium on Supercomputing and Experiments in Fluid Dynamics, Nobeyama, Japan, September 1991.

Ghia, U., Thornburg, H.J. and Ghia, K.N., "A Flow-Adaptive Grid Technique for Simulation of Time-Dependent Vortical Flow," presented at Fourth Nobeyama Workshop on Supercomputing and Experiments in Fluid Dynamics, Nobeyama, Japan, September 3-5, 1991.

Ghia, K.N. and Ghia, U., "Three-Dimensional Unsteady Navier-Stokes Analysis and Some Simplified Analyses for Inlet and Nozzle Flows," presented at OAI Workshop on Inlets and Nozzles, The Ohio Aerospace Institute, Brook Park, Ohio, July 1990.

Ghia, K.N. and Ghia, U., "Direct Numerical Simulation of Dynamic Stall Phenomenon Using Two-Dimensional Unsteady Navier-Stokes Equations," IMACS 1st Annual International Conference on Computational Physics, Boulder, Colorado, June 1990.

Ghia, K.N., "Chaotic Flows in Open System," IMACS 1st Annual International Conference on Computational Physics, Boulder, Colorado, June 1990.

Ghia, U., "Numerical Experiments on Flow Control," IMACS 1st Annual International Conference on Computational Physics, Boulder, Colorado, June 1990.

Ghia, U. and Ghia, K.N., "Low Speed Forced Unsteady Flows," presented at International Symposium on Nonsteady Fluid Dynamics, ASME Fluids Engineering Division Meeting, Toronto, Canada, June 1990.

Papers:

Beltz, S., Ghia, K.N. and Rohling, T., "Study of the Effect of Camber on Window of Chaos for Flow Past a Joukowski Airfoil," presented at AIAA 18th Annual Mini-Symposium on Aerospace Science and Technology, Dayton, Ohio, March 1992.

*Blodgett, K. and Ghia, K.N., "A Spectral Method for Solution of the Navier-Stokes Equations for Arbitrary Geometries," presented at AIAA 18th Annual Mini-Symposium on Aerospace Science and Technology, Dayton, Ohio, March 1992.

Ding, Z., Ghia, K.N., Osswald, G.A. and Ghia, U., "Simulation of Flow Inside a Backstep Duct Using 3-D Unsteady Incompressible Navier-Stokes Equations," presented at AIAA 18th Annual Mini-Symposium on Aerospace Science and Technology, Dayton, Ohio, March 1992.

Huang, Y., Ghia, U. and Osswald, G.A., "3-D Vorticity-Velocity Simulation of an Afterbody Flow," presented at AIAA 18th Annual Mini-Symposium on Aerospace Science and Technology, Dayton, Ohio, March 1992.

Melde, P.F. and Ghia, K.N., "Investigation of Vorticed Flows Over Slender Delta Wings," presented at AIAA 18th Annual Mini-Symposium on Aerospace Science and Technology, Dayton, Ohio, March 1992.

Noll, C., Ghia, K.N. and Muralirayan, K.S., "Analysis of Dynamic Stall Phenomenon for Oscillating Airfoil," presented at AIAA 18th Annual Mini-Symposium on Aerospace Science and Technology, Dayton, Ohio, March 1992.

Wu, H.C., Ghia, K.N. and Ghia, U., "Evaluation of Third-Order Upwind Difference Schemes Using Flow Inside Backstep Channel," presented at AIAA 18th Annual Mini-

---

* Best Paper Award, 1992.

Symposium on Aerospace Science and Technology, Dayton, Ohio, March 1992.

Yang, J., Ghia, K.N., Osswald, G.A. and Ghia, U., "Active Control of the Dynamic Stall Vortex Using Modulated Suction and Injection," presented at AIAA 18th Annual Mini-Symposium on Aerospace Science and Technology, Dayton, Ohio, March 1992.

Ghia, K.N., Yang, J., Osswald, G.A. and Ghia, U., "Study of the Role of Unsteady Separation in the Formation of Dynamic Stall Vortex," AIAA Paper 92-0196, AIAA 30th Aerospace Sciences Meeting, Reno, Nevada, January 1991.

Blodgett, K., Ghia, K.N., Osswald, G.A. and Ghia, U., "Pulsating Flow Past an Elliptic Cylinder," Bull. Am. Phys. Soc., Vol. 36, No. 10, pp. 2656-2657, 1991, presented at the 44th Annual APS Meeting, Scottsdale, Arizona, November 1991.

Ding, Z., Ghia, K.N., Osswald, G.A. and Ghia, U., "Simulation of Flow Inside a Backstep Duct by Unsteady Three-Dimensional Navier-Stokes Equations," Bull. Am. Phys. Soc., Vol. 36, No. 10, pp. 2621-2622, 1991, presented at the 44th Annual APS Meeting, Scottsdale, Arizona, November 1991.

Thornburg, H.J., Ghia, U. and Ghia, K.N., "Study of Free Shear Layer Instability and Vortex Development Using a Flow Adaptive Grid Technique," Bull. Am. Phys. Soc., Vol. 36, No. 10, pp. 2645-246, 1991, presented at the 44th Annual APS Meeting, Scottsdale, Arizona, November 1991.

Ding, Z., Ghia, K.N., Ghia, U. and Osswald, G.A., "Hybrid Method for Solution of Three-Dimensional Unsteady Incompressible Navier-Stokes Equations," presented at AIAA 17th Annual Mini-Symposium on Aerospace Science and Technology, Dayton, Ohio, March 1991.

Ghia, K.N., Yang, J., Osswald, G.A. and Ghia, U., "Study of Dynamic Stall Mechanism Using Simulation of Two-Dimensional Unsteady Navier-Stokes Equations," presented at AIAA 17th Annual Mini-Symposium on Aerospace Science and Technology, Dayton, Ohio, March 1991.

Huang, Y., Osswald, G.A. and Ghia, K.N., "Application of a Multi-Grid Method in Numerical Solution of Unsteady 3-D Navier-Stokes Equations," presented at AIAA 17th Annual Mini-Symposium on Aerospace Science and Technology, Dayton, Ohio, March 1991.

Rohling, T., Ghia, K.N., Osswald, G.A. and Ghia, U., "Nonlinear Shear Layer Interaction in a Chaotic External Flow," presented at AIAA 17th Annual Mini-Symposium on Aerospace Science and Technology, Dayton, Ohio, March 1991.

Shirooni, S., Ghia, U., Ghia, K.N. and Osswald, G.A., "Vortex-Ring Interactions in an Axisymmetric Combustor Flow Configuration," presented at AIAA 17th Annual Mini-Symposium on Aerospace Science and Technology, Dayton, Ohio, March 1991

**Thornburgh, H.J., Ghia, U. and Ghia, K.N., "Efficient Adaptive-Grid Simulation of Unsteady Separated Internal Flow," presented at AIAA 17th Annual Mini-Symposium on Aerospace Science and Technology, Dayton, Ohio, March 1991.

Yang, J., Ghia, K.N., Osswald, G.A. and Ghia, U., "Study of Initial Acceleration on the Development of Dynamic Stall Vortex for an Airfoil Pitching at Constant Rate," presented at AIAA 17th Annual Mini-Symposium on Aerospace Science and Technology, Dayton, Ohio, March 1991.

Ghia, K.N., Yang, J., Osswald, G.A. and Ghia, U., "Study of Dynamic Stall Mechanism Using Simulation of Two-Dimensional Unsteady Navier-Stokes Equations," presented at 29th Aerospace Sciences Meeting, Reno, Nevada, January 7-10, 1991.

Ghia, U., Shirooni, S., Ghia, K.N. and Osswald, G.A., "Examination of a Vortex Ring Interaction Phenomenon in an Axisymmetric Flow," presented at 29th Aerospace Sciences Meeting, Reno, Nevada, January 7-10, 1991.

Ghia, K.N., Ghia, U. and Osswald, G.A., "Characterization of Dynamic Stall Phenomenon Using Two-Dimensional Unsteady Navier-Stokes Equations," Proceedings of NASA/AFOSR/ARO Workshop on Physics of Forced Unsteady Separation, Moffett Field, California, April 1990.

Ghia, K.N., "Analyses of Self-Excited Oscillatory Flows," presented at NASA/AFOSR/ARO Workshop on Physics of Forced Unsteady Separation, Moffett Field, California, April 1990.

Ghia, U., "Axisymmetric Vortex-Ring Interactions and Break-Up," presented at NASA/AFOSR/ARO Workshop on Physics of Forced Unsteady Separation, Moffett Field, California, April 1990.

Osswald, G.A., Ghia, K.N. and Ghia, U., "Unsteady Fluid Dynamics of Maneuvering Bodies," presented at AIAA 16th Annual Mini-Symposium on Aerospace Science and Technology, Dayton, Ohio, March 1990.

Rohling, T., Ghia, K.N., Osswald, G.A. and Ghia, U., "Prediction of Chaotic Flow Using Navier-Stokes Equations," presented at AIAA 16th Annual Mini-Symposium on Aerospace Science and Technology, Dayton, Ohio, March 1990.

Blodgett, K., Osswald, G.A., Ghia, K.N. and Ghia, U., "Bubbles - An Unsteady Numerical Particle Trace Technique," presented at AIAA 16th Annual Mini-Symposium on Aerospace Science and Technology, Dayton, Ohio, March 1990

** Best Paper Award, 1991.

Section 6

STUDENT DEGREE THESES AND DISSERTATIONS

M.S. Degree Theses

Blodgett, K.E.J., "Unsteady Separated Flow Past an Elliptic Cylinder Using the Two-Dimensional Incompressible Navier-Stokes Equations," M.S. Thesis, Department of Aerospace Engineering and Engineering Mechanics, University of Cincinnati, Cincinnati, Ohio, March 1990.

Rohling, T., "Simulation of Chaotic Flows Past Airfoils at High Incidence Using the Unsteady Navier-Stokes Equations," M.S. Thesis, Department of Aerospace Engineering and Engineering Mechanics, University of Cincinnati, Cincinnati, Ohio, March 1991.

Melde, P.F., "Investigation of Vortical Flows Over Slender Delta Wings," M.S. Thesis, Department of Aerospace Engineering and Engineering Mechanics, University of Cincinnati, Cincinnati, Ohio, March 1992.

Ph.D. Degree Dissertations

Thornburg, H.J., "An Adaptive-Grid Technique for Simulation of Complex Unsteady Flows," Ph.D. Dissertation, Department of Mechanical, Industrial and Nuclear Engineering, University of Cincinnati, Cincinnati, Ohio, August 1991.

Huang, Y., "Numerical Solution of 3-D Navier-Stokes Equations in Vorticity-Velocity Form For Incompressible Flows," Ph.D. Dissertation, Department of Mechanical, Industrial and Nuclear Engineering, University of Cincinnati, Cincinnati, Ohio, March 1992.

Section 7

TECHNICAL APPLICATIONS

Of the various CFD analyses developed, some were of direct use to the technical community. Although to our knowledge, none of these analyses were used in the development of any specific hardware, they are being used in preliminary design studies by analysts in the industry. Some of these analyses are also being used by other researchers at governmental laboratories to improve their analyses. The following is a list of the CFD analyses and the organizations using them.

Analysis	**Organization**
• Three-Dimensional Unsteady Navier-Stokes Analysis Using Iterative Technique with Multigrid Acceleration	Copeland Corporation Sidney, Ohio
• Flow-Adaptive Grid Technique For Simulation of Unsteady Vortical Flows	McDonnel Douglas Research Center St. Louis, Missouri
• Flow Visualization Technique for Unsteady Viscous Flows	The Ohio Supercomputer Center Columbus, Ohio

Appendix A

Figures for Section 2.A

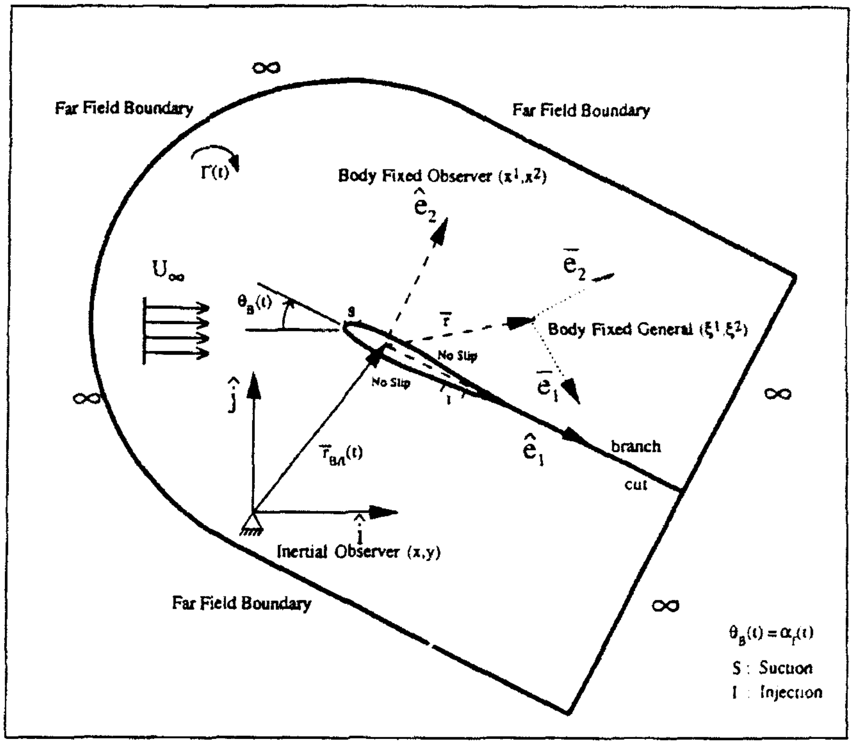

Figure A.1: Inertial/body-fixed coordinate systems and boundary conditions for flow past an arbitrary maneuvering body.

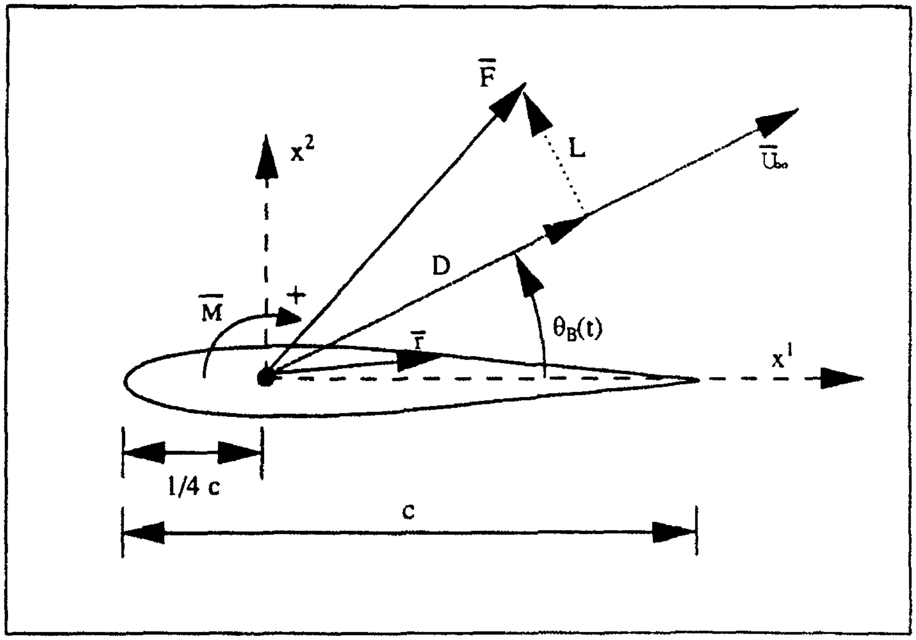

Figure A 2: Depiction of forces and moments on the maneuvering airfoil.

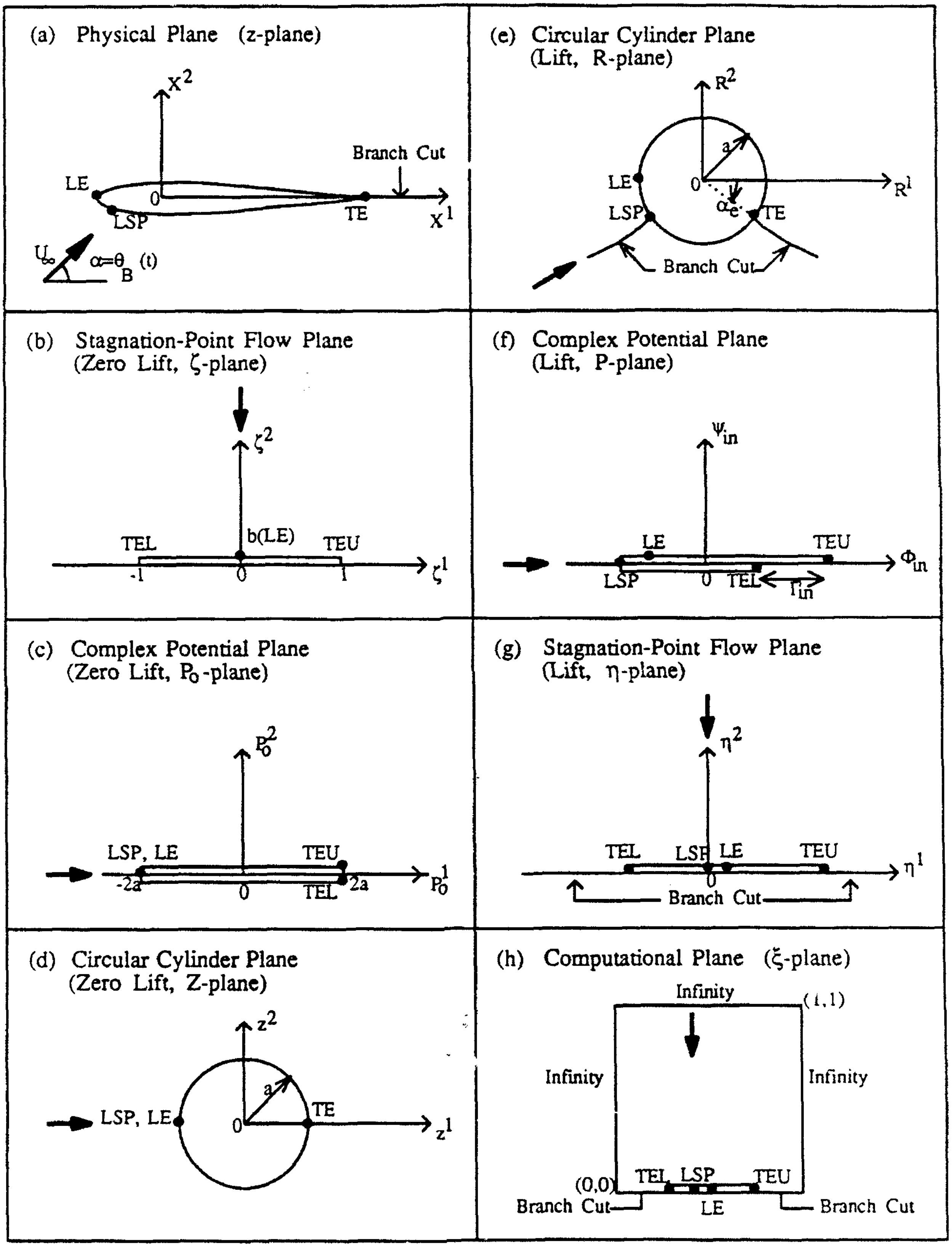

Figure A.3: Representation of inviscid flow past symmetric NACA 0015 airfoil at angle of attac': (with circulation), in physical and various transformed planes.

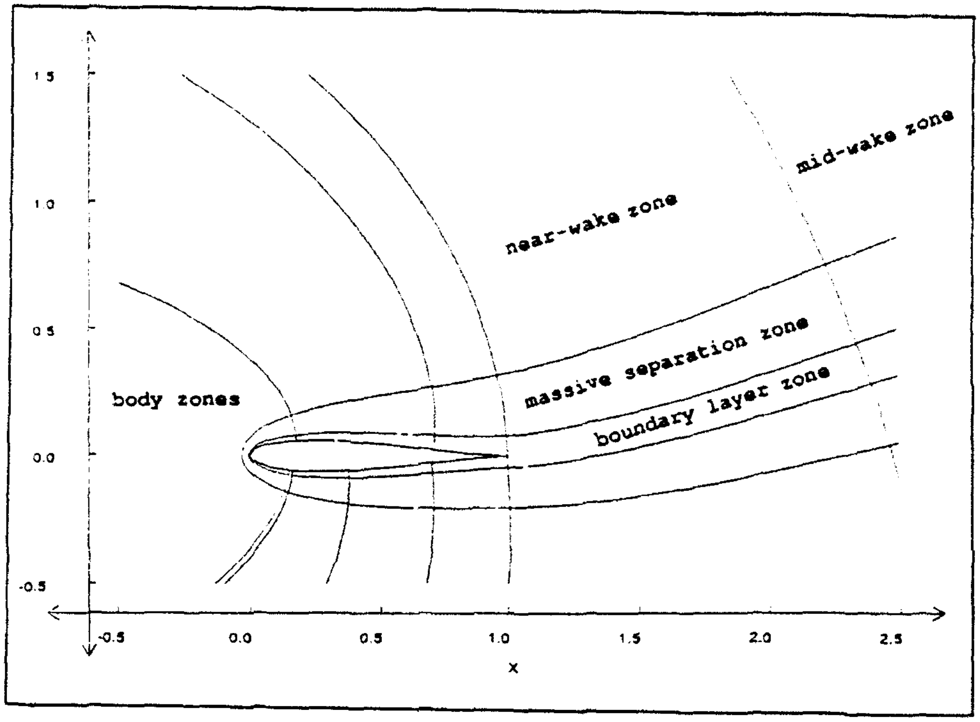

Figure A.4: Depiction of various zones for streamwise and normal 1-D analytical cubic spline clustering transformations.

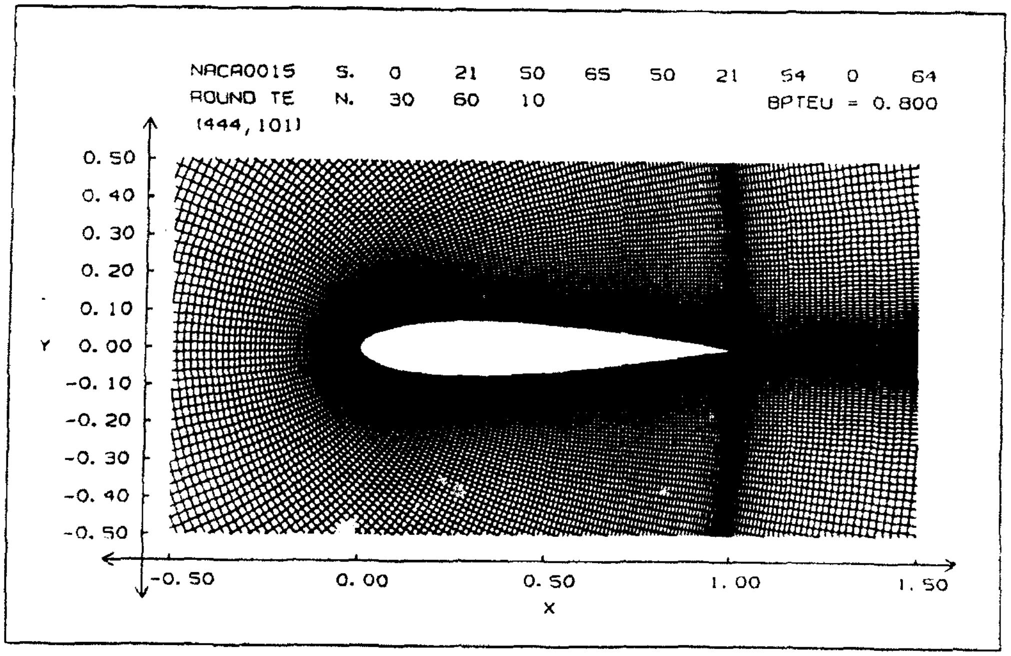

Figure A.5: Grid distribution for a NACA 0015 airfoil with (444 × 101) mesh points.

Constant Pitch-up Motion
NACA 0015 Airfoil, Re = 45,000
Computational Plane, C-Grid (444,101)

Vorticity Distribution (ADI Solution)

(a) Time = 1.50 $\alpha = 20.54^{\circ}$

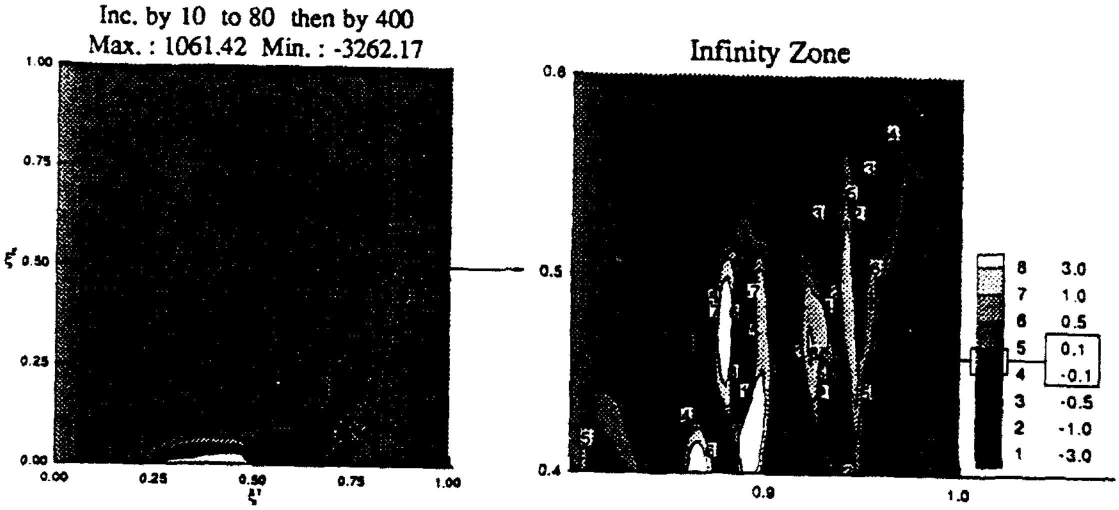

(b) Time = 3.30 $\alpha = 36.58^{\circ}$

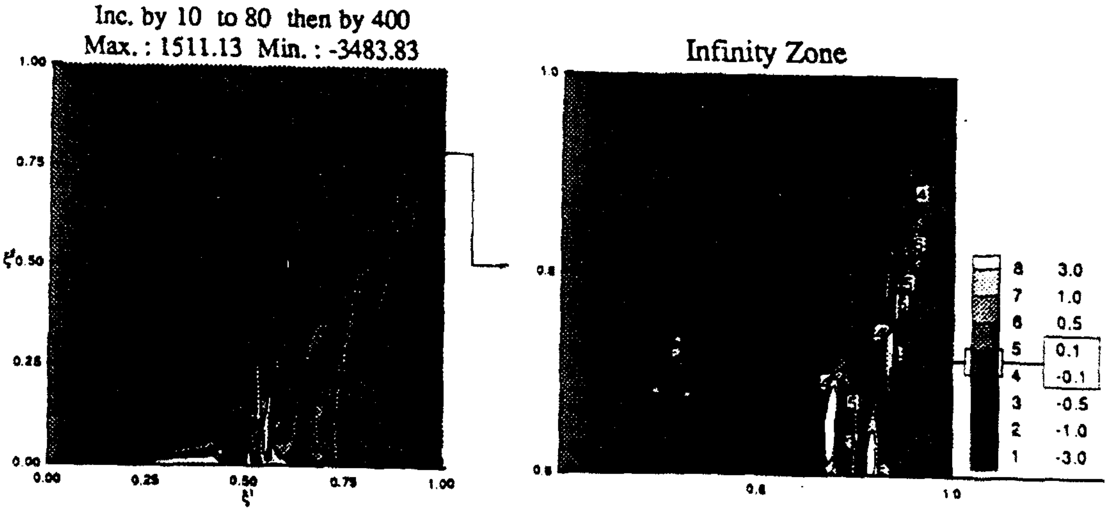

Figure A.6: Effect of grid stretching on far-field solution - vorticity contours. (a) $\alpha = 20.54^{\circ}$, (b) $\alpha = 36.58^{\circ}$.

Constant Pitch-up Motion
NACA 0015 Airfoil, Re = 45,000
Computational Plane, C-Grid (444,101)

Disturbance Stream Function Distribution (BGE Solution)

(a) Time = 1.50 $\alpha = 20.54^\circ$

- Dirichlet (Body Surface, Infinity) with Symmetric Condition (Branch-Cut)
  - Poisson Problem for BGE Solution

- $\alpha = 20.54^\circ$
  Max. $|\Psi_I^D|$: 0.266 at (0.817,0.32)
- $\alpha = 36.58^\circ$
  Max. $|\Psi_I|$: 0.355 at (0.601,0.41)
- $0.0^\circ \leq \alpha \leq 36.58^\circ$
  $0.083 \leq \text{Max.}|\Psi_I^D| \leq 0.355$

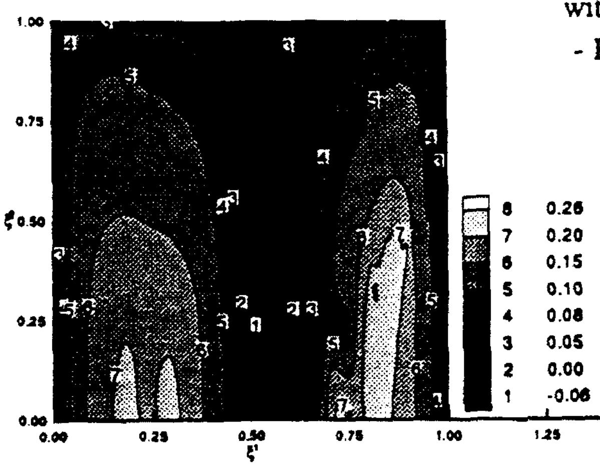

(b) Time = 3.30 $\alpha = 36.58^\circ$

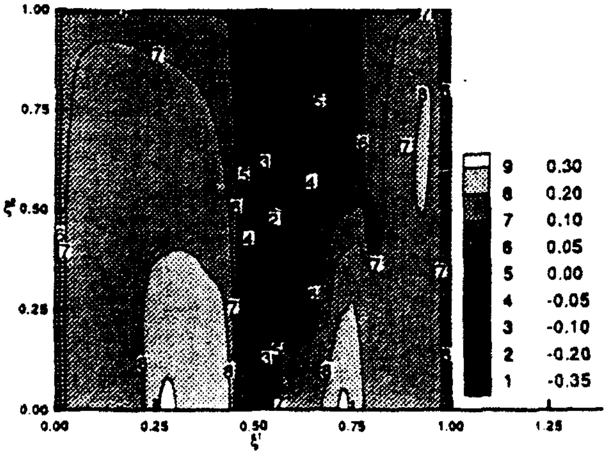

Computational Plane (ξ^1, ξ^2)

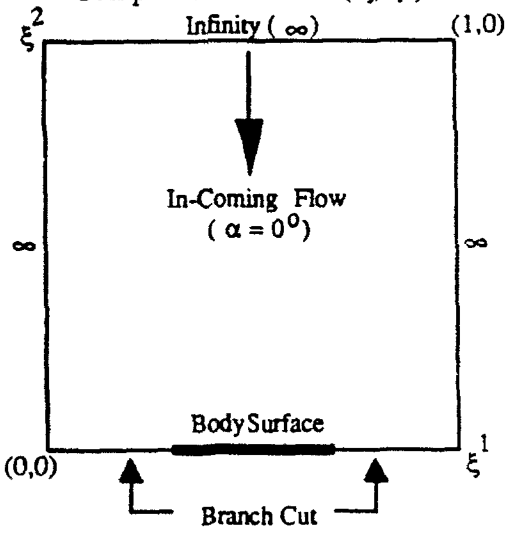

Figure A.7: Effect of grid stretching on far-field solution - disturbance stream function distribution. (a) $\alpha = 20.54^\circ$, (b) $\alpha = 36.58^\circ$.

- Metric Coefficient Distributions
- Computational Plane (ξ^1, ξ^2)
- Grid Size ; (444,101)

(a) G11 Distribution

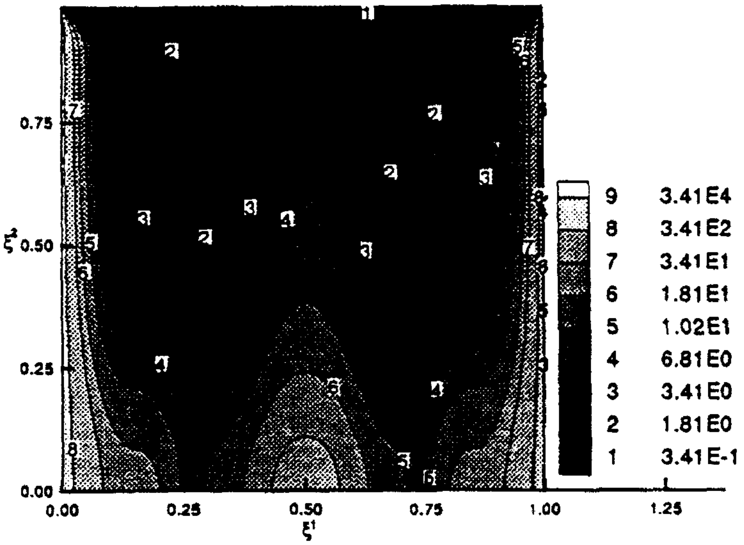

- Max. ; 3.64E4
  at (2.26E-3, 5.0E-3)
  (9.98E-1, 5.0E-3)
- Min. ; 3.63E-3
  at (2.66E-1, 9.95E-1)
  (7.34E-1, 9.95E-1)

(b) G22β Distribution

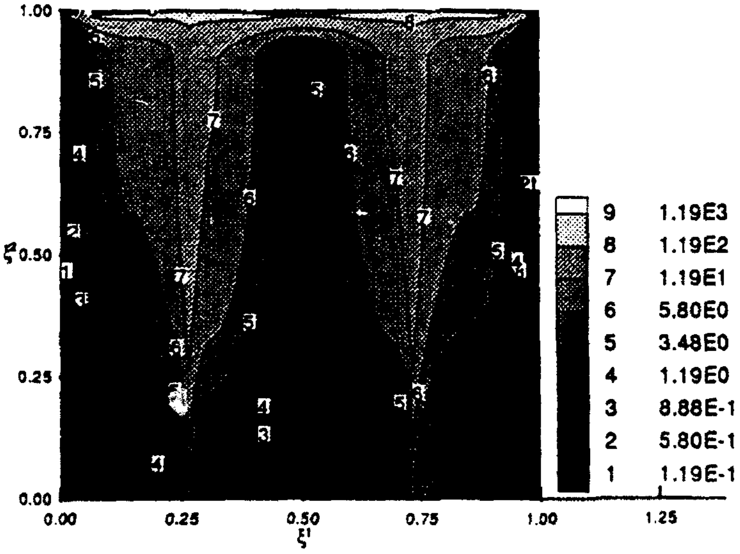

- Max. ; 1.27E3
  at (2.65E-1, 1.0E0)
  (7.35E-1, 1.0E0)
- Min. ; 3.63E-3
  at (1.0E-3, 0.0E0)
  (9.99E-1, 0.0E0)

Figure A.8: Distribution of metric coefficients, for round-off error study (a) G11, (b) G22β.

- Dirichlet-Poisson Problem for BGE Solution
- Computational Plane (ξ^1, ξ^2)
- Truncation Error in Space ; $O((\Delta\xi^1),(\Delta\xi^2))$
  $(\Delta\xi^1)^2 = 5.1E\text{-}6$, $(\Delta\xi^2)^2 = 1.0E\text{-}4$
- Grid Size ; (444,101)

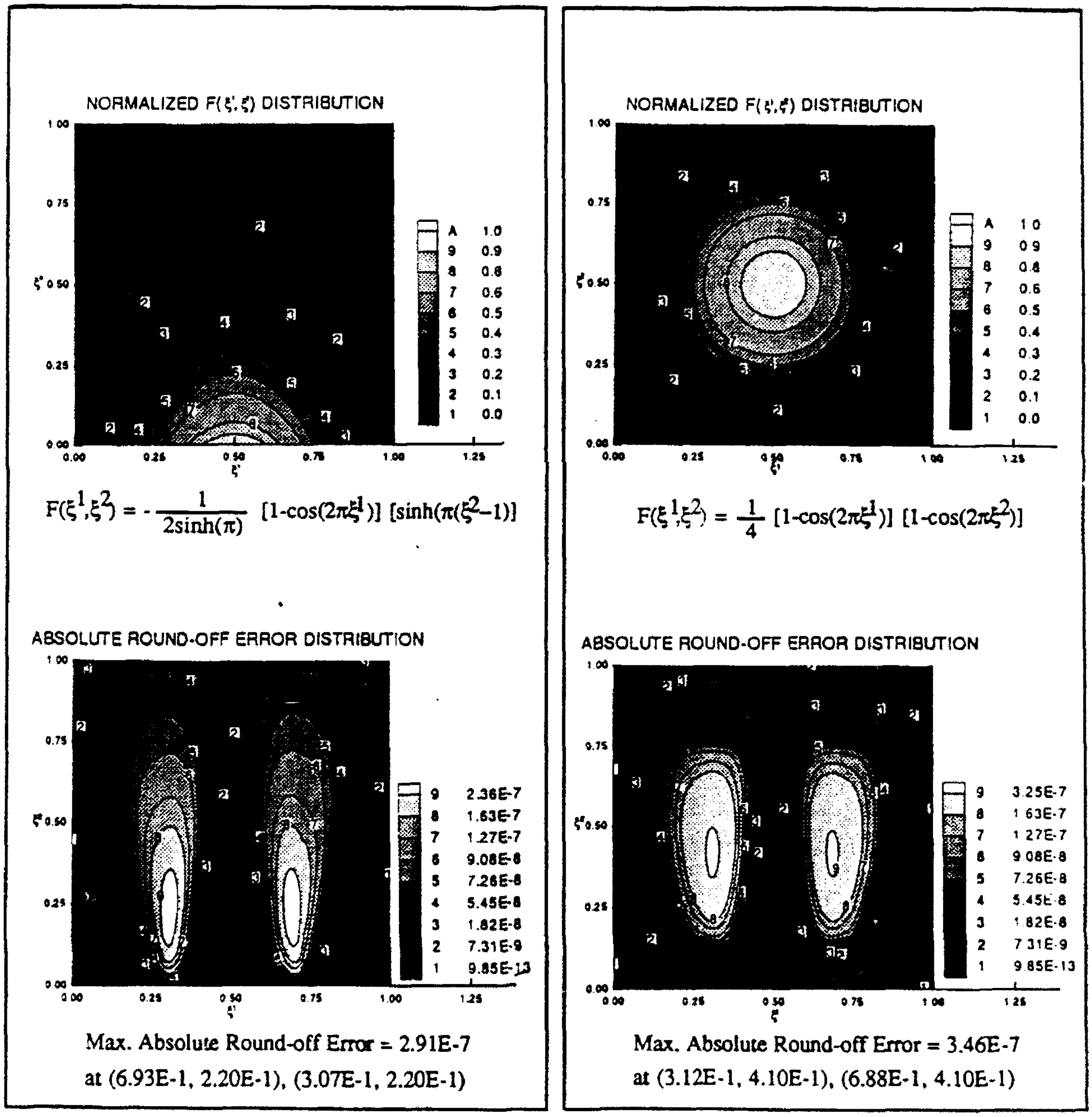

$$F(\xi^1,\xi^2) = -\frac{1}{2\sinh(\pi)}\,[1-\cos(2\pi\xi^1)]\,[\sinh(\pi(\xi^2-1))]$$

$$F(\xi^1,\xi^2) = \frac{1}{4}\,[1-\cos(2\pi\xi^1)]\,[1-\cos(2\pi\xi^2)]$$

Max. Absolute Round-off Error = 2.91E-7
at (6.93E-1, 2.20E-1), (3.07E-1, 2.20E-1)

Max. Absolute Round-off Error = 3.46E-7
at (3.12E-1, 4.10E-1), (6.88E-1, 4.10E-1)

Figure A.9: Estimation of accumulated round-off error distribution due to grid stretching in Block-Gaussian Elimination solution.

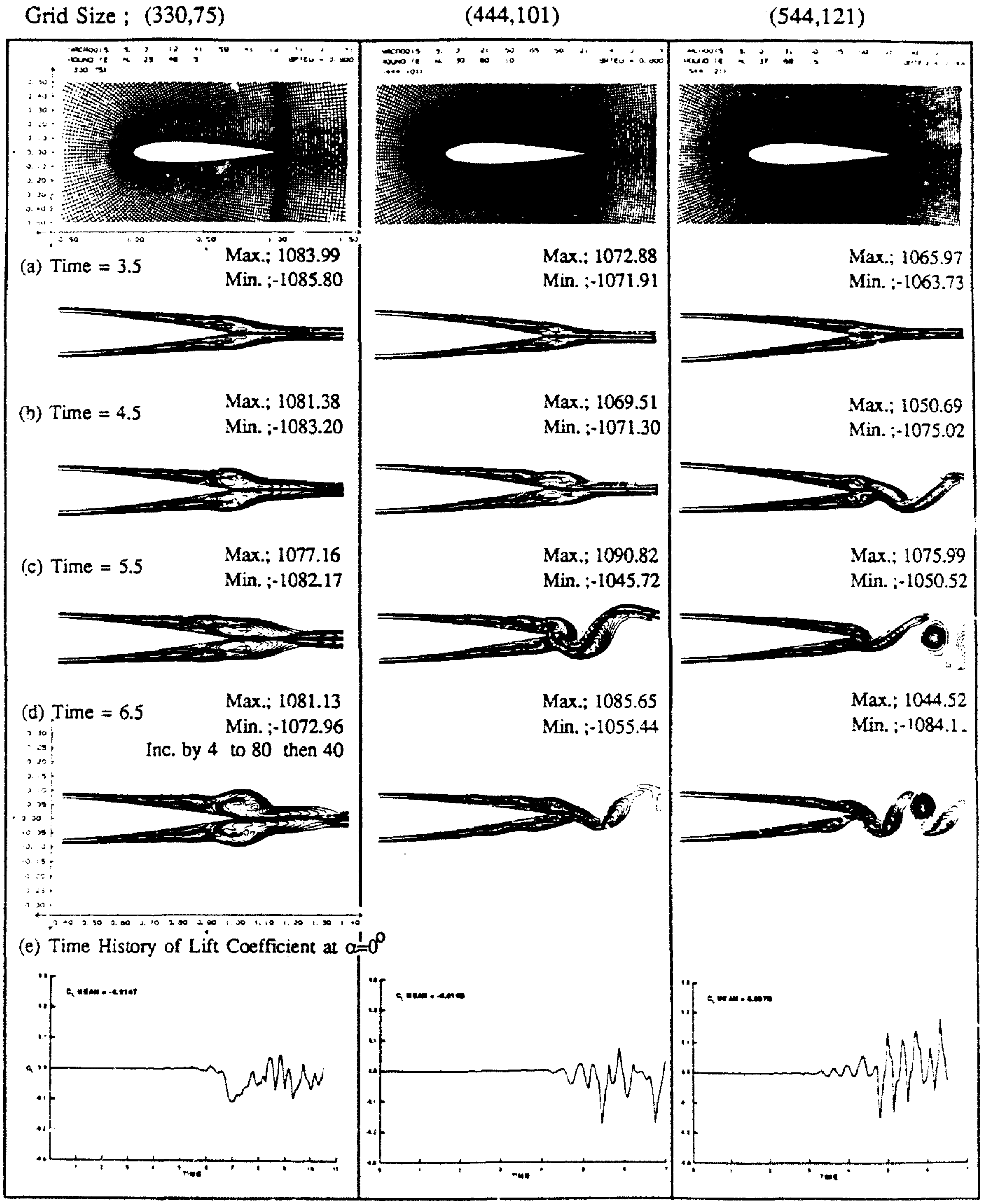

Figure A.10: Effect of three different grid distributions on asymptotic flow solution at $\alpha = 0°$, for Re = 45,000, $\dot{\alpha}^+ = 0.2$. (a-d) vorticity contours near TE, (e) time history of lift coefficient.

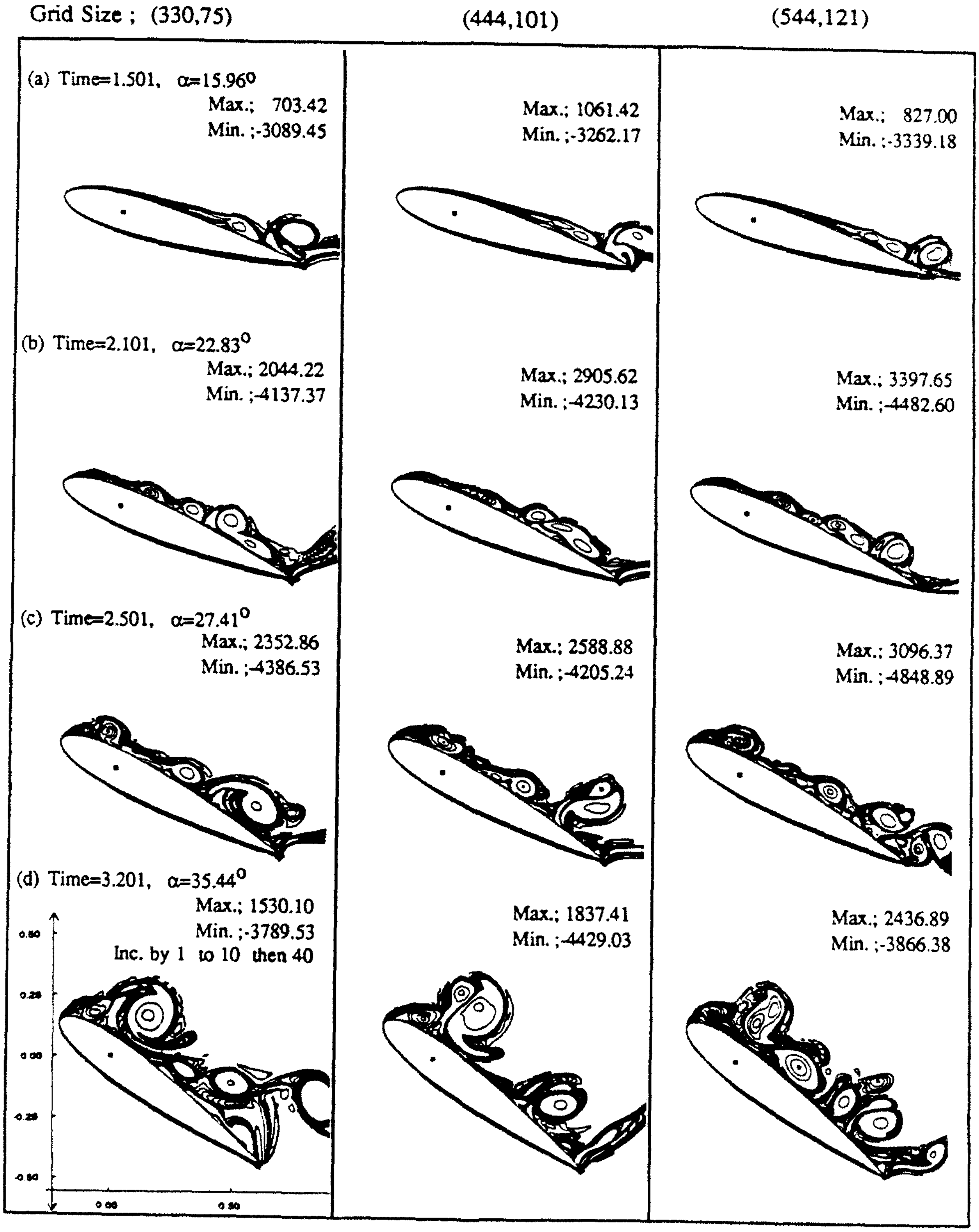

Figure A.11: Effect of three different grid distributions on flow past a NACA 0015 airfoil for Re = 45,000, $\dot{\alpha}^+ = 0.2$ - contours of instantaneous vorticity.

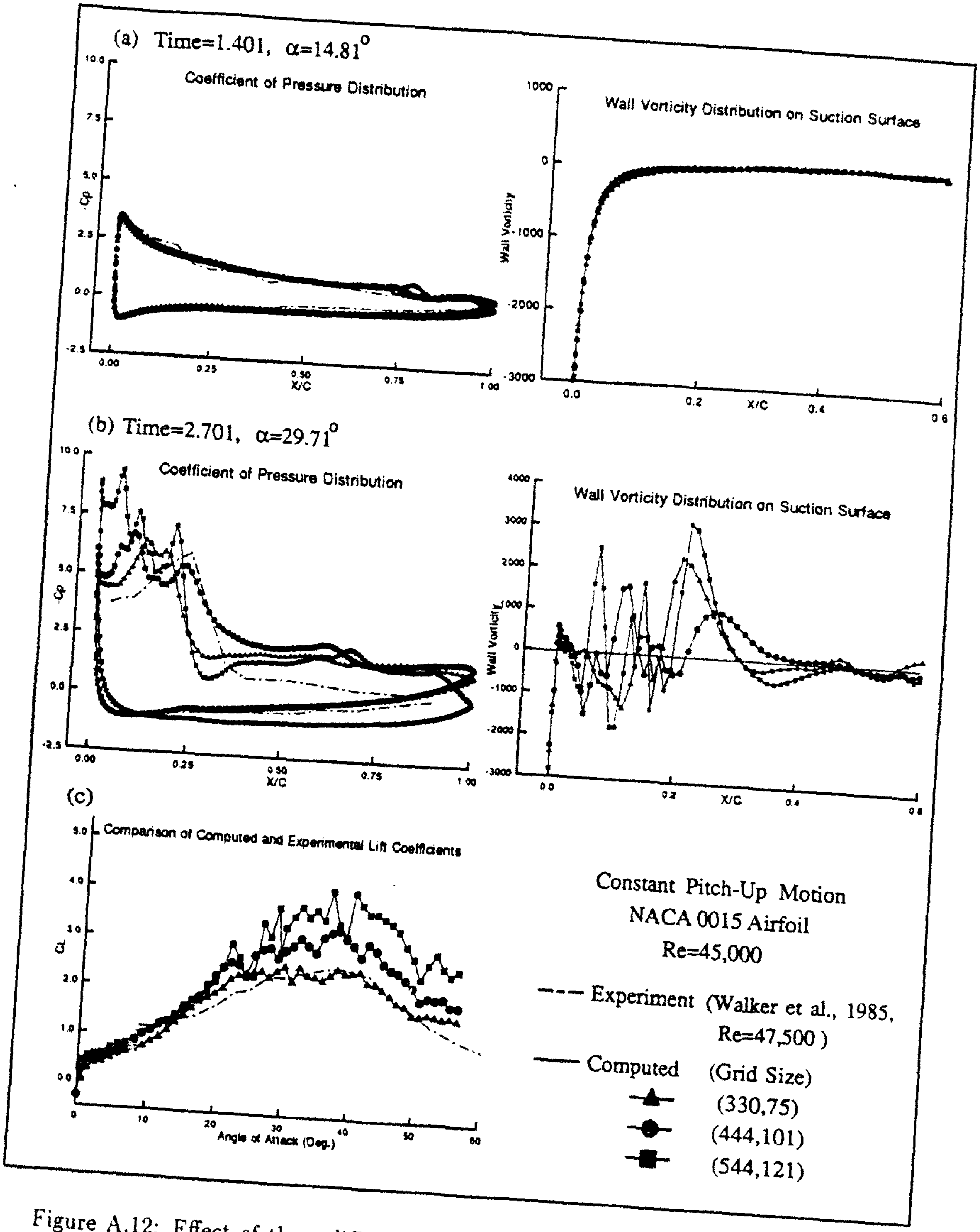

Figure A.12: Effect of three different grid distributions on flow past a NACA 0015 airfoil for Re = 45,000, $\dot{\alpha}^{+} = 0.2$. (a) C_P - distribution and wall vorticity on suction surface at $\alpha = 14.81°$, (b) C_P - distribution and wall vorticity on suction surface at $\alpha = 29.71°$, (c) C_L - distribution.

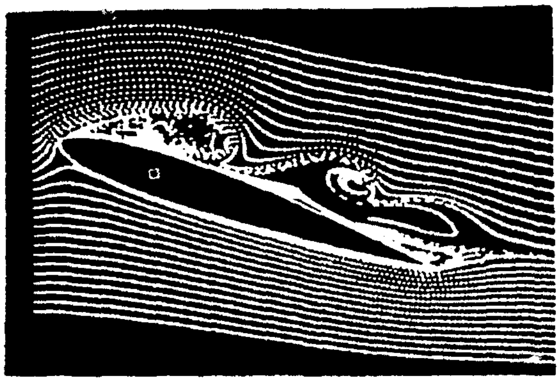

Streak Lines

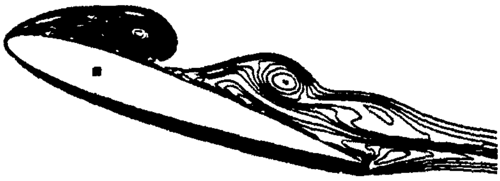

Vorticity Contours

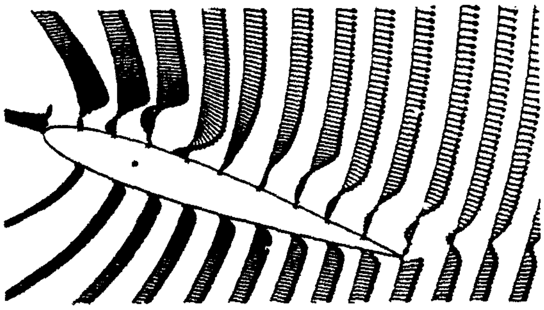

Velocity Vectors

PRESENT

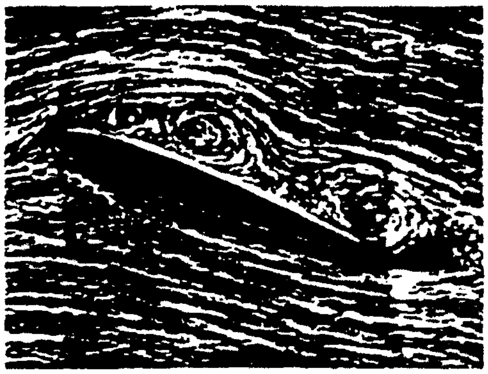

ONERA Experiment
WERLÈ (1976)

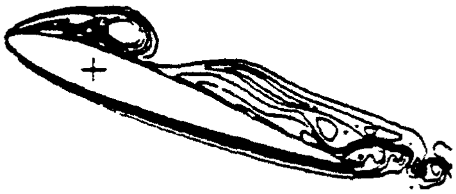

Vorticity Contours

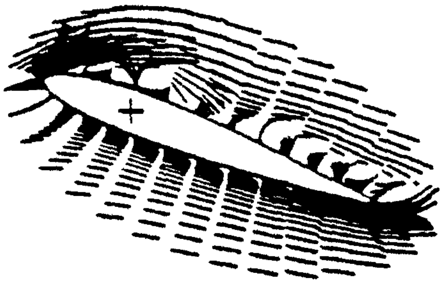

Velocity Vectors

MEHTA (1977)

Figure A.13: Comparison with numerical results of Mehta (1977) and experimental data of Werlé (1976) for NACA 0012 airfoil, Re=5,000, κ=1.0.

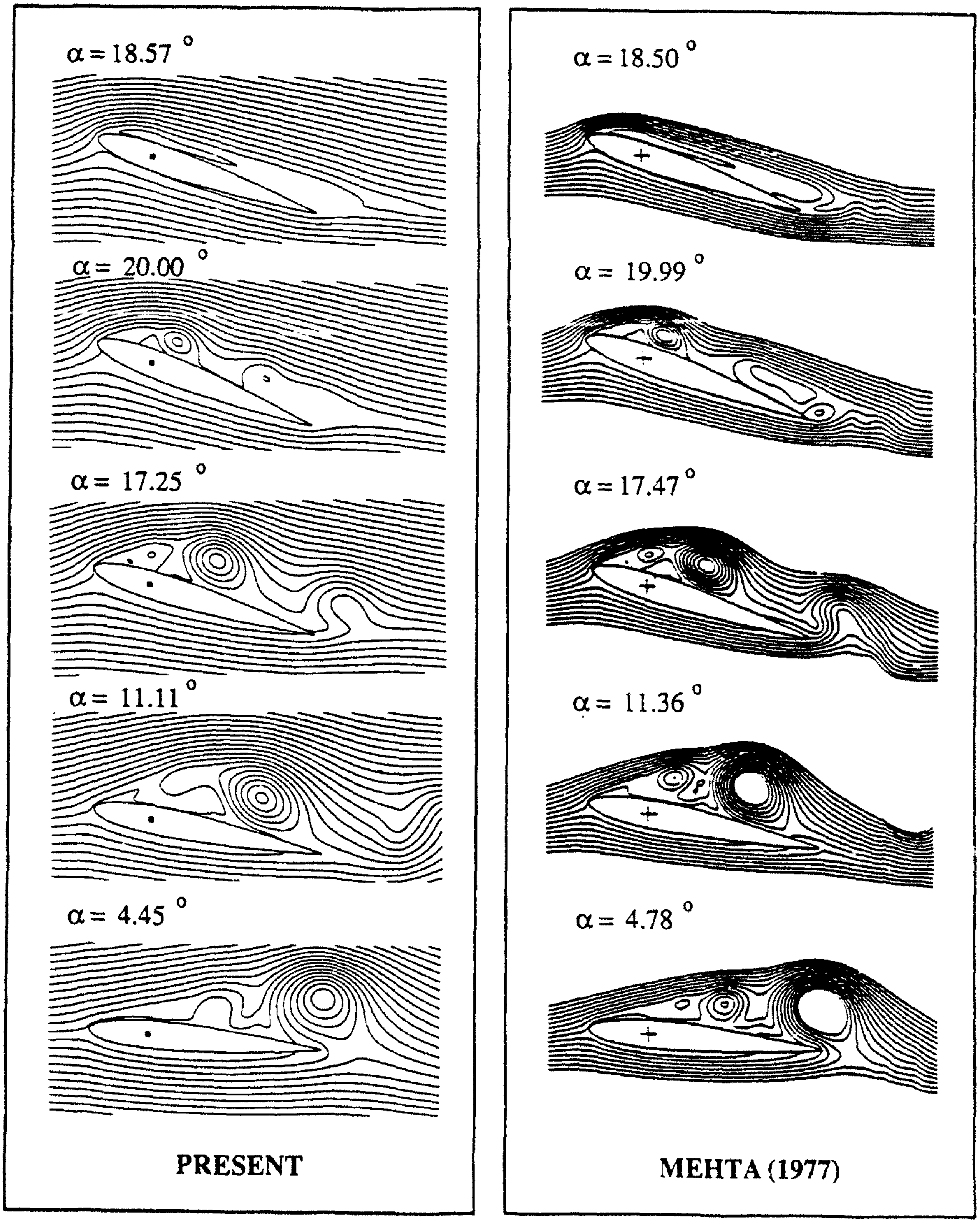

PRESENT

MEHTA (1977)

Figure A.14: Comparison with numerical results of Mehta (1977) for NACA 0012 airfoil, Re=5,000, k=1.0 - instantaneous stream function.

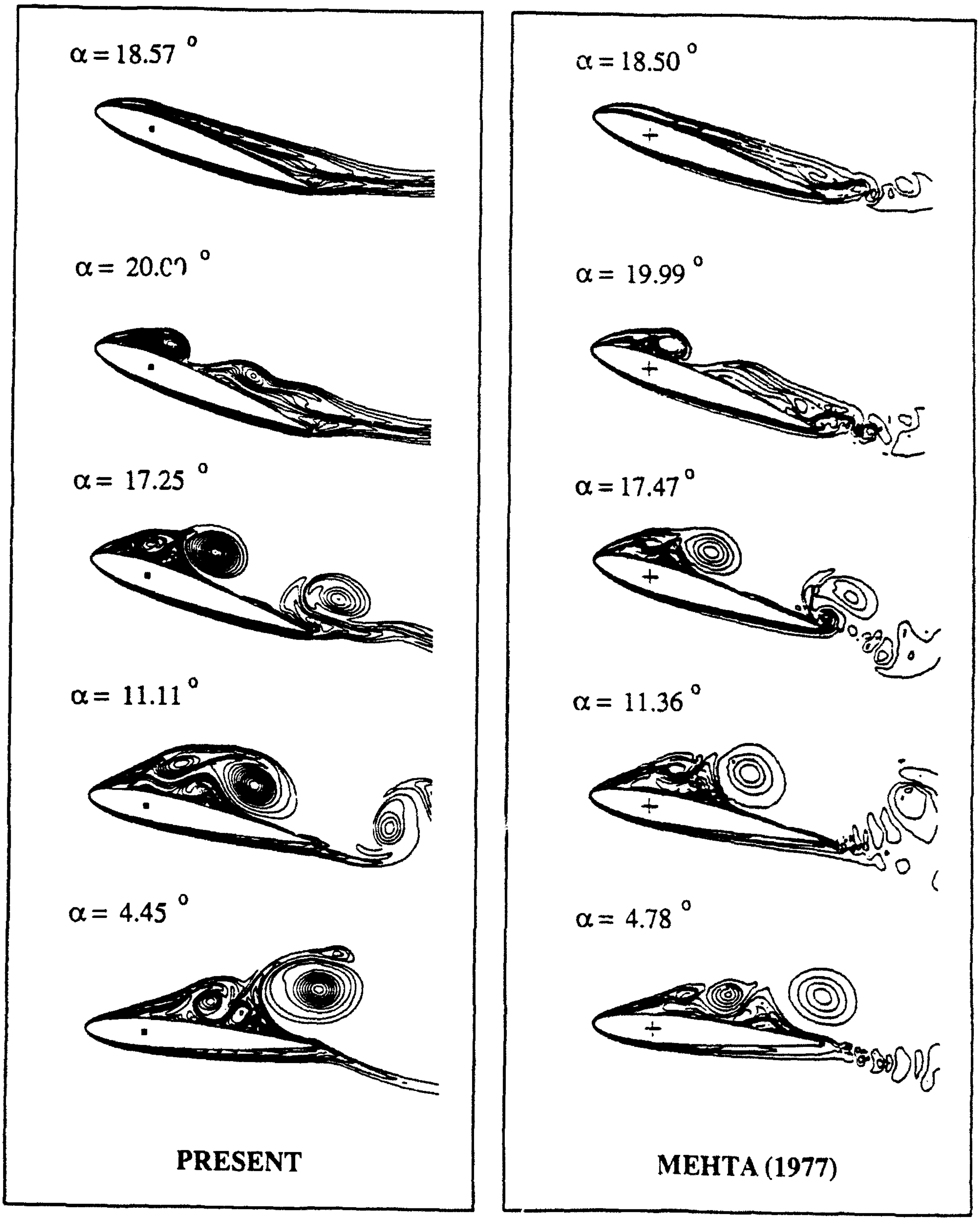

Figure A.15: Comparison with numerical results of Mehta (1977) for NACA 0012 airfoil, Re=5,000, k=1.0 - instantaneous vorticity contours.

(a)

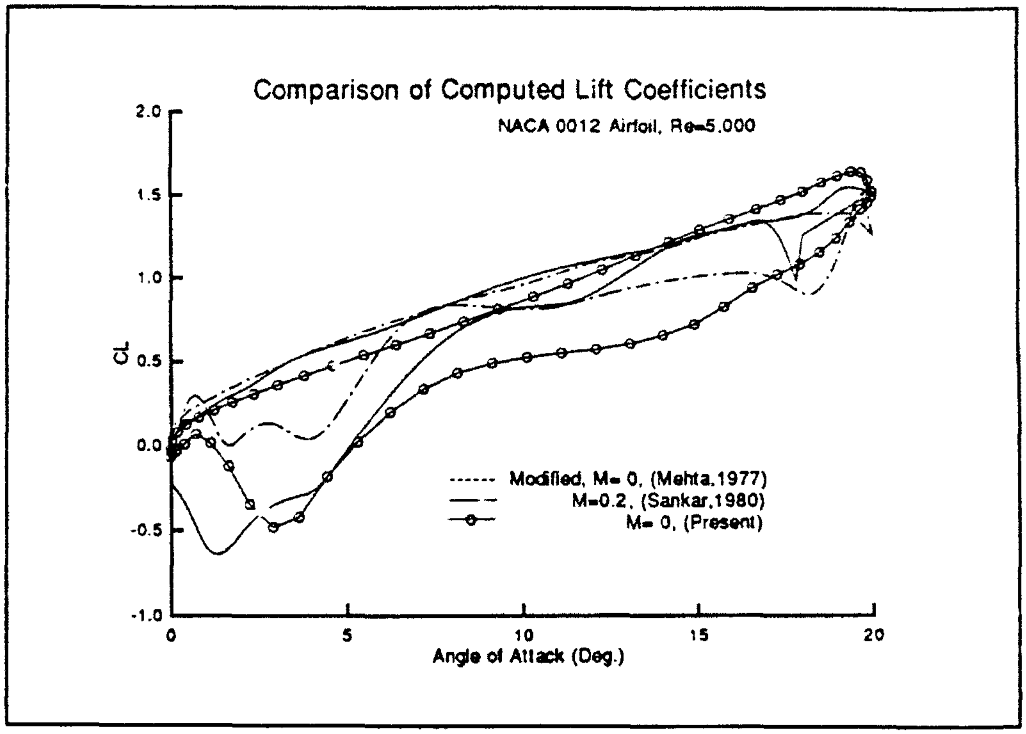

(b) Time = 2.601, α = 18.57° (Pitch-Up) Time = 4.601, α = 11.11° (Pitch-Down)

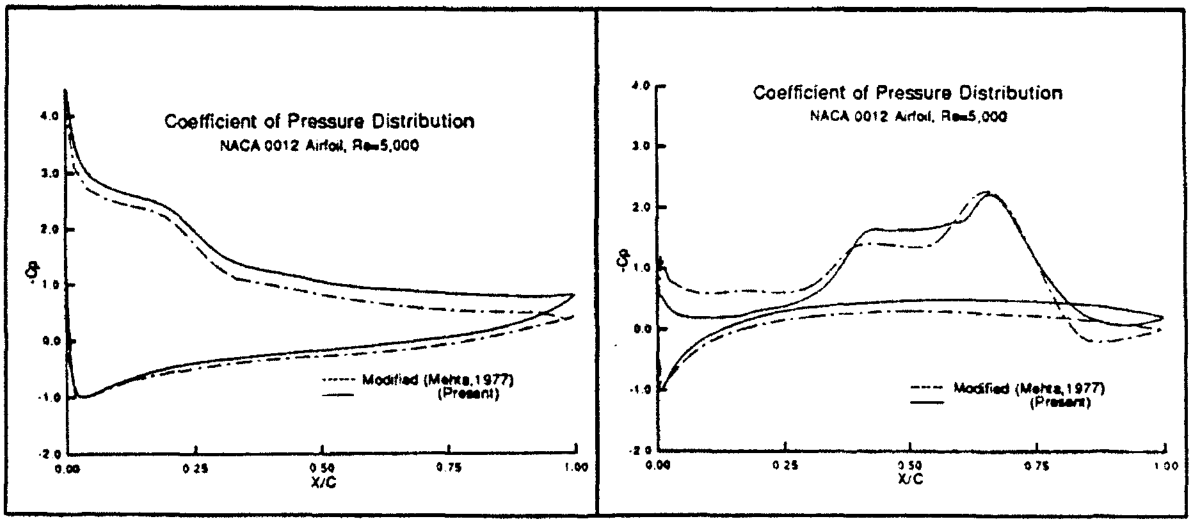

Figure A.16: Comparison with numerical results of Mehta (1977) and Sankar et al. (1980) for NACA 0012 airfoil; Re=5,000, k=1.0. (a) C_L vs. α, (b) C_P - distribution for $\alpha = 18.57°$ (pitch-up) and $\alpha = 11.11°$ (pitch-down).

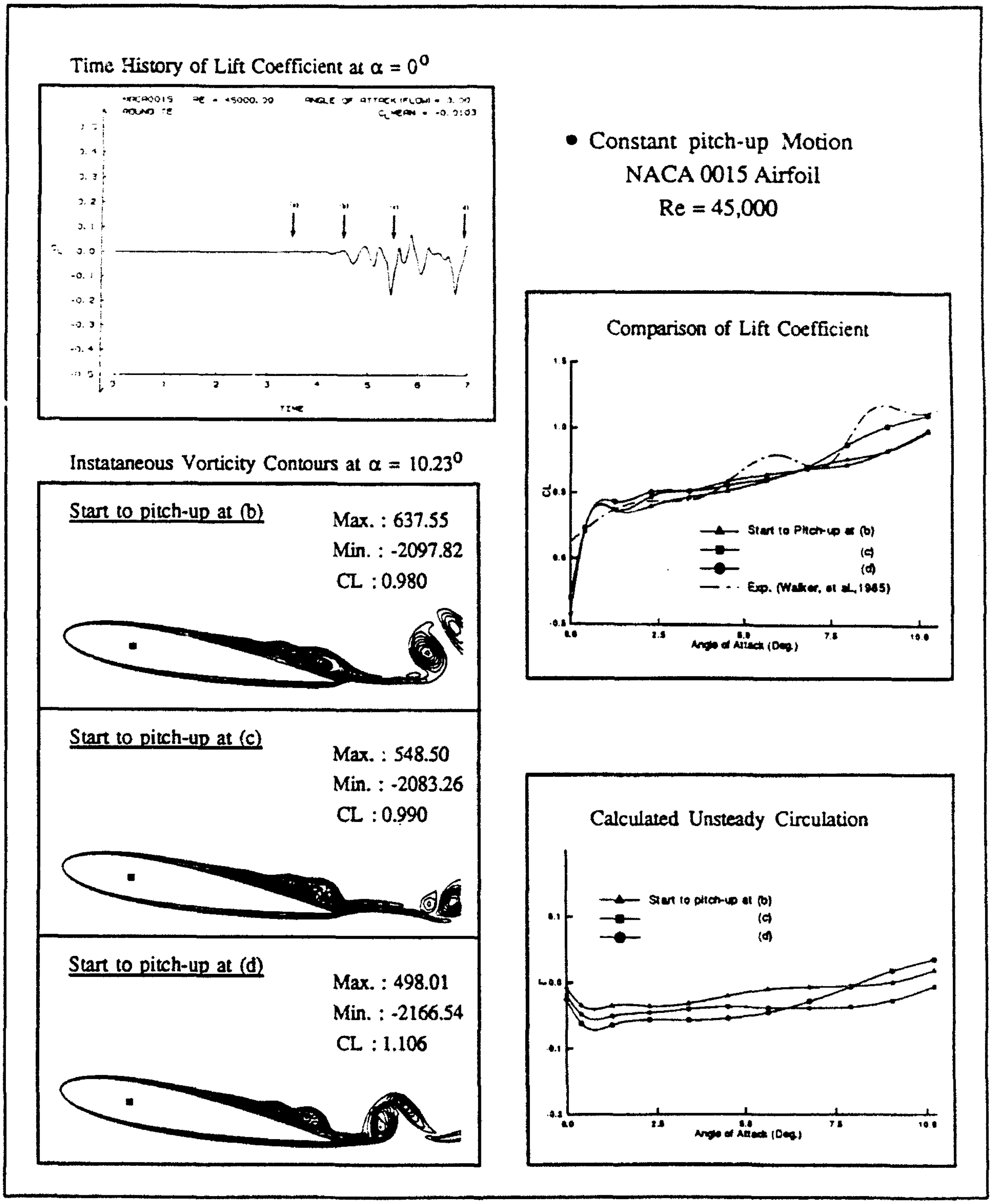

Figure A.17: Effect of three different initial states on flow past a NACA 0015 airfoil; Re = 45,000, $\dot{\alpha}^+ = 0.2$ - vorticity contours, lift coefficients and unsteady circulation.

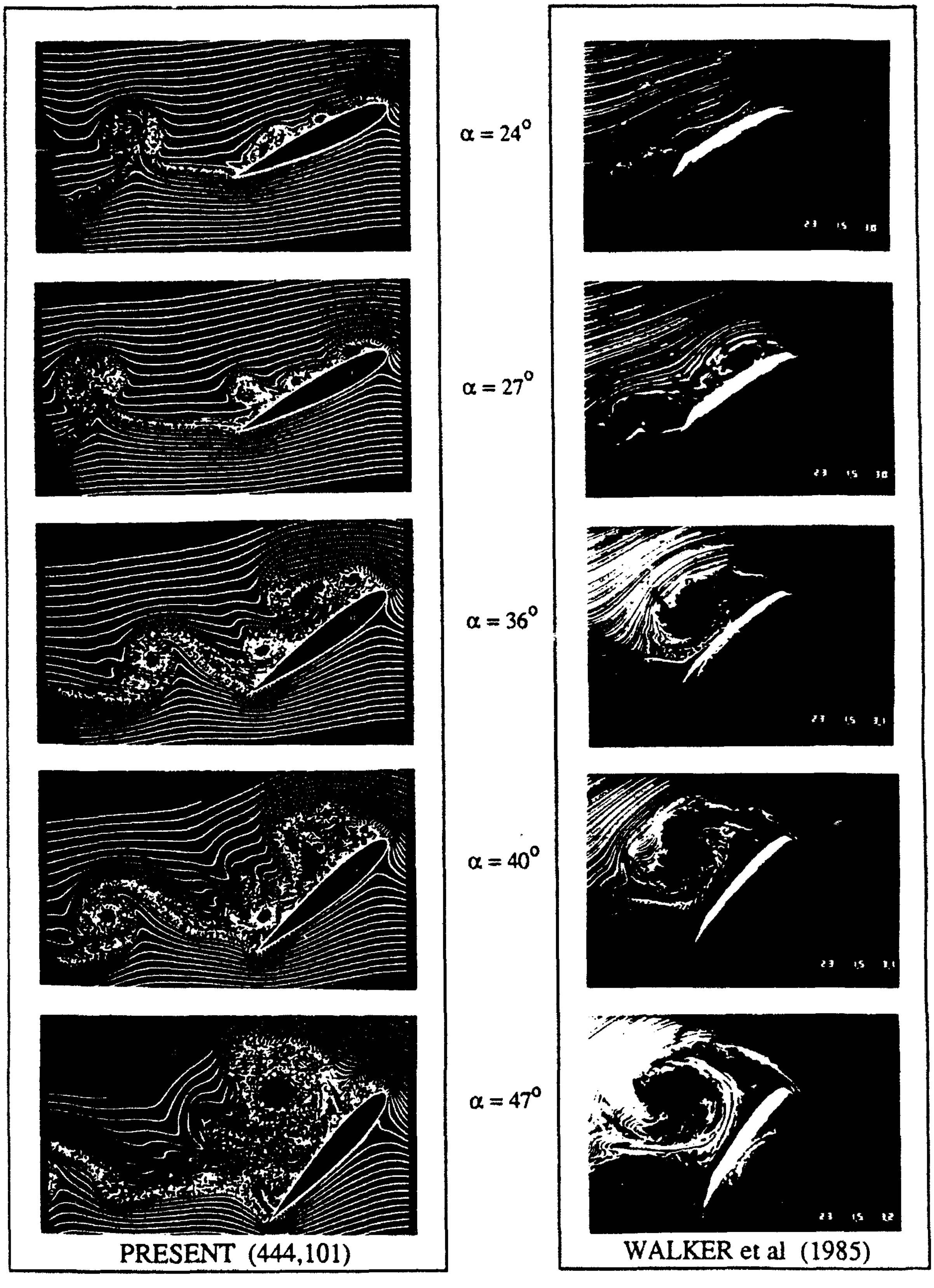

Figure A.18: Comparison with experimental data of Walker et al.(1985) for flow past a NACA 0015 airfoil; Re = 45,000, $\dot{\alpha}^{+} = 0.2$ - streaklines.

(a)

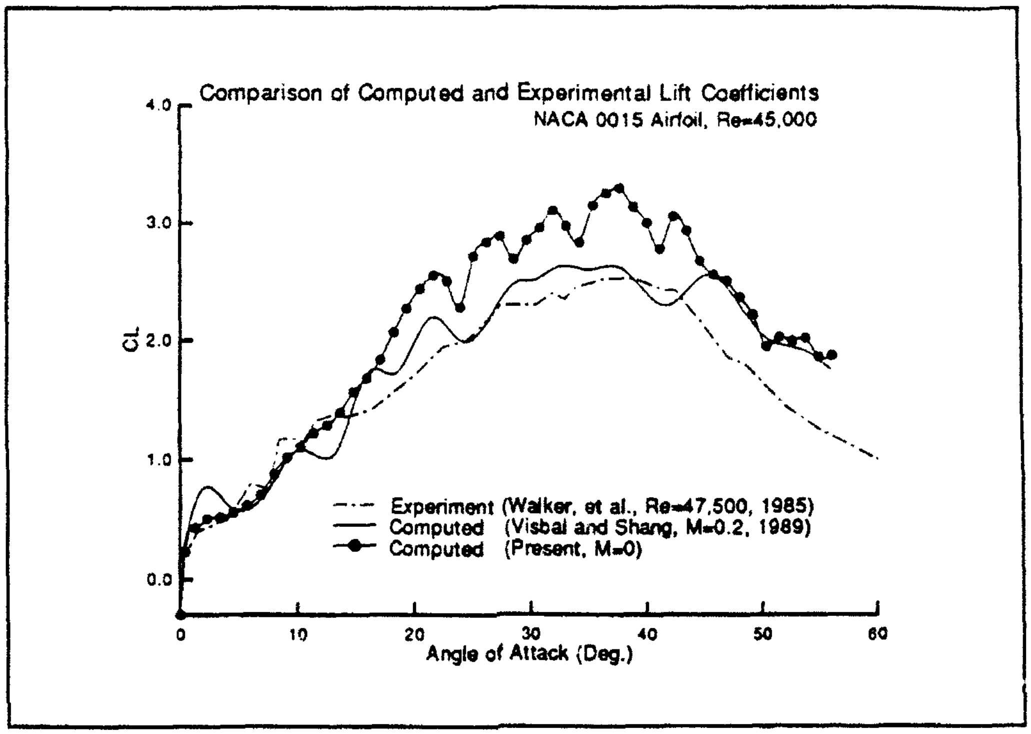

(b) Time = 1.401, $\alpha = 14.81^\circ$ Time = 2.701, $\alpha = 29.71^\circ$

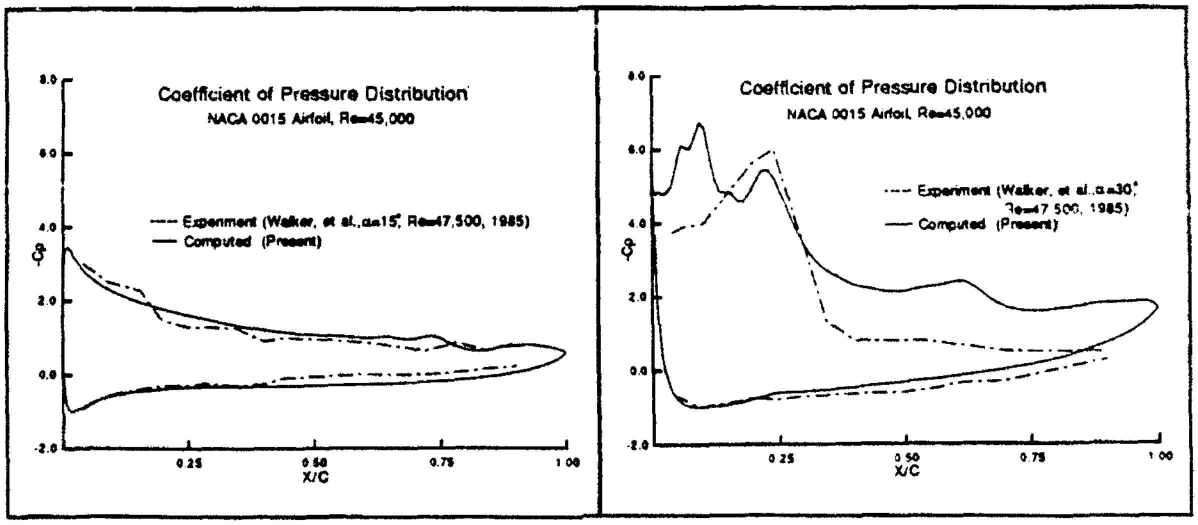

Figure A.19: Comparison with experimental data of Walker et al.(1985) for flow past a NACA 0015 airfoil; Re = 45,000, $\dot{\alpha}^+ = 0.2$. (a) C_L vs. α, (b) C_P - distribution for $\alpha = 14.81^\circ$ and $\alpha = 29.71^\circ$.

(a) Time=1.101, α=11.37°

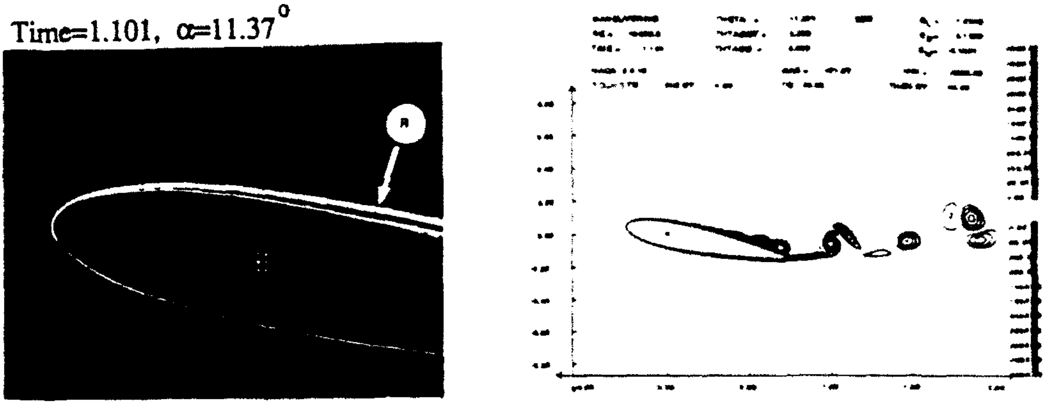

(b) Time=1.501, α=15.96°

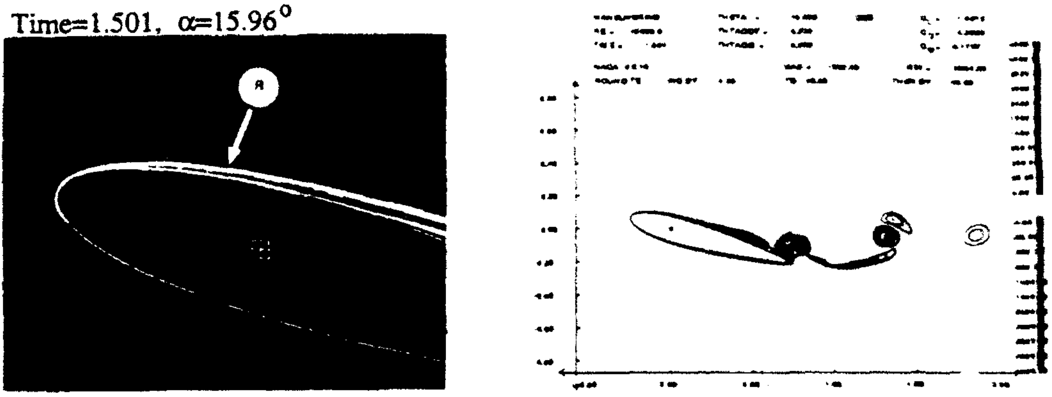

(c) Time=1.701, α=18.25°

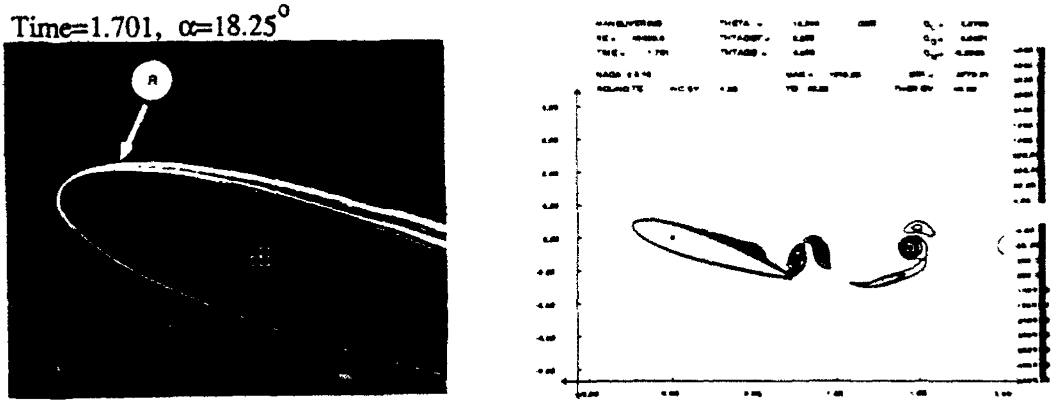

(d) Time=1.901, α=20.54°

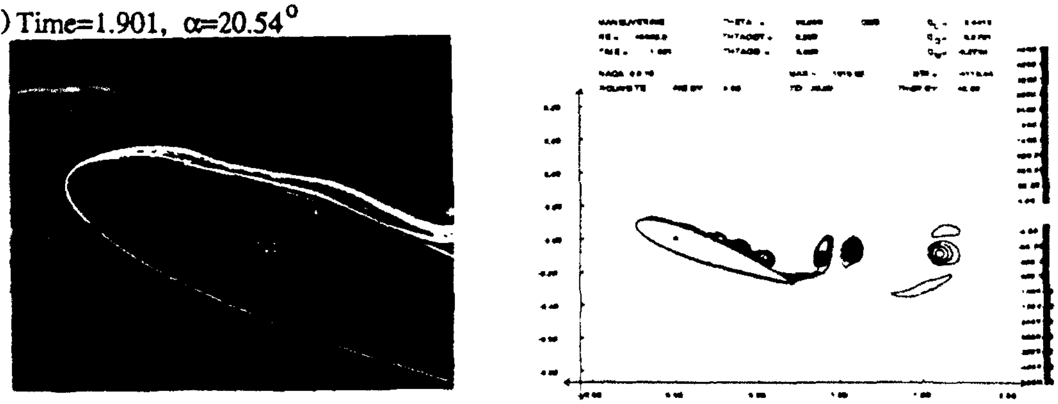

Figure A.20: Details of flow structure for NACA 0015 airfoil; Re= 45,000, $\dot{\alpha}^{+} = 0.2$. - instantaneous vorticity contours for $\alpha = 11.37°, 15.96°, 18.25°$, and $20.54°$.

(a) Time=2.101, α=22.83°

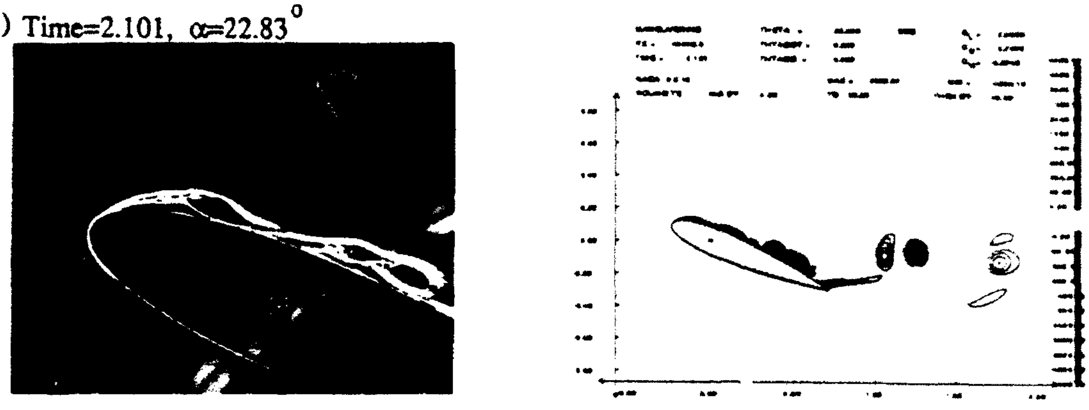

(b) Time=2.401, α=26.27°

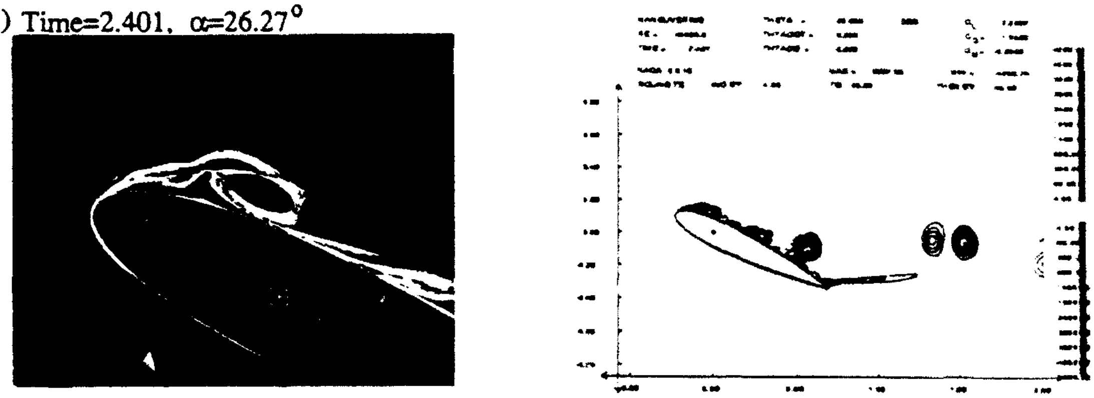

(c) Time=2.601, α=28.56°

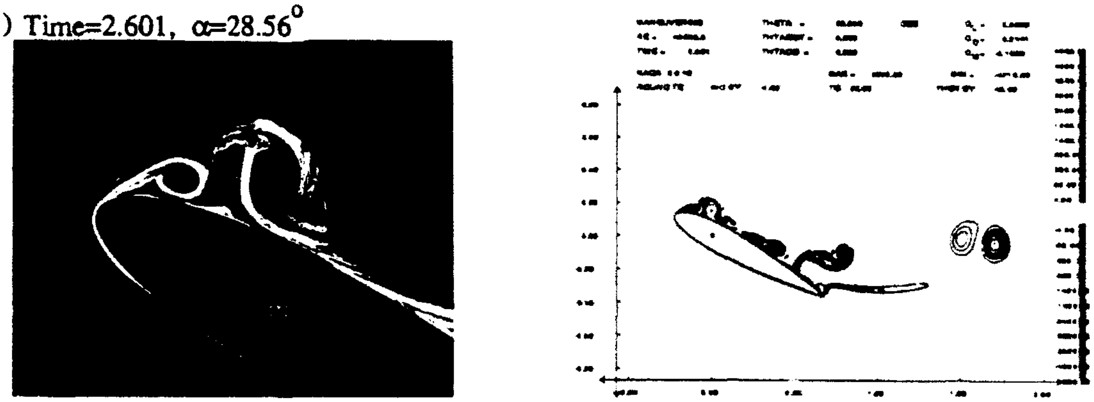

(d) Time=2.701, α=29.71°

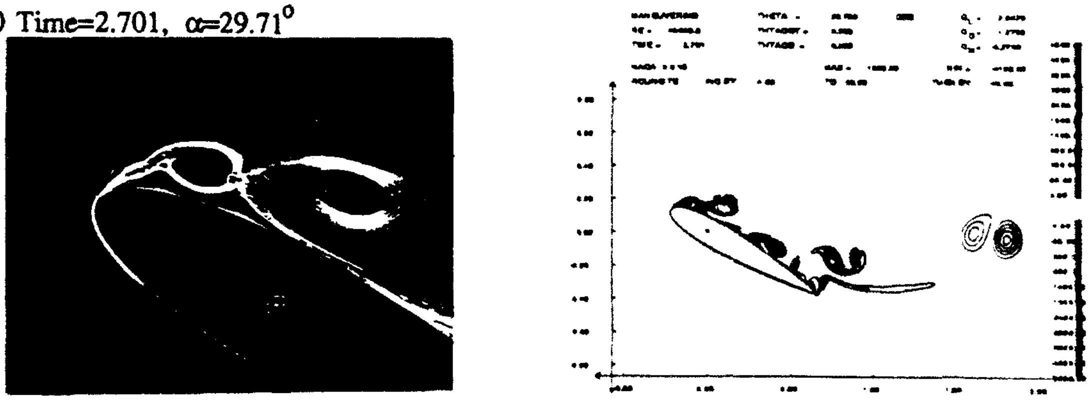

Figure A.21: Details of flow structure for NACA 0015 airfoil; Re= 45,000, $\dot{\alpha}^+ = 0.2$. - instantaneous vorticity contours for $\alpha = 22.83°, 26.27°, 28.56°$, and $29.71°$.

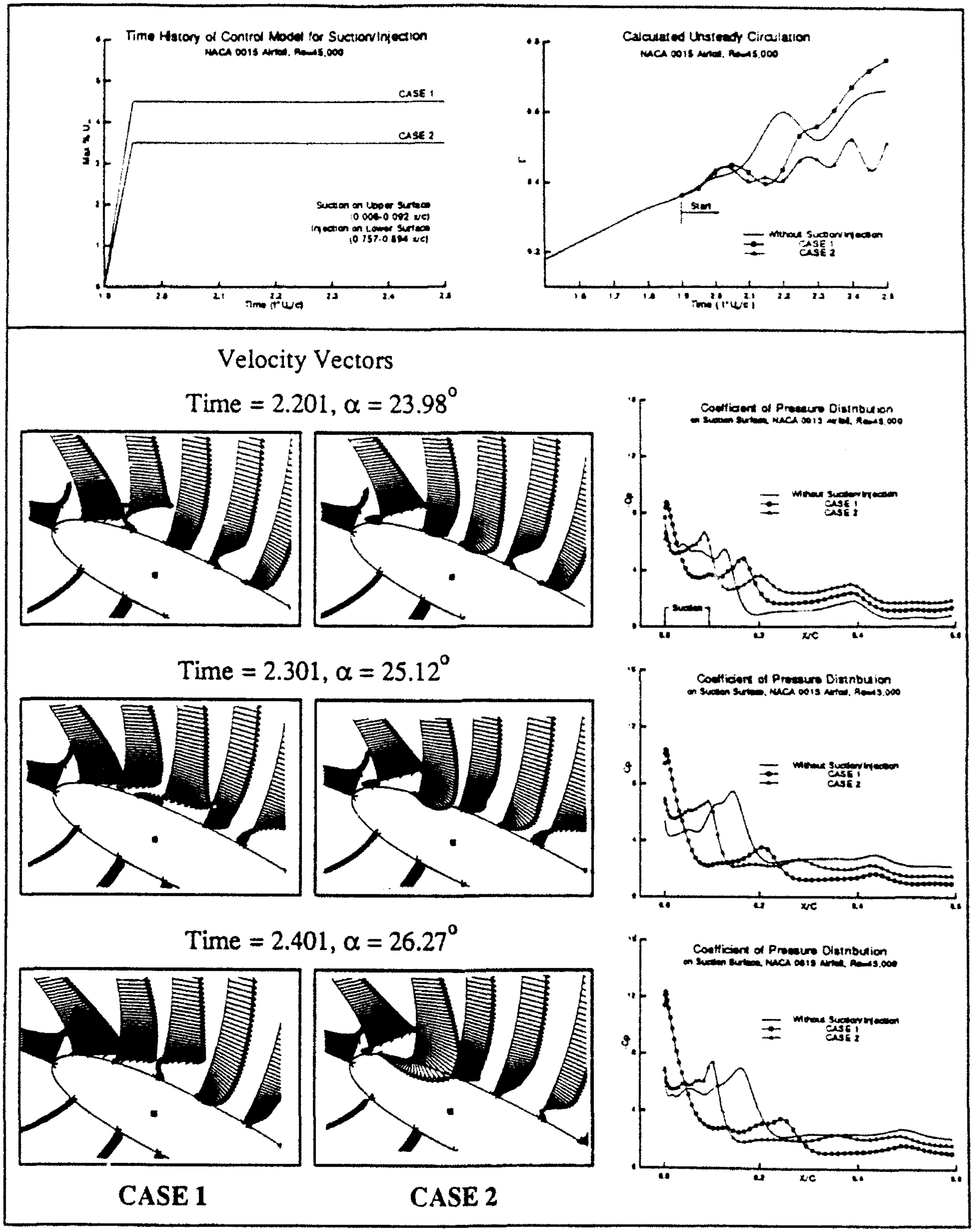

Figure A.22: Effect of suction/injection for NACA 0015 airfoil; Re= 45,000, and $\dot{\alpha}^+ = 0.2$ - unsteady circulation, velocity vectors and C_P - distribution. (i) CASE 1: $v_s/U_\infty = 0.045$, (ii) CASE 2: $v_s/U_\infty = 0.035$.

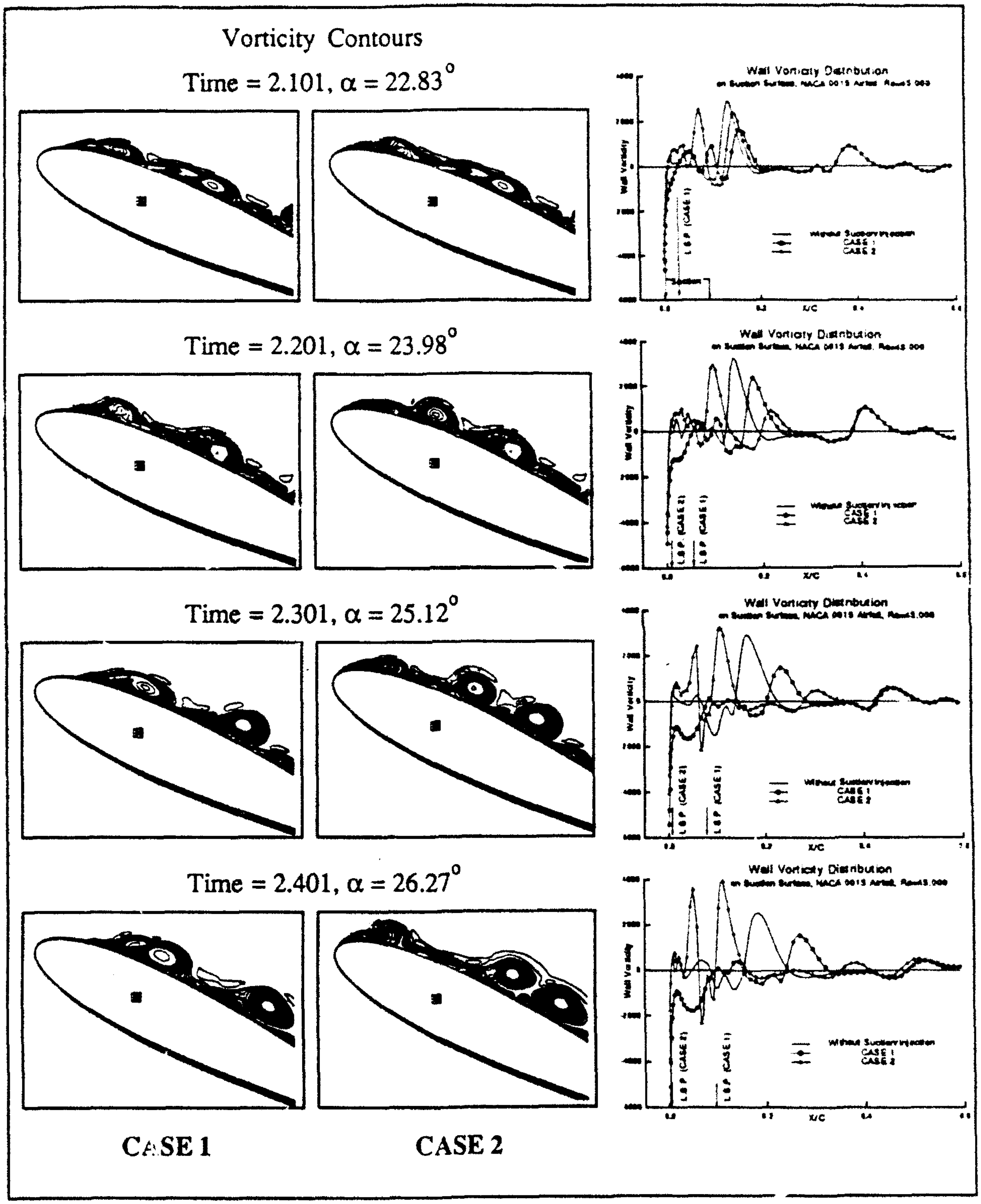

Figure A.23: Effect of suction/injection for NACA 0015 airfoil; Re= 45,000, and $\dot{\alpha}^+ = 0.2$ - instantaneous vorticity contours and wall vorticity. (i) CASE 1: $v_s/U_\infty = 0.045$, (ii) CASE 2: $v_s/U_\infty = 0.035$.

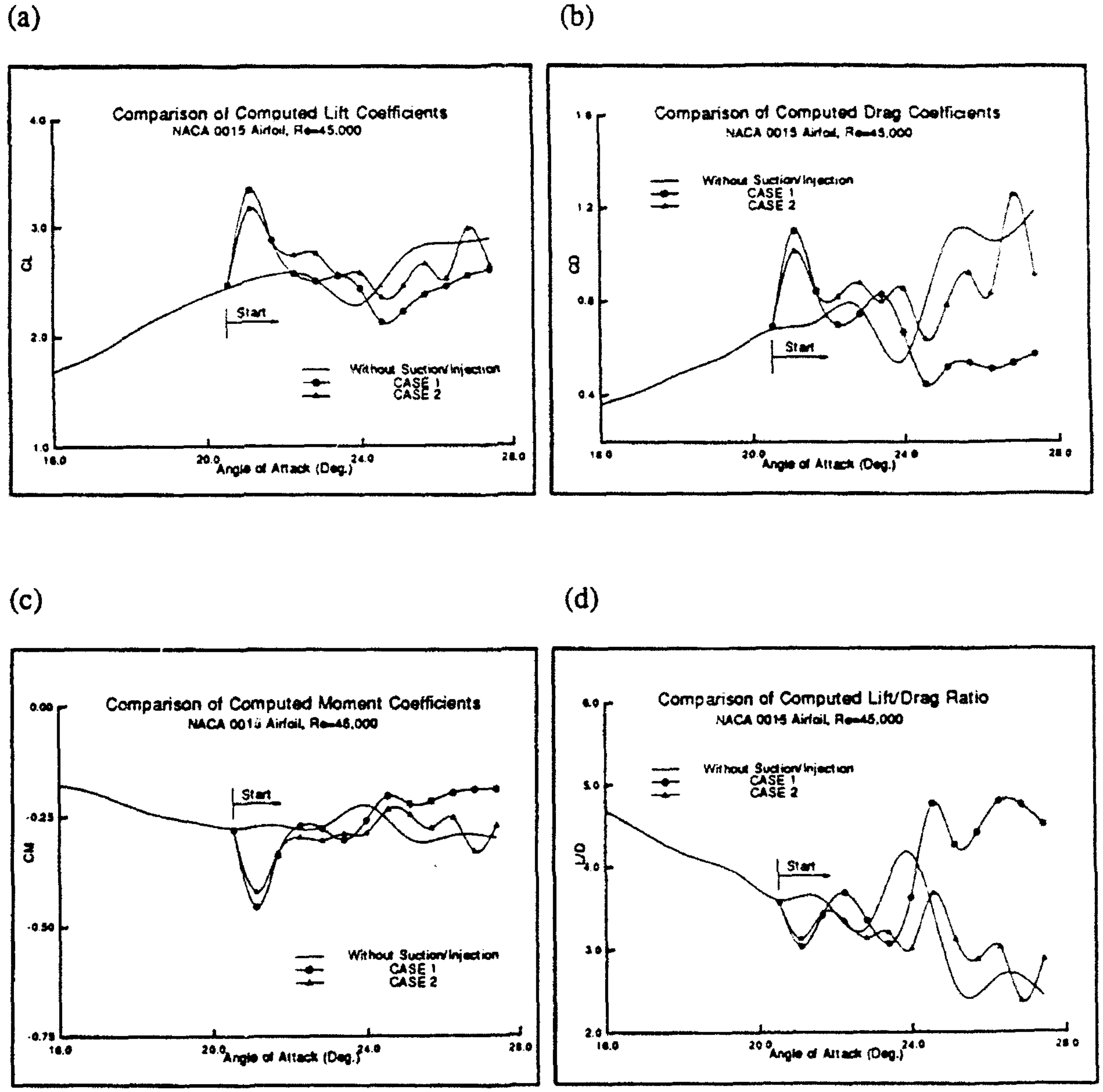

Figure A.24: Effect of suction/injection for NACA 0015 airfoil; Re= 45,000, and $\dot{\alpha}^+ = 0.2$ - C_L, C_D, C_M and L_D. (i) CASE 1: $v_s/U_\infty = 0.045$, (ii) CASE 2: $v_s/U_\infty = 0.035$.

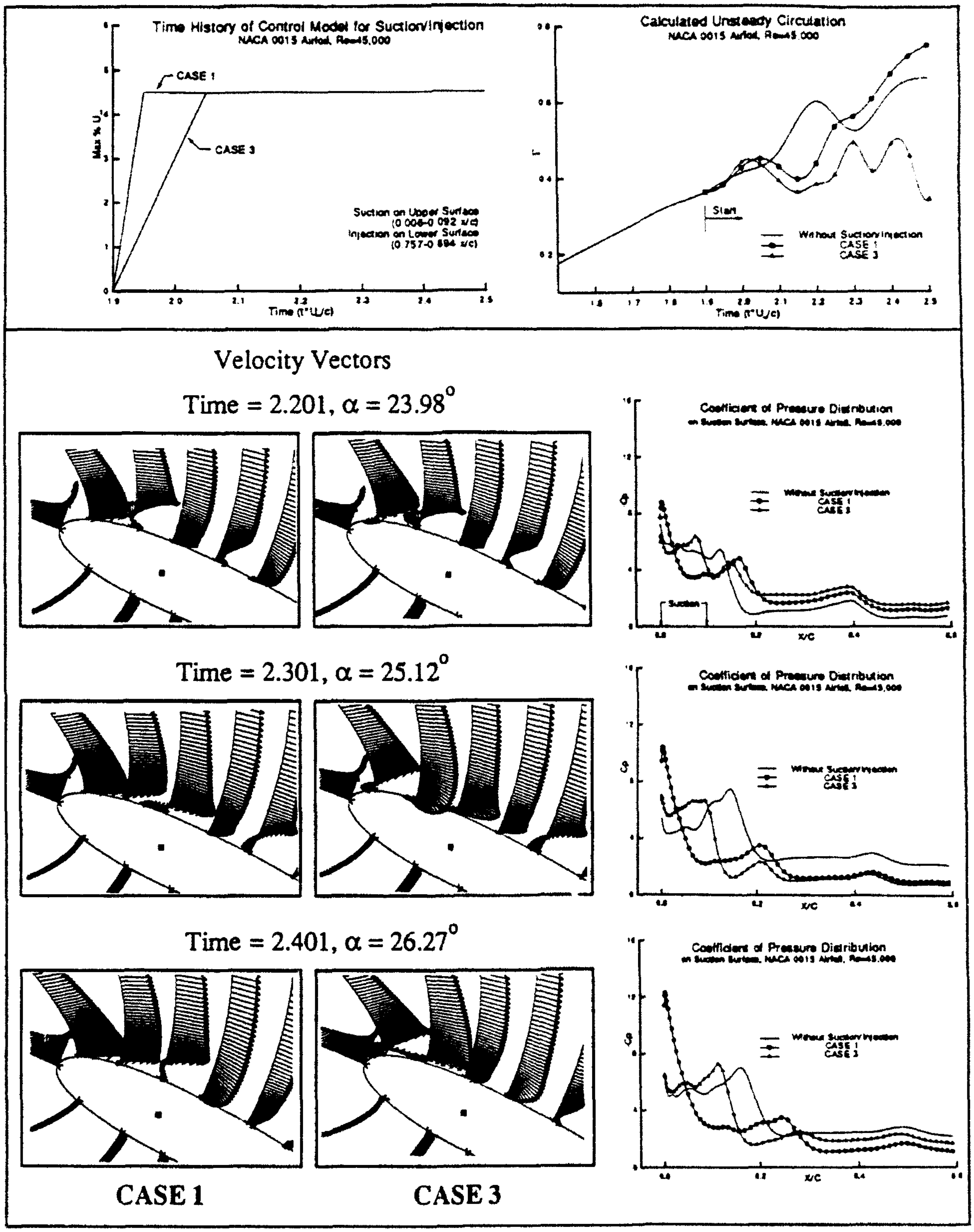

Figure A.25: Effect of suction/injection for NACA 0015 airfoil; Re= 45,000, $\dot{\alpha}^+ = 0.2$ and $v_s/U_\infty = 0.045$ - unsteady circulation, velocity vectors and C_P - distribution. (i) CASE 1: $t_o = 0.05$, (ii) CASE 3: $t_o = 0.15$.

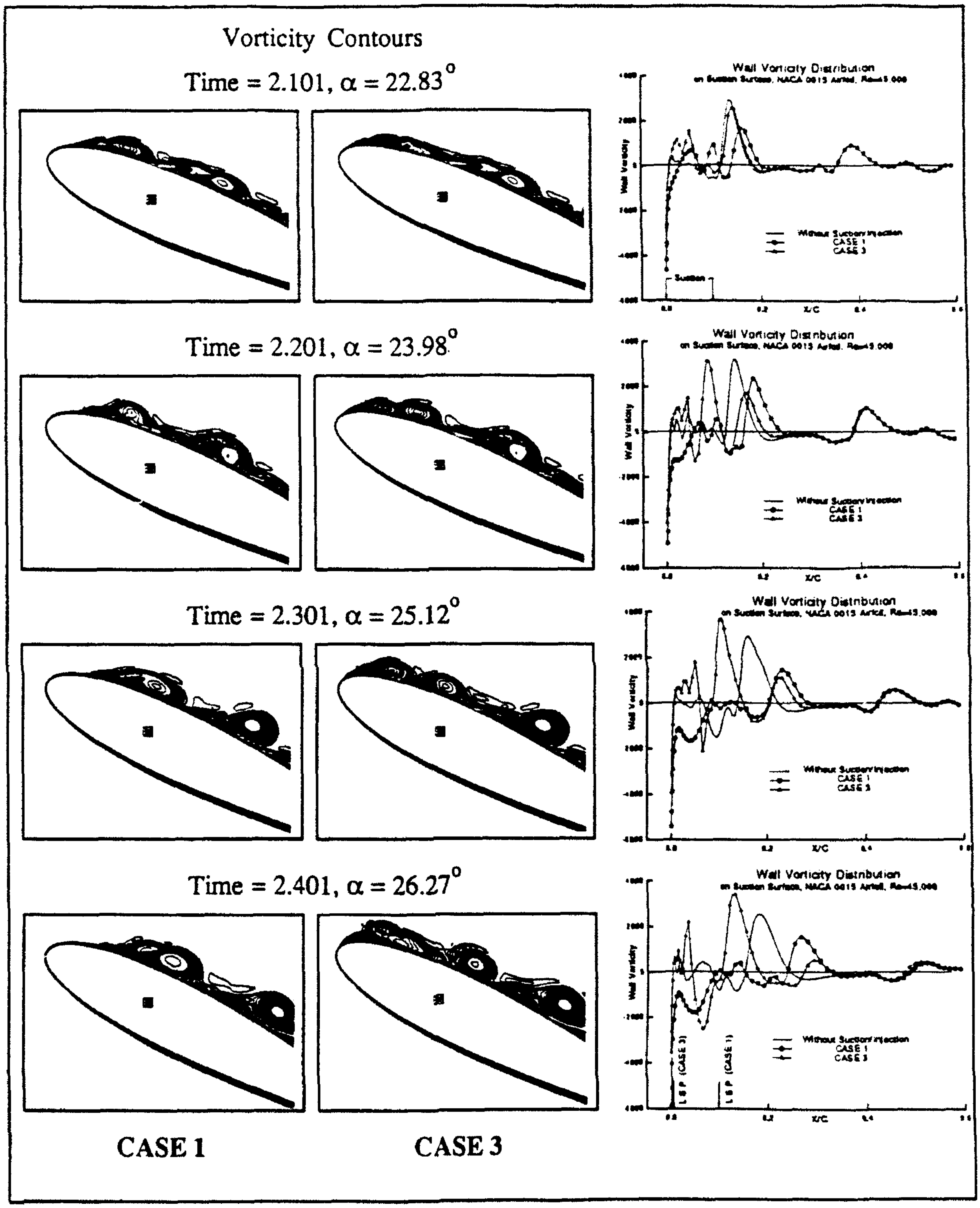

Figure A.26: Effect of suction/injection for NACA 0015 airfoil; Re= 45,000, $\dot{\alpha}^+ = 0.2$ and $v_s/U_\infty = 0.045$ - instantaneous vorticity contours and wall vorticity. (i) CASE 1: $t_o = 0.05$, (ii) CASE 3: $t_o = 0.15$.

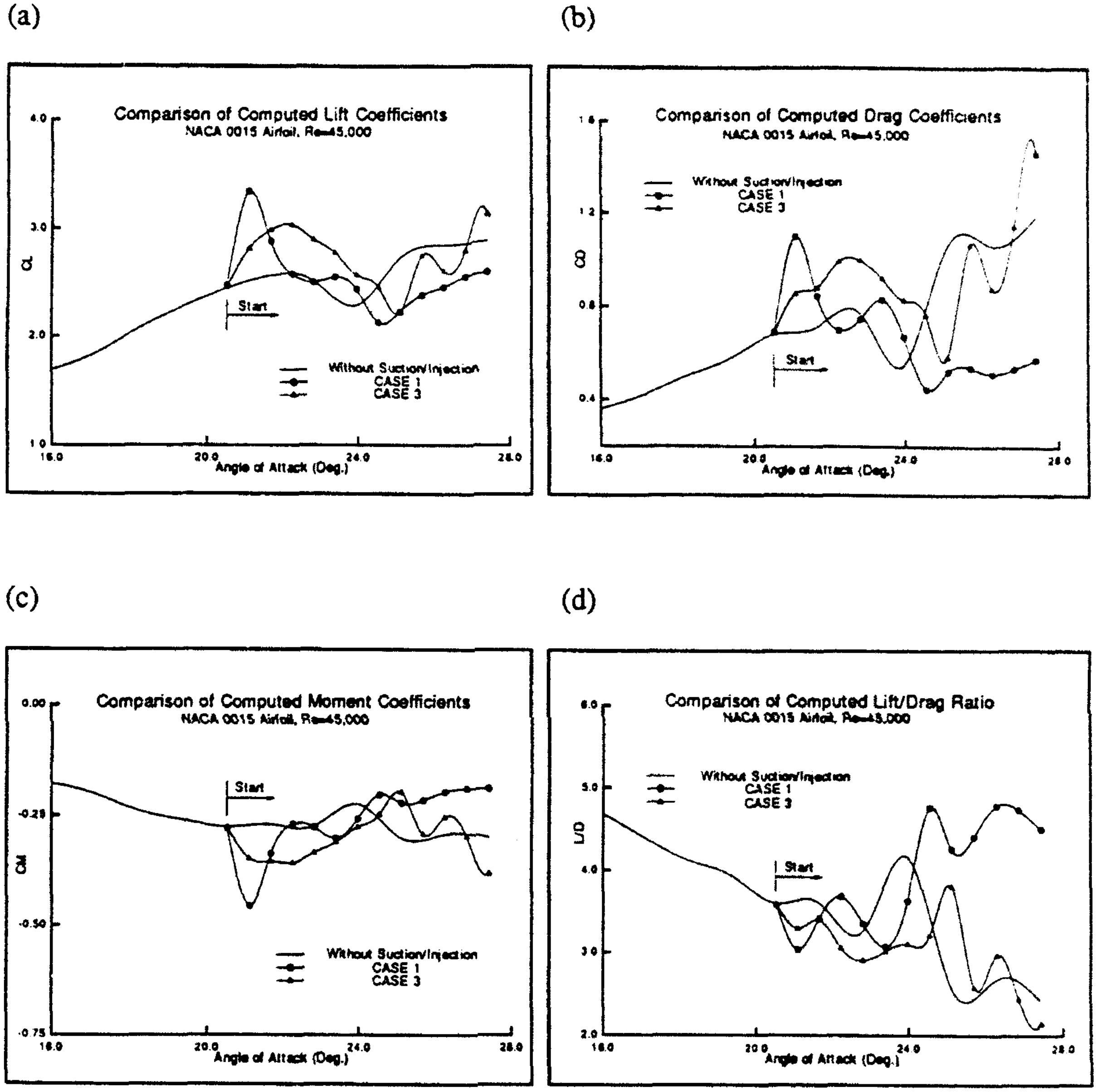

Figure A.27: Effect of suction/injection for NACA 0015 airfoil; Re= 45,000, $\dot{\alpha}^+ = 0.2$ and $v_s/U_\infty = 0.045$ - C_L, C_D, C_M and L_D. (i) CASE 1: $t_o = 0.05$, (ii) CASE 3: $t_o = 0.15$.

Appendix B

Tables & Figures for Section 2.B

Grid Method	25x25x25	33x33x33	49x49x49
MG-DGS	0.4	0.9	2.5
BGE	32	135	1000

Table B.1: Storage requirement in megawords for MG-DGS and BGE methods for velocity problem

U - Uniform Grid   C - Clustered Grid

	25x25x25		33x33x33		49x49x49
	U	C	U	C	U
$\text{CPU}^{*}_{\text{sec}}$	.39	.58	1.04	1.31	2.64
WU	12.8	20.1	16.2	20.7	13.5
μ	.41	.57	.48	.58	.42

* On CRAY Y-MP

Table B.2: Some results for model problem using MG-DGS method

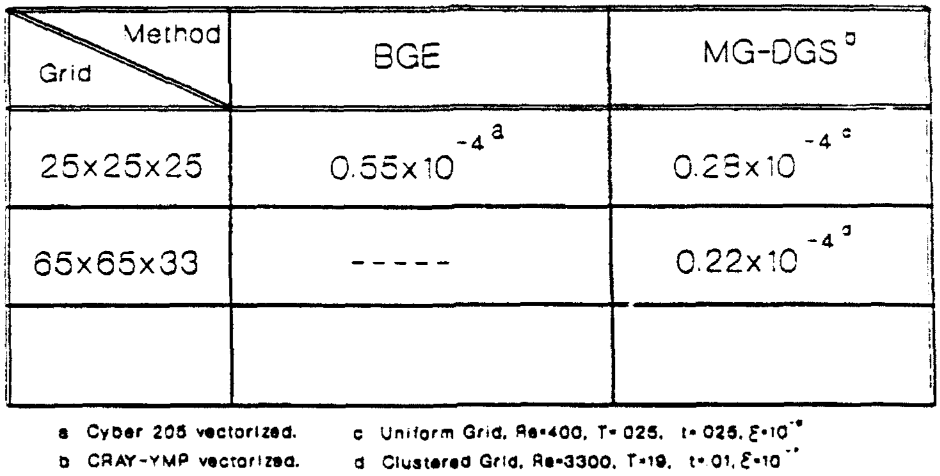

Method / Grid	BGE	MG-DGS[b]
25x25x25	0.55×10^{-4}[a]	0.28×10^{-4}[c]
65x65x33	-----	0.22×10^{-4}[d]

a Cyber 205 vectorized.
b CRAY-YMP vectorized.
c Uniform Grid, Re=400, T=025, t=025, $\varepsilon=10^{-[illegible]}$
d Clustered Grid, Re=3300, T=19, t=.01, $\varepsilon=10^{-[illegible]}$

Table B.3: Comparison of CPU time (sec/per grid/per time step) for BGE and MG-DGS methods for cavity flow problem

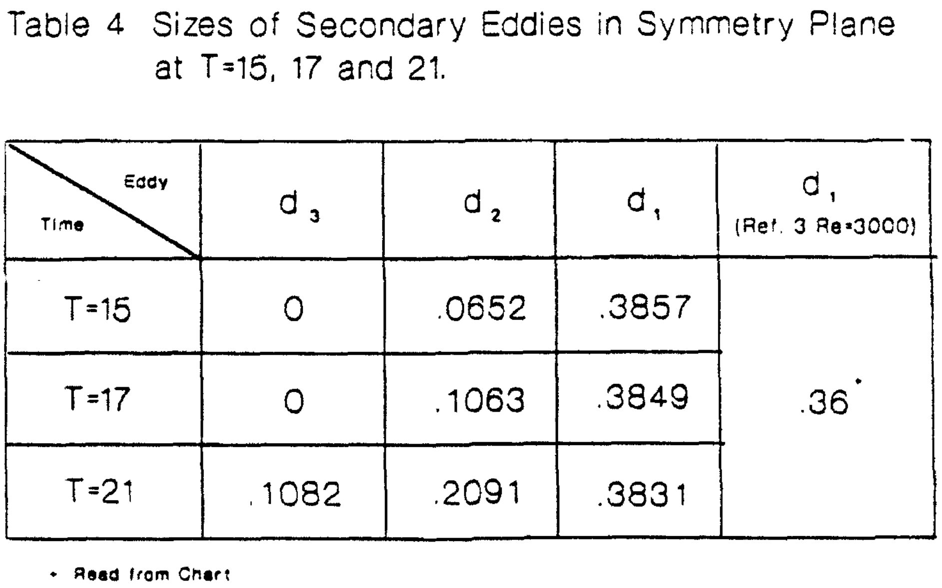

Table 4 Sizes of Secondary Eddies in Symmetry Plane at T=15, 17 and 21.

Eddy / Time	d_3	d_2	d_1	d_1 (Ref. 3 Re=3000)
T=15	0	.0652	.3857	.36*
T=17	0	.1063	.3849	
T=21	.1082	.2091	.3831	

* Read from Chart

Table B.4: Sizes of secondary eddies in symmetry plane at T = 15, 17 and 21

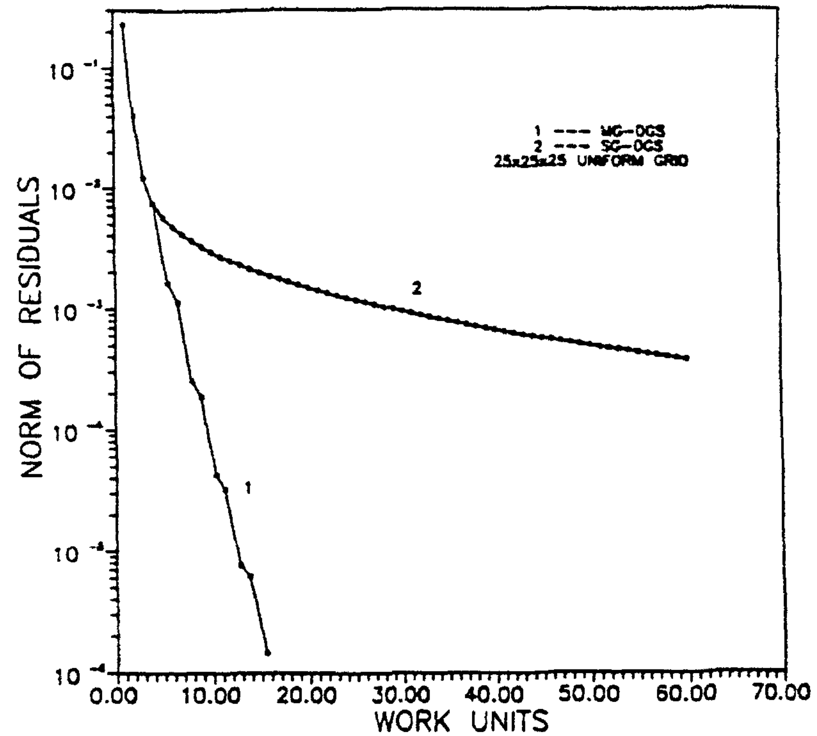

Figure B.1: Convergence history for DGS scheme for model problem using (25 × 25 × 25) uniform grid.

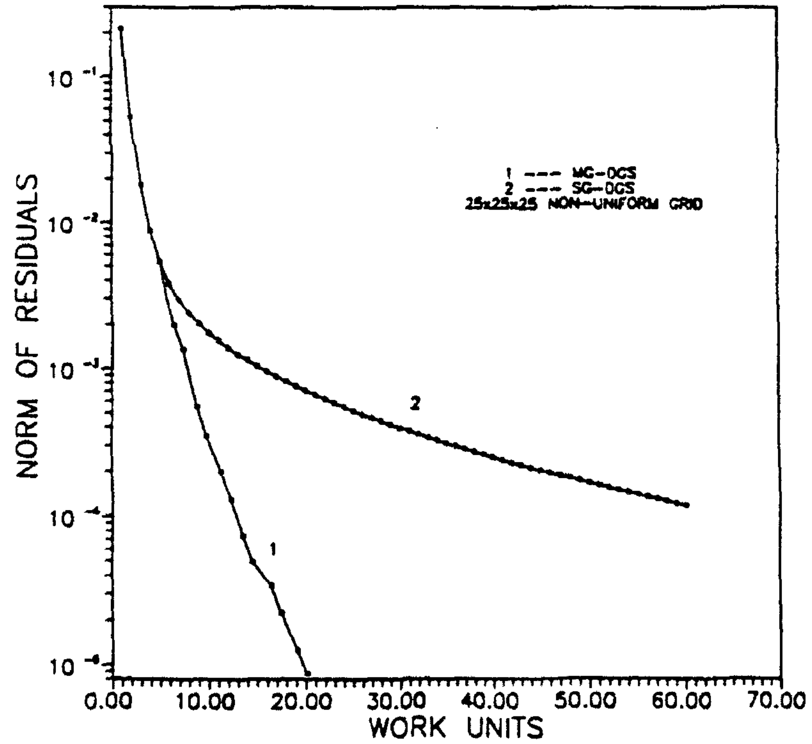

Figure B.2: Convergence history for DGS scheme for model problem using (25 × 25 × 25) moderately clustered grid.

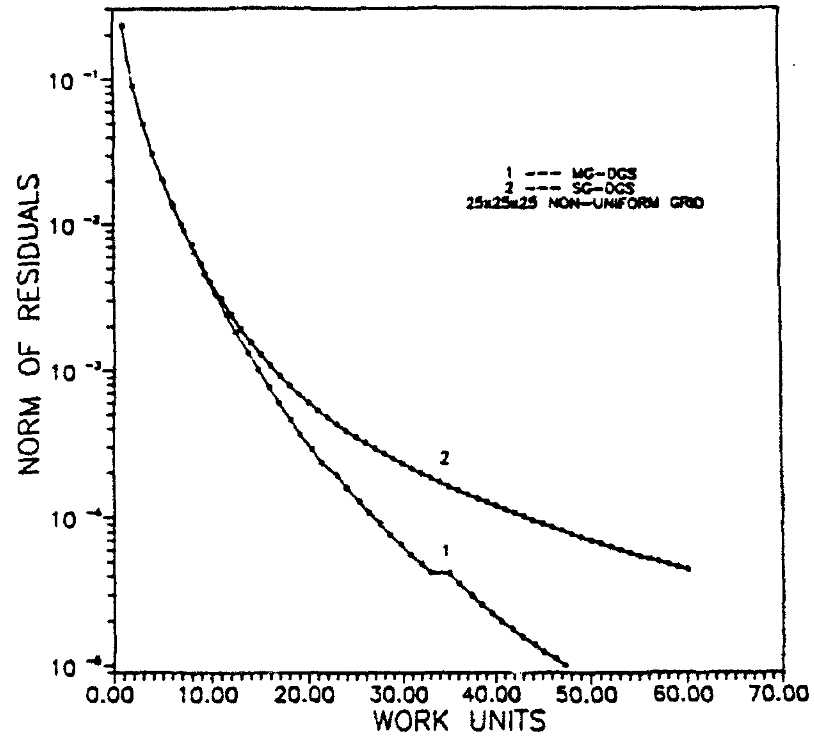

Figure B.3: Convergence history for DGS scheme for model problem using (25 × 25 × 25) strongly clustered grid.

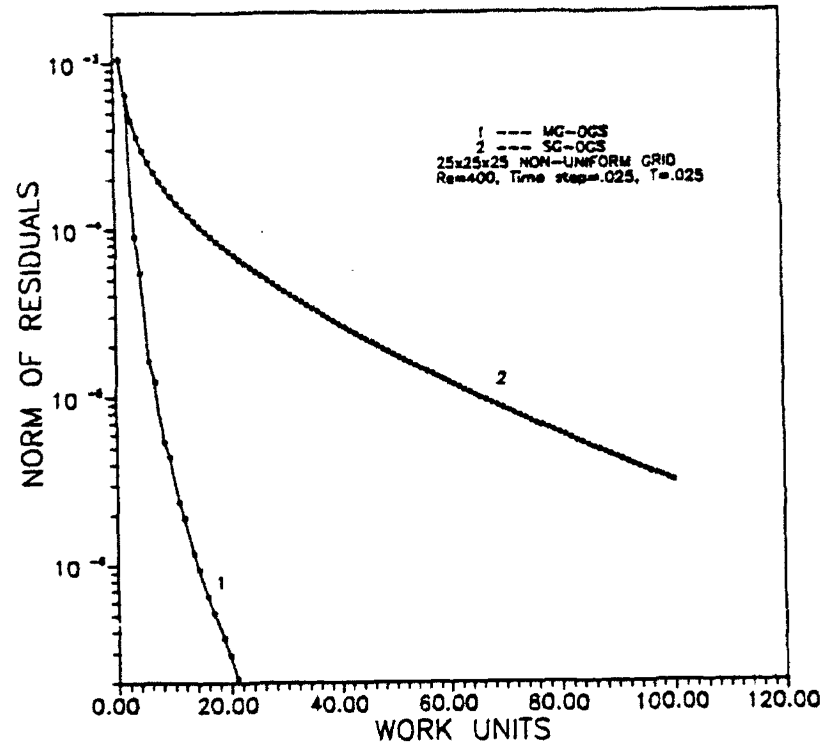

Figure B.4: Convergence history for DGS scheme for velocity solution of shear-driven 3-D cavity flow.

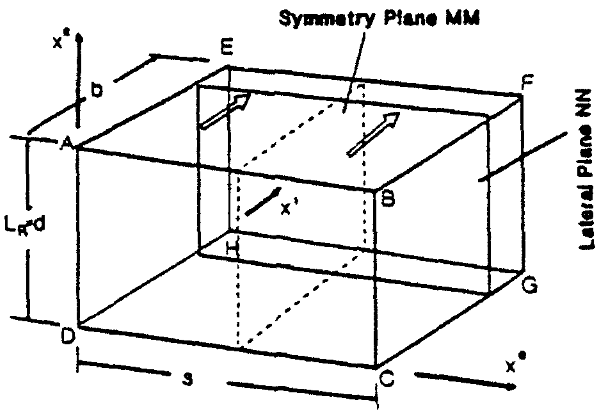

Figure B.5: Configuration of 3-D cavity flow.

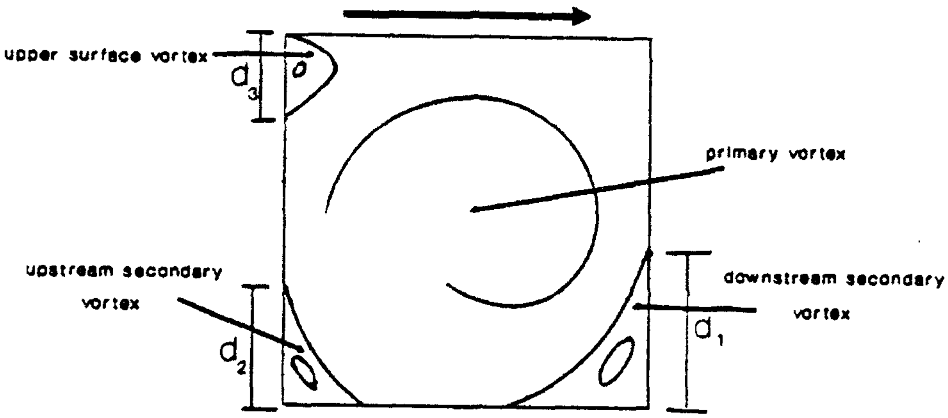

Figure B.6: Flow pattern in symmetry plane MM.

(a)

(b)

Figure B.7: Visualization of Ref. [B.14] for cavity flow (spanwise aspect ratio 3;1); (a) symmetry plane MM; (b) lateral plane NN ($x^1 = 0.8$). Re = 3200, time-averaged.

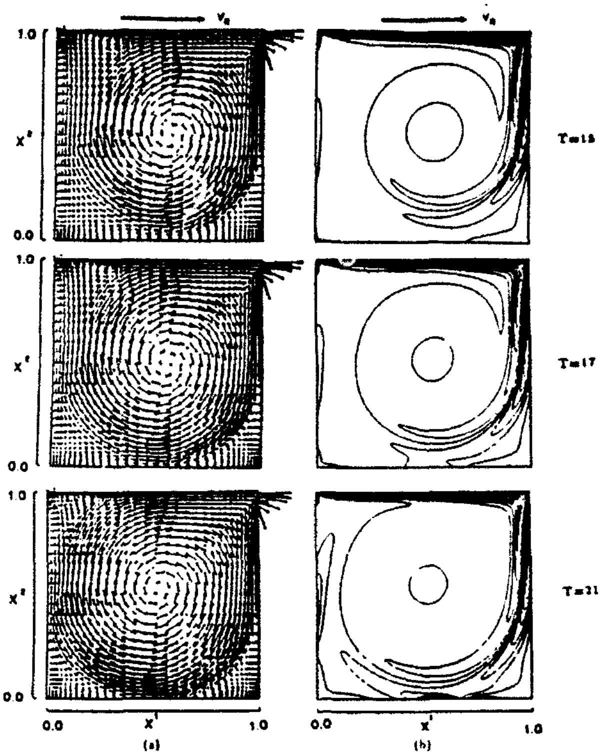

Figure B.8: Simulation results for cavity flow (spanwise aspect ratio 3:1) in symmetry plane MM; (a) velocity vectors; (b) vorticity contours. Re = 3300, T = 15, 17, 21.

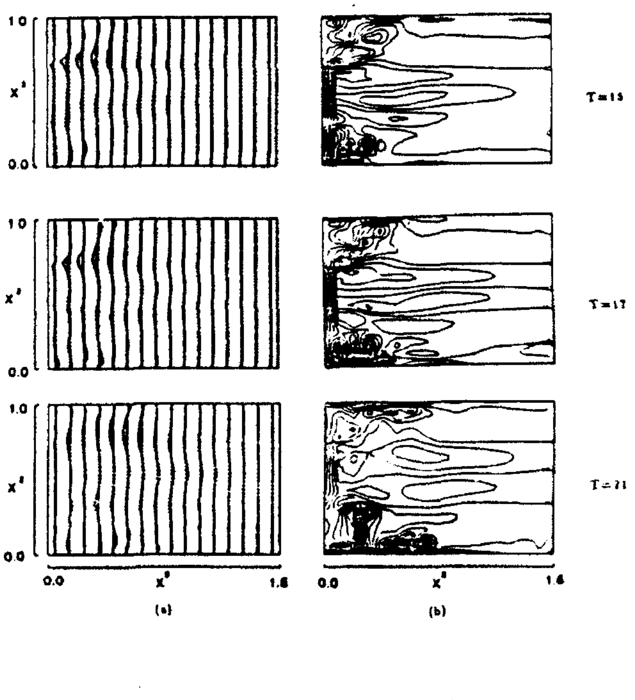

Figure B.9: Simulation results for cavity flow (spanwise aspect ratio 3:1) in lateral plane NN; (a) velocity vectors; (b) vorticity contours. Re = 3300, T = 15, 17, 21.

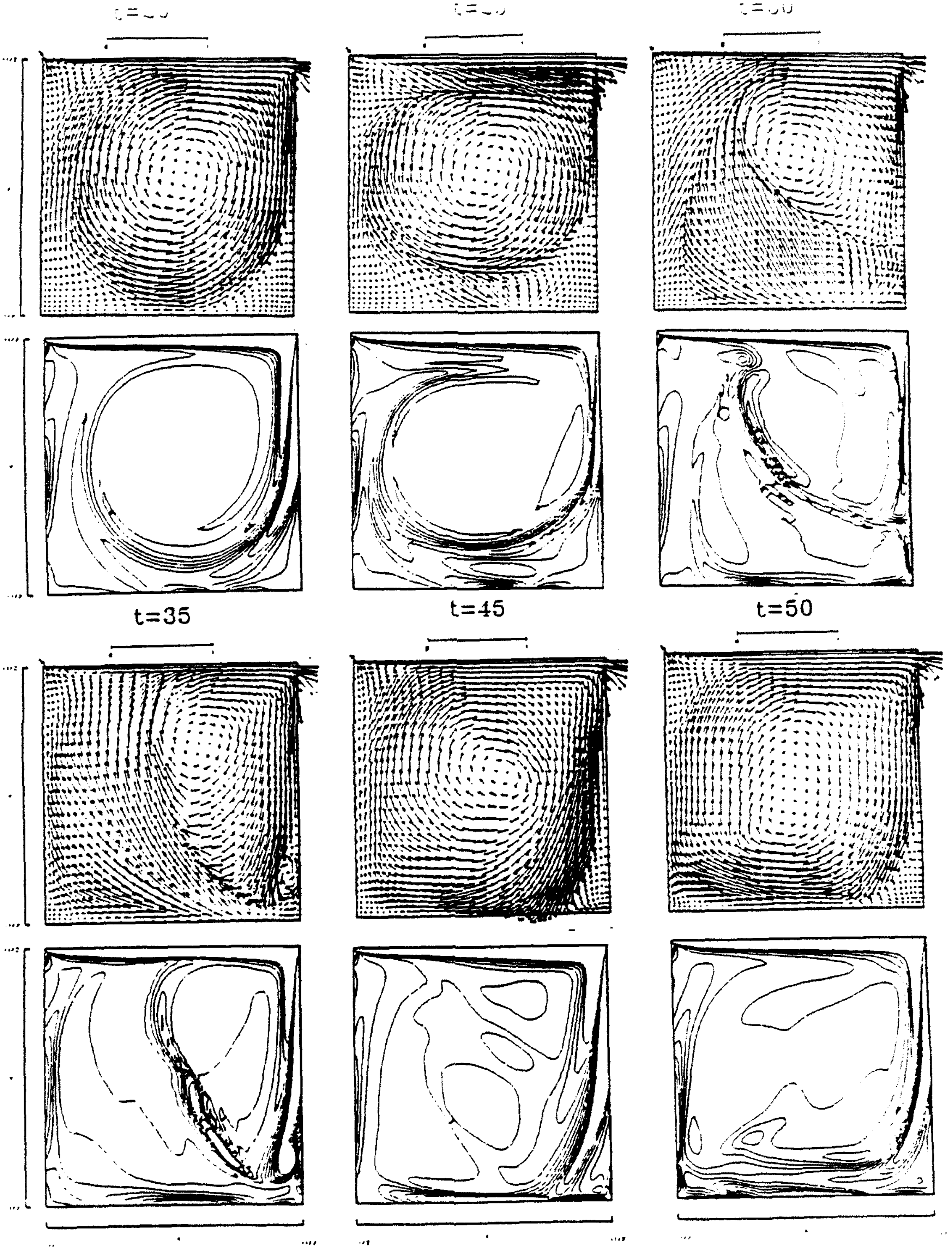

Figure B.10: Tangential velocity vector plots and normal vorticity contour in symmetry plane z = 0 for t = 20, 25, 30, 35, 45, 50.

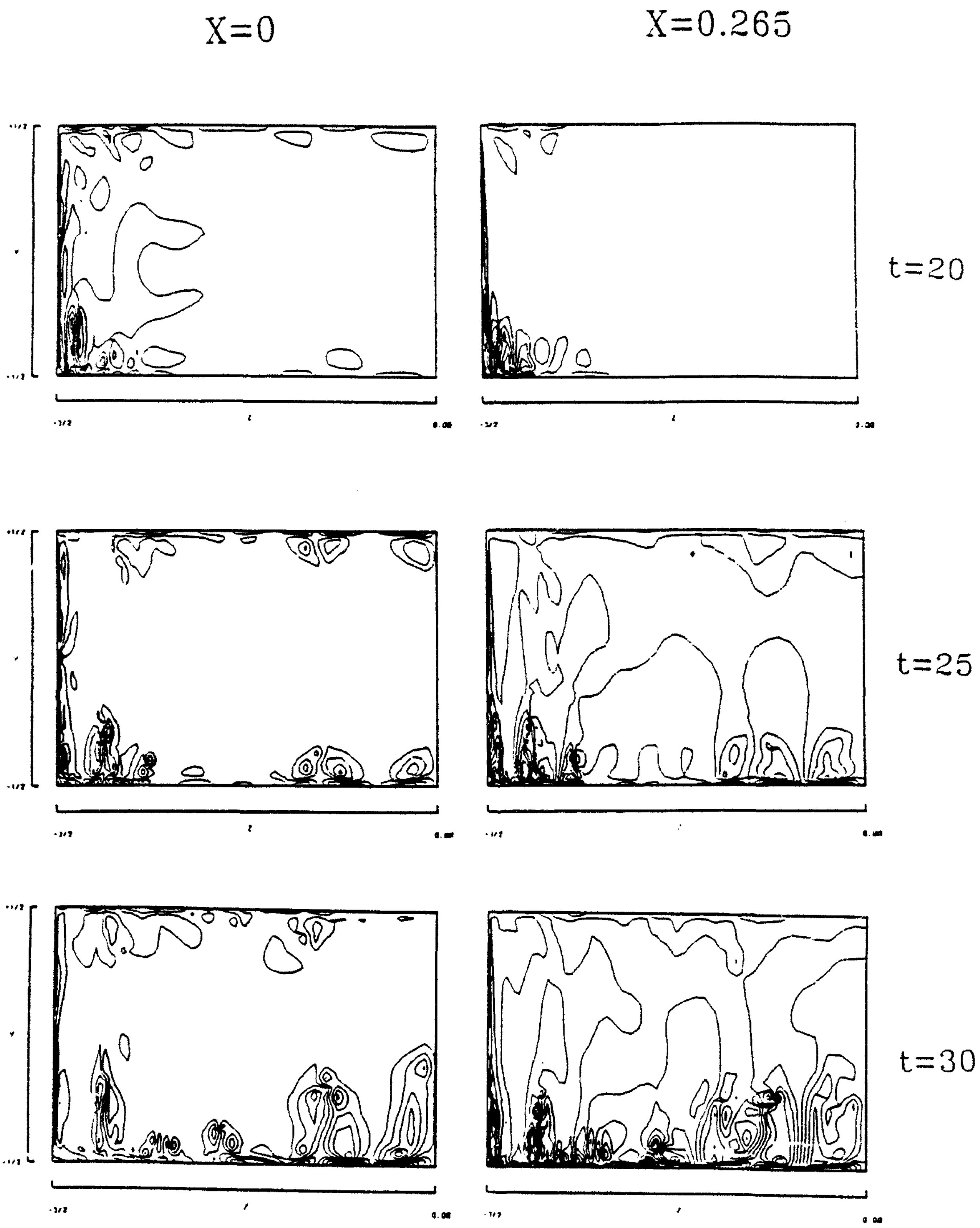

Figure B.11: Normal vorticity contour in vertical spanwise planes x = 0 and x = 0.265 for t = 20, 25, 30, 35, 45, 50.

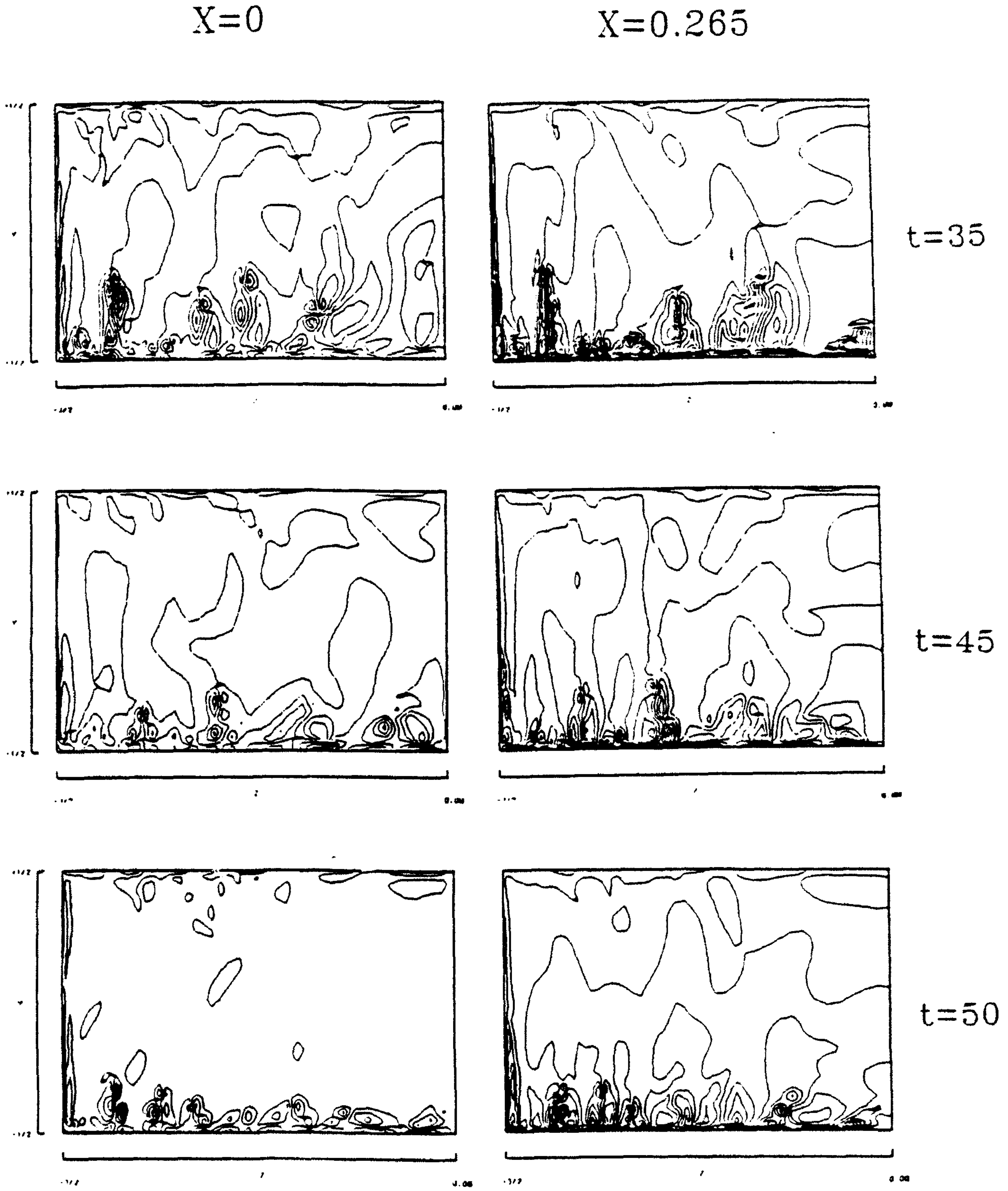

Figure B.12: Normal vorticity contour in vertical spanwise planes (cont'd.) x = 0 and x = 0.265 for t = 20, 25, 30, 35, 45, 50.

Appendix C

Table & Figures for Section 2.C

Source	Reattachment point location Xr
ACR = 0.50, XSL = 2.0	
RE = 500	
Experimental data of Ahmed and Giddens (1983)	≈ 4.5
Present Computation, (300 x 30) Fixed grid	4.2
Present Computation, (300 x 30) Adapted grid	4.45
Present Computation, (100 x 20) Adapted grid	4.2
Present Computation, (50 x 15) Adapted grid	4.0
Re = 750	
Experimental data of Ahmed and Giddens (1983)	≈ 5.5
Present Computation, (300 x 30) Adapted	5.4
Re = 1000	
Experimental data of Ahmed and Giddens (1983)	6.0⁺ (Not well defined)
Present Computation, (300 x 30) Adapted grid	6.9
Present Computation, (100 x 20) Adapted grid	6.7

Table C.1: Comparison of reattachment length. ACR = 0.50, XSL = 2.0

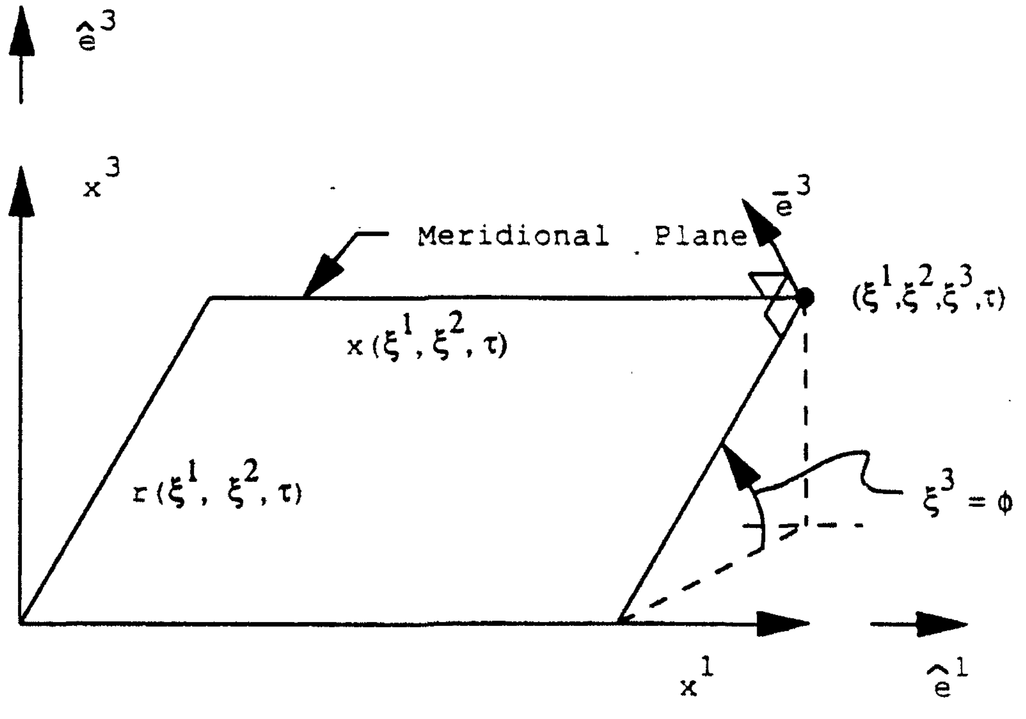

Figure C.1: Generalized axisymmetric coordinate transformation T.

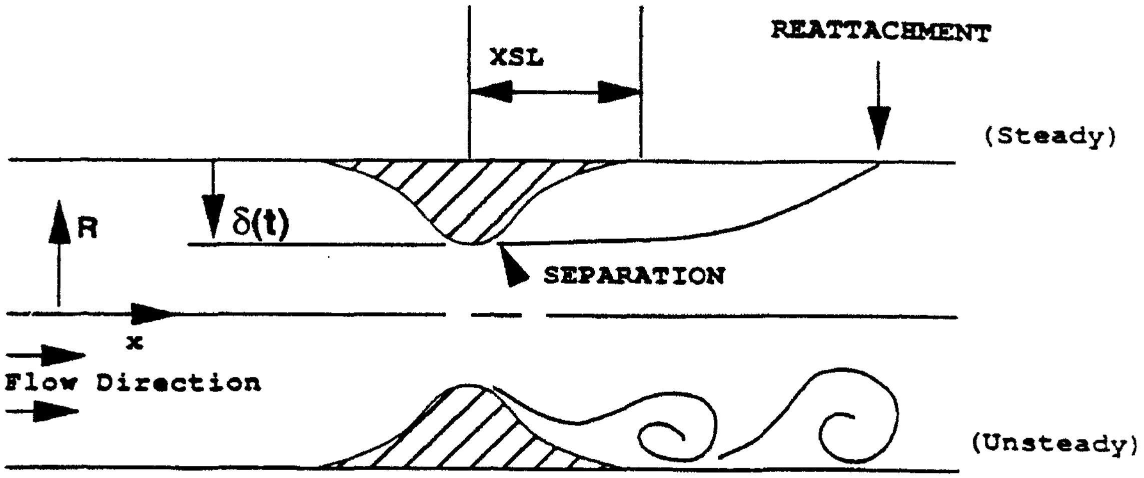

Figure C.2: Schematic of geometric configuration.

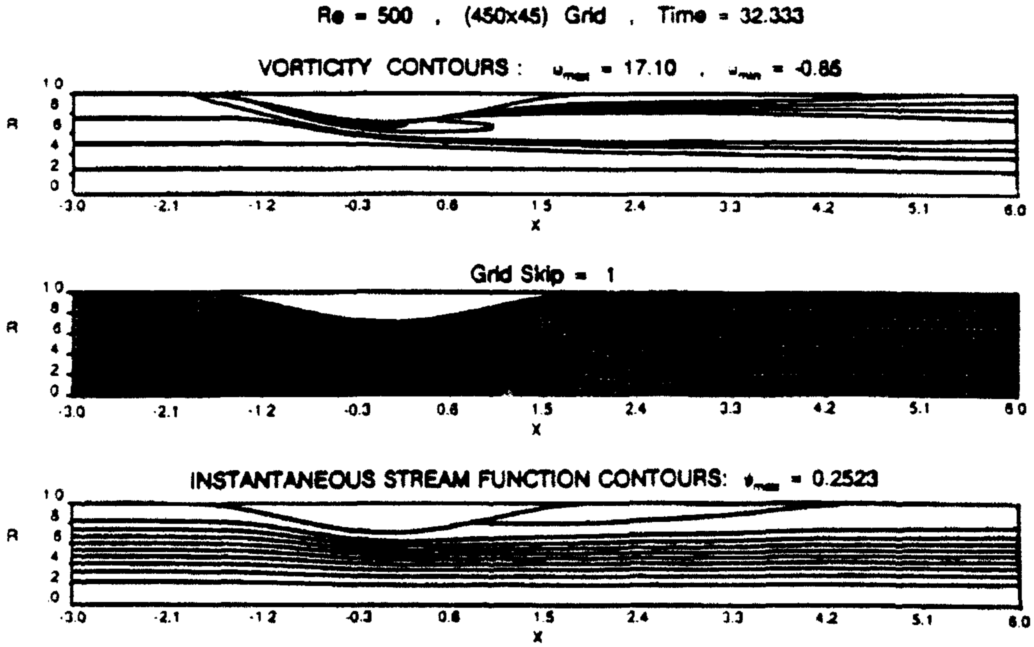

Figure C.3: Steady flow, 50 % constriction by area, XSL = 2.0, (450 × 45) fixed grid, Re = 500.

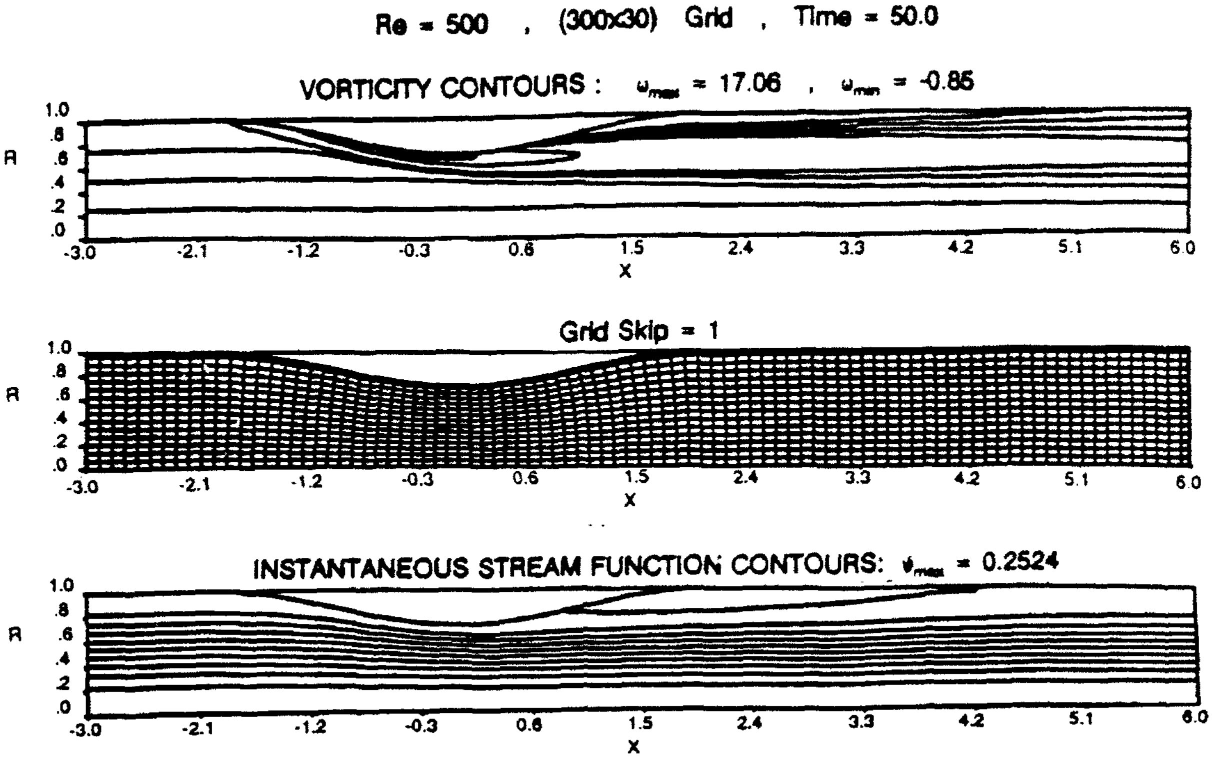

Re = 500 , (300x30) Grid , Time = 50.0

VORTICITY CONTOURS : ω_{max} = 17.06 , ω_{min} = -0.85

Grid Skip = 1

INSTANTANEOUS STREAM FUNCTION CONTOURS: ψ_{max} = 0.2524

Figure C.4: Steady flow, 50 % constriction by area, XSL = 2.0, (300 × 30) fixed grid, Re = 500.

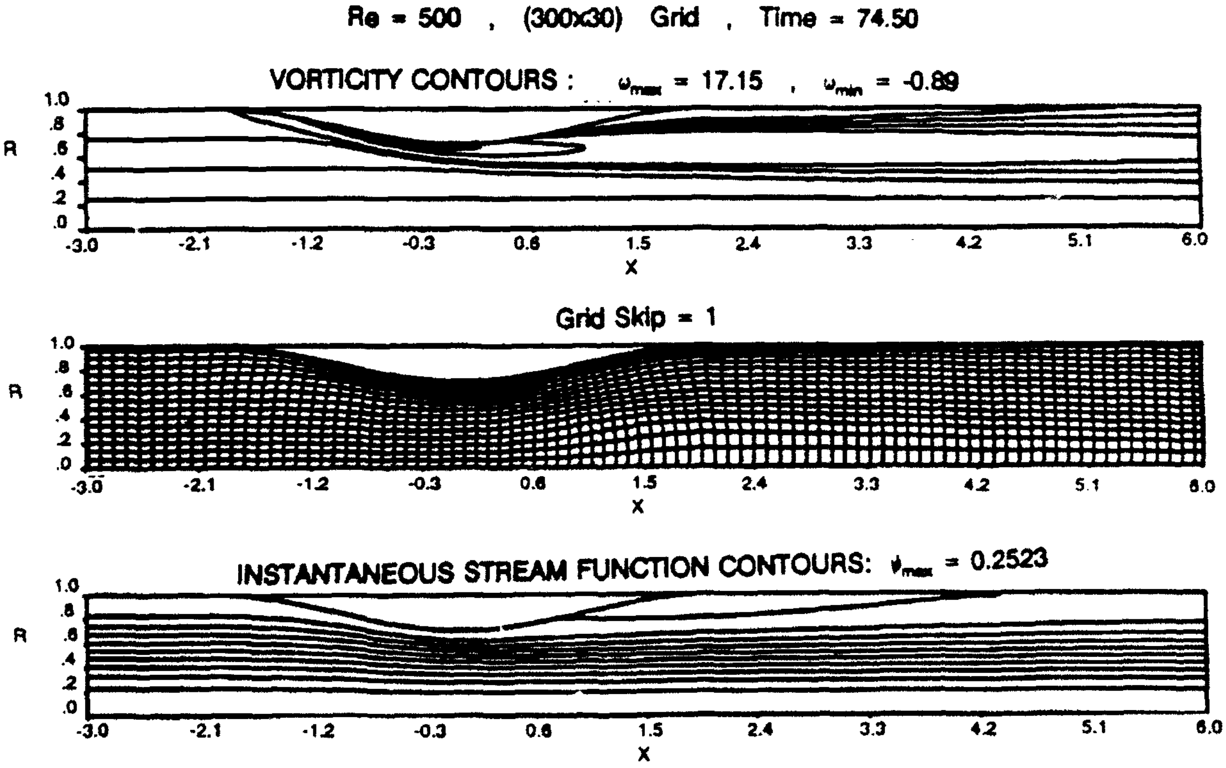

Re = 500 , (300x30) Grid , Time = 74.50

VORTICITY CONTOURS : ω_{max} = 17.15 , ω_{min} = -0.89

Grid Skip = 1

INSTANTANEOUS STREAM FUNCTION CONTOURS: ψ_{max} = 0.2523

Figure C.5: Steady flow, 50 % constriction by area, XSL = 2.0, (300 × 30) adapted grid, Re = 500.

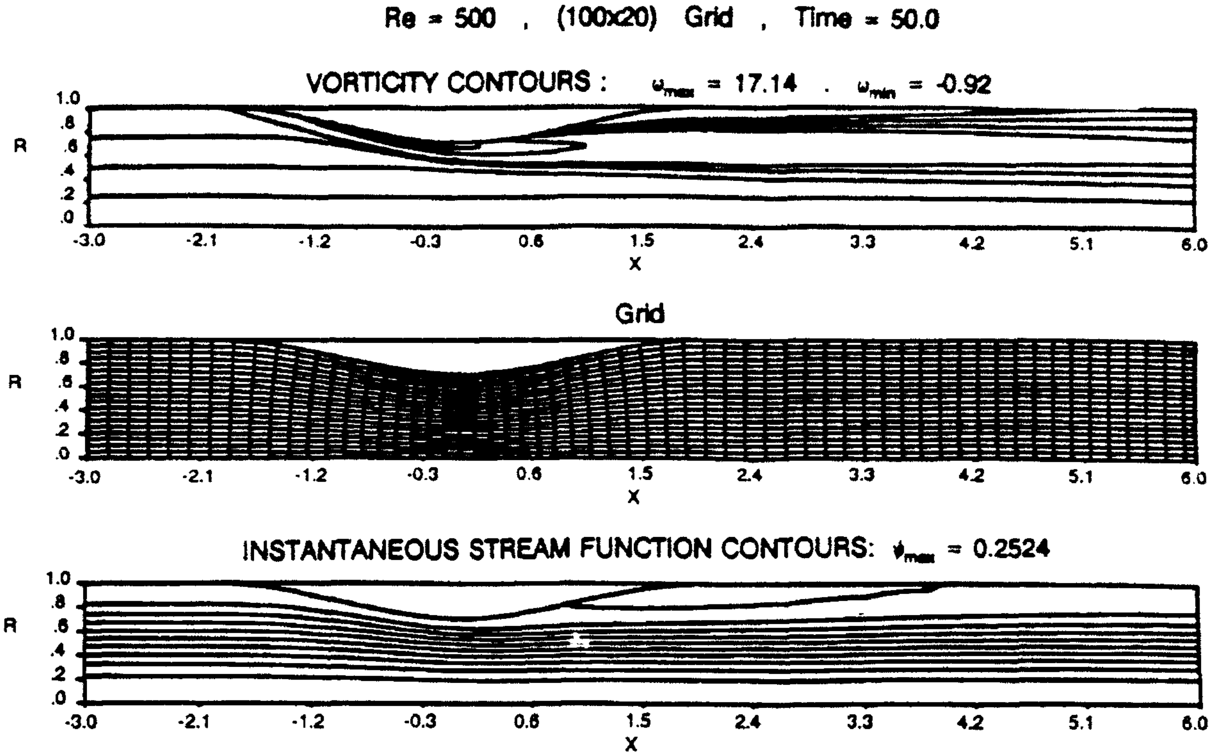
Re = 500 , (100x20) Grid , Time = 50.0

VORTICITY CONTOURS : ω_{max} = 17.14 . ω_{min} = -0.92

Grid

INSTANTANEOUS STREAM FUNCTION CONTOURS: ψ_{max} = 0.2524

Figure C.6: Steady flow, 50 % constriction by area, XSL = 2.0, (100 × 20) fixed grid, Re = 500.

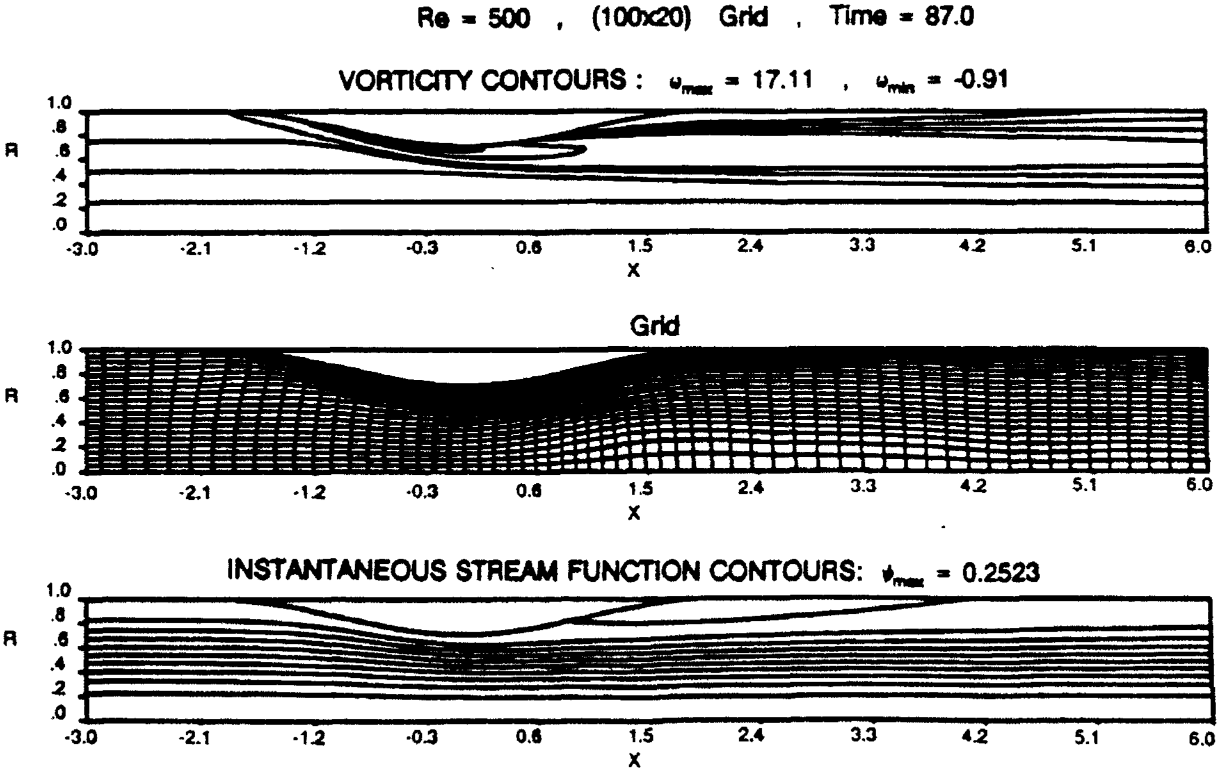
Re = 500 , (100x20) Grid , Time = 87.0

VORTICITY CONTOURS : ω_{max} = 17.11 , ω_{min} = -0.91

Grid

INSTANTANEOUS STREAM FUNCTION CONTOURS: ψ_{max} = 0.2523

Figure C.7: Steady flow, 50 % constriction by area, XSL = 2.0, (100 × 20) adapted grid, Re = 500.

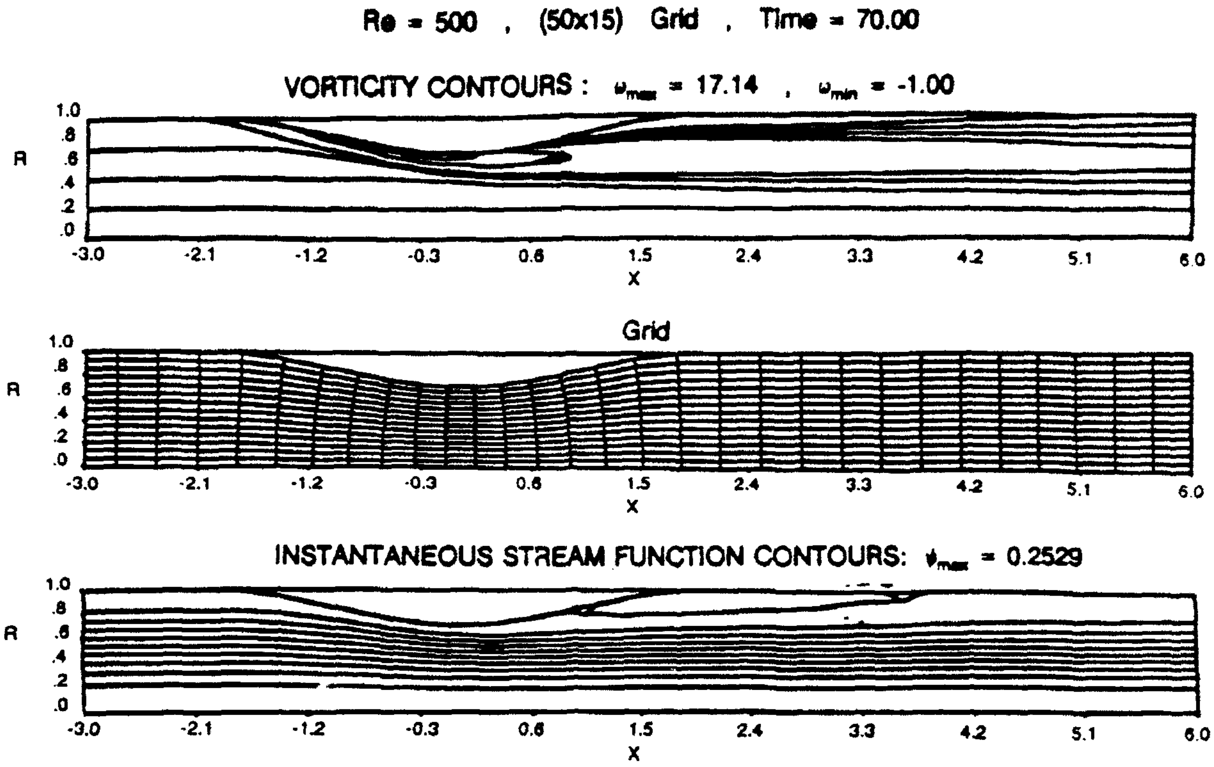
Re = 500 , (50x15) Grid , Time = 70.00

VORTICITY CONTOURS : ω_{max} = 17.14 , ω_{min} = -1.00

Grid

INSTANTANEOUS STREAM FUNCTION CONTOURS: ψ_{max} = 0.2529

Figure C.8: Steady flow, 50 % constriction by area, XSL = 2.0, (50 × 15) fixed grid, Re = 500.

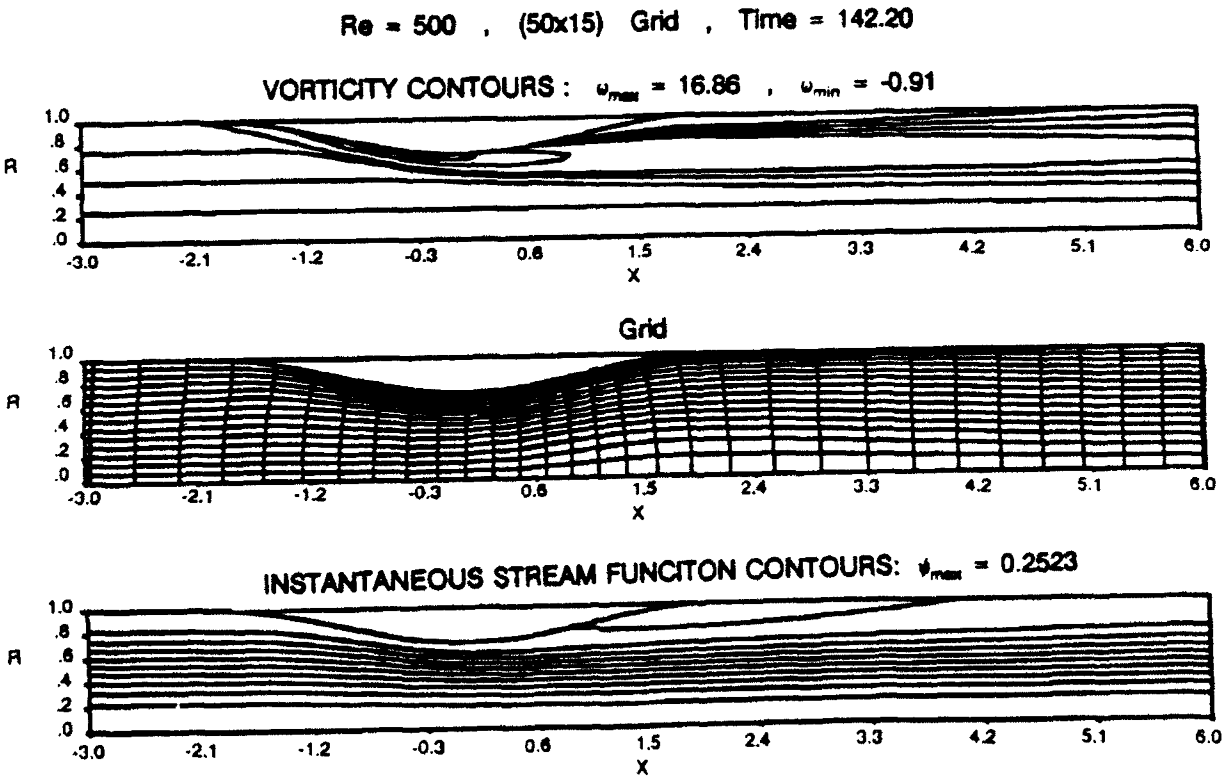
Re = 500 , (50x15) Grid , Time = 142.20

VORTICITY CONTOURS : ω_{max} = 16.86 , ω_{min} = -0.91

Grid

INSTANTANEOUS STREAM FUNCITON CONTOURS: ψ_{max} = 0.2523

Figure C.9: Steady flow, 50 % constriction by area, XSL = 2.0, (50 × 15) adapted grid, Re = 500.

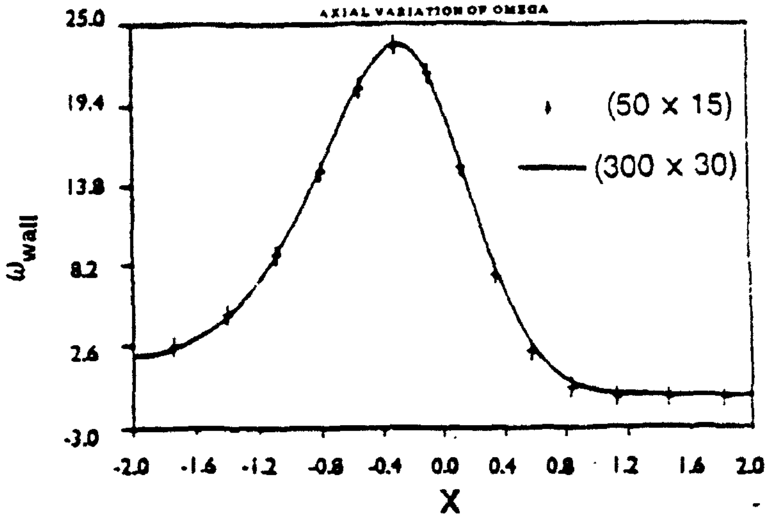

Figure C.10: Axial variation of wall vorticity, steady flow, 50 % constriction by area, Re = 500.

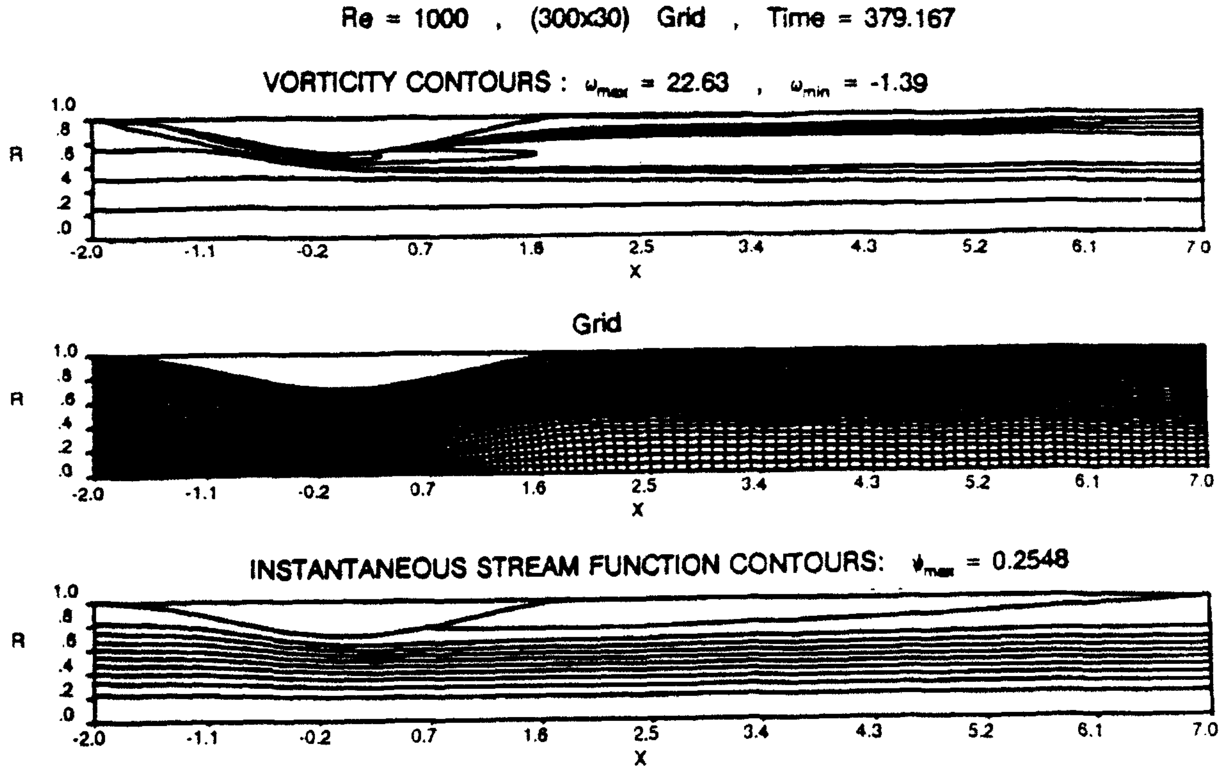

Figure C.11: Steady flow, 50 % constriction by area, XSL = 2.0, (300 × 40) adapted grid, Re = 1000.

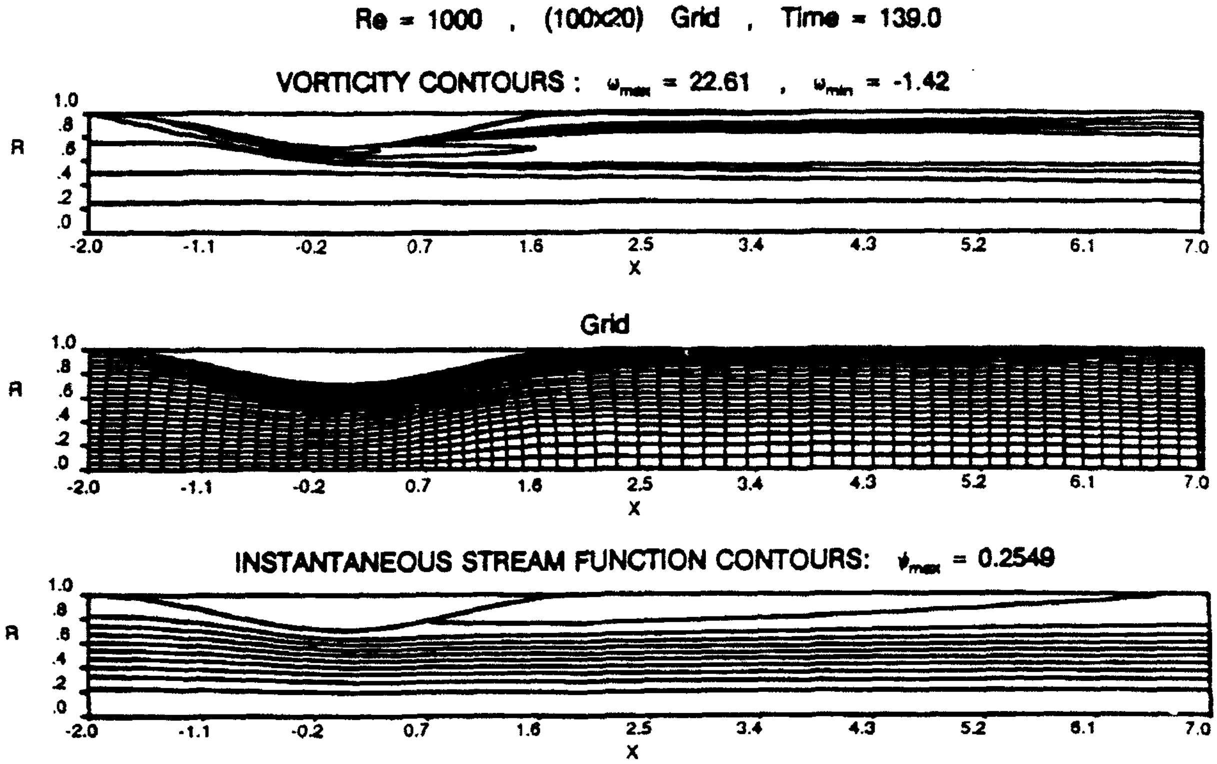

Figure C.12: Steady flow, 50 % constriction by area, XSL = 2.0, (100 × 20) adapted grid, Re = 1000.

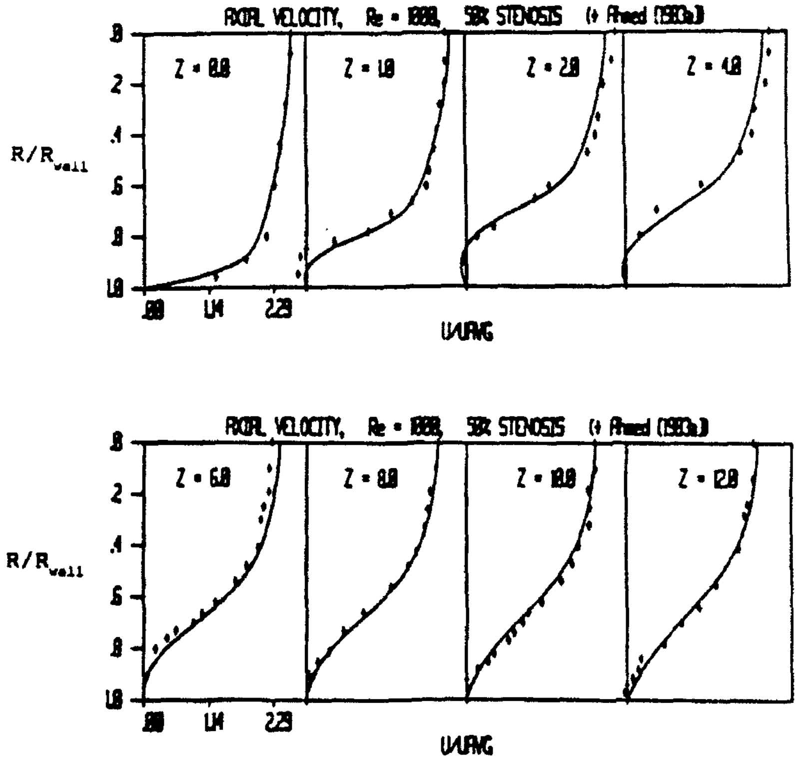

Figure C.13: Axial velocity profiles, 50 % constriction by area, XSL = 2.0, (300 × 30) adapted grid, Re = 1000.

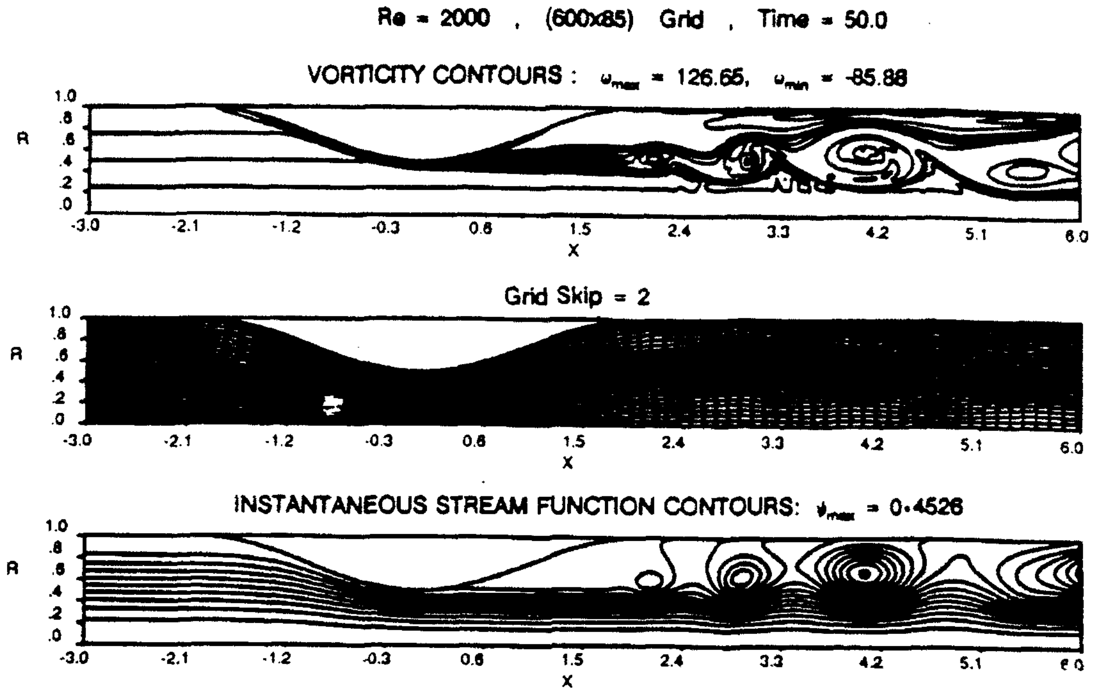

a. τ = 50.0.

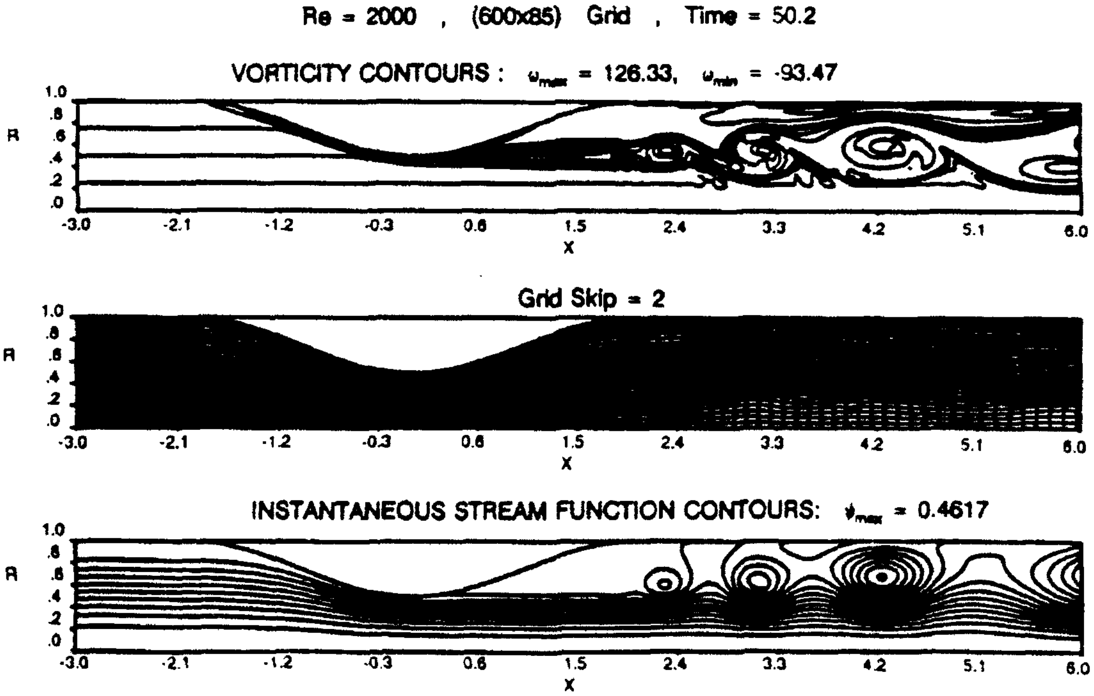

b. τ = 50.2.

Figure C.14: Unsteady flow adaption, throat region, Re = 2000, XSL = 2.0, ACR = 0.75, (600 × 85) grid.

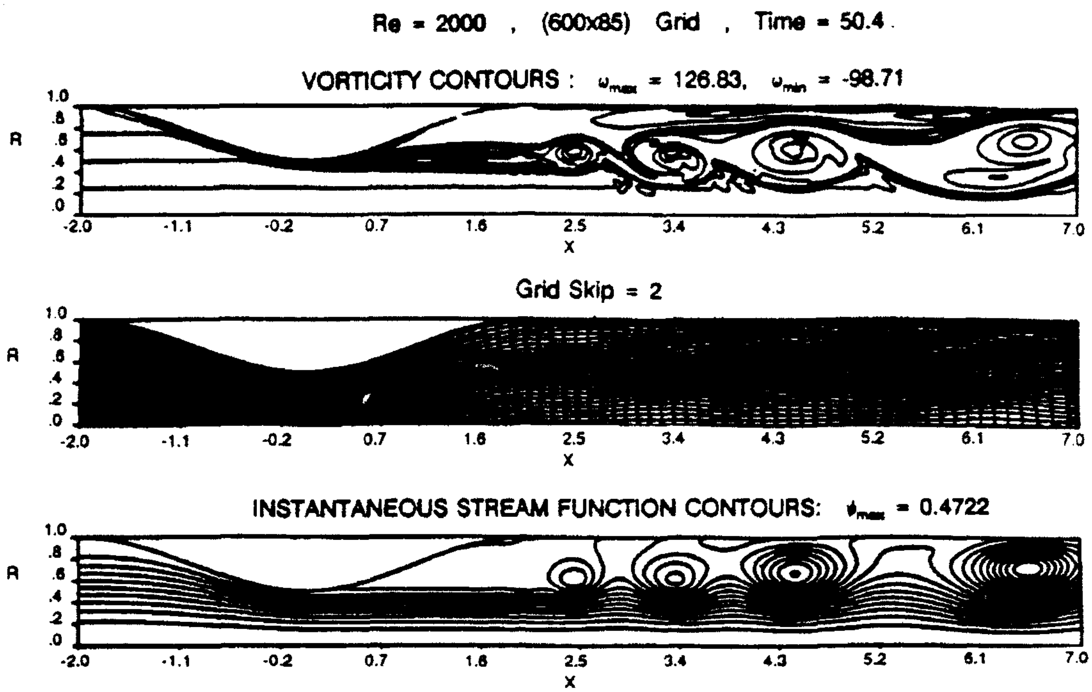
Re = 2000 , (600x85) Grid , Time = 50.4

VORTICITY CONTOURS : ω_{max} = 126.83, ω_{min} = -98.71

Grid Skip = 2

INSTANTANEOUS STREAM FUNCTION CONTOURS: ψ_{max} = 0.4722

c. τ = 50.4.

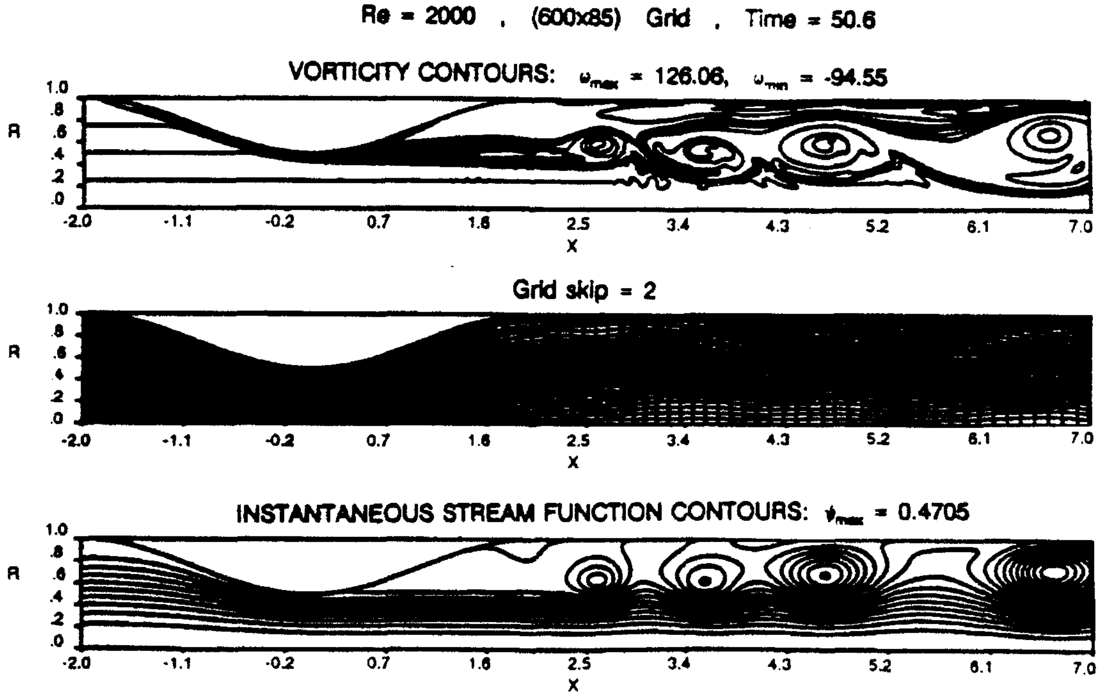
Re = 2000 , (600x85) Grid , Time = 50.6

VORTICITY CONTOURS: ω_{max} = 126.06, ω_{min} = -94.55

Grid skip = 2

INSTANTANEOUS STREAM FUNCTION CONTOURS: ψ_{max} = 0.4705

d. τ = 50.6.

Figure C.14: Continued.

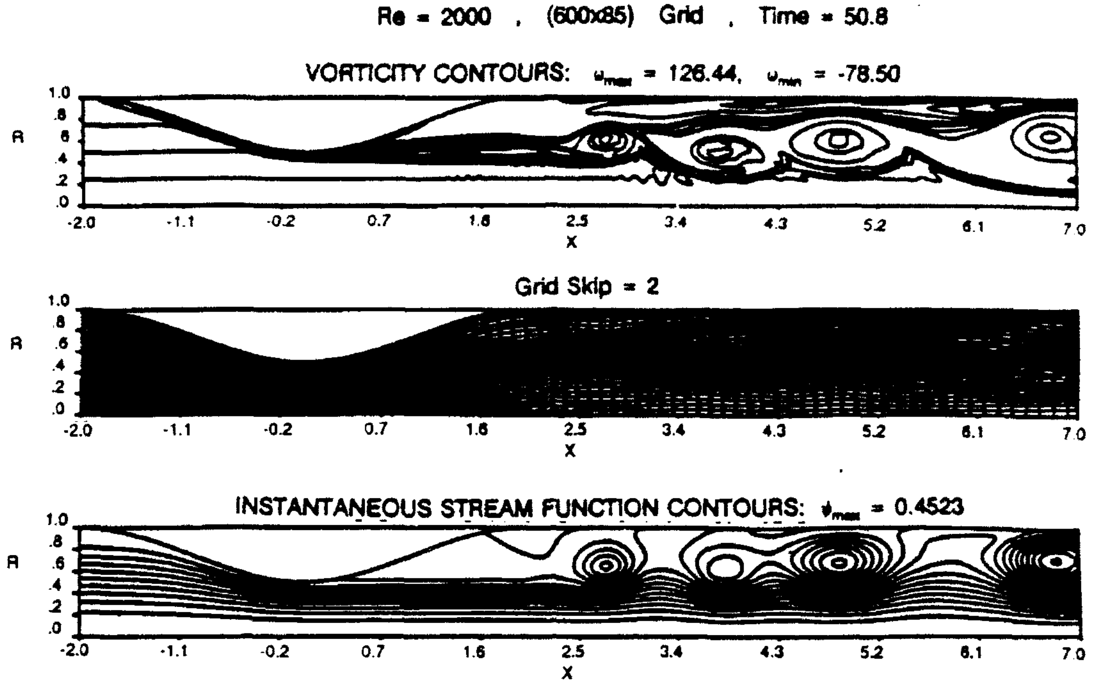

e. τ = 50.8.

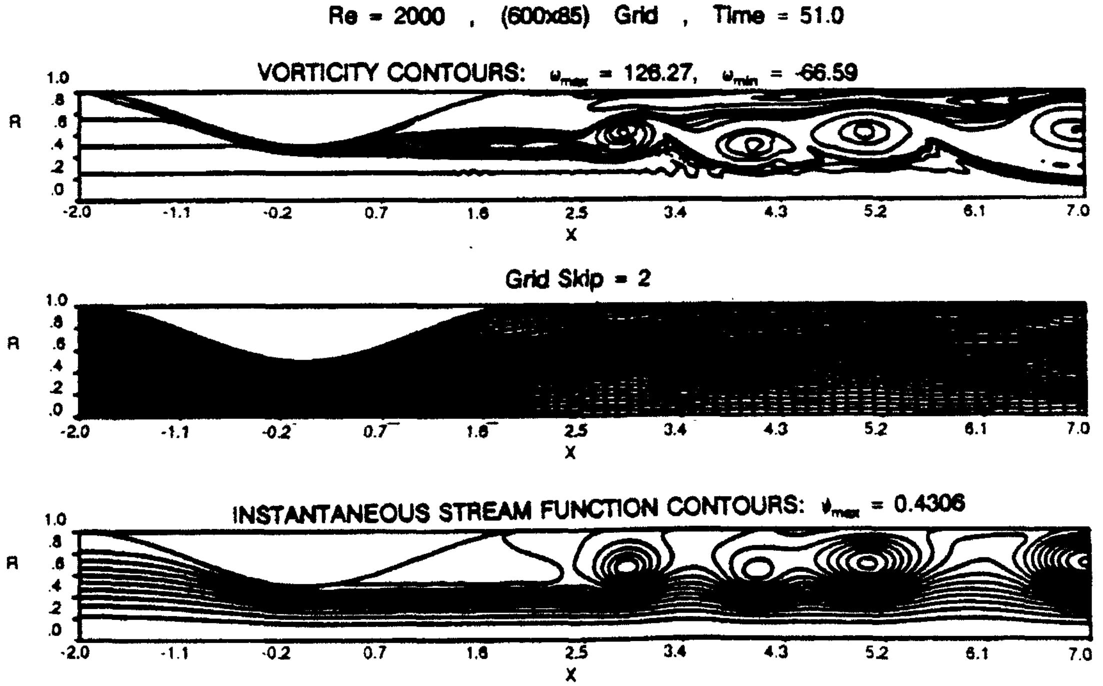

f. τ = 51.0.

Figure C.14: Continued.

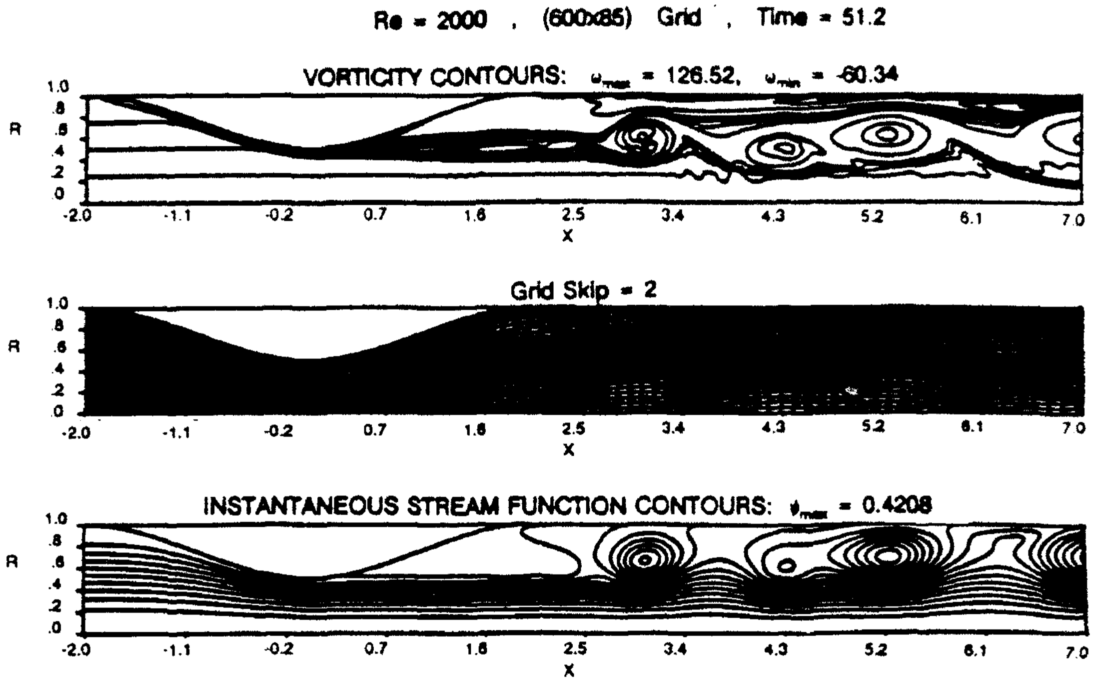

g. τ = 51.2.

Figure C.14: Continued.

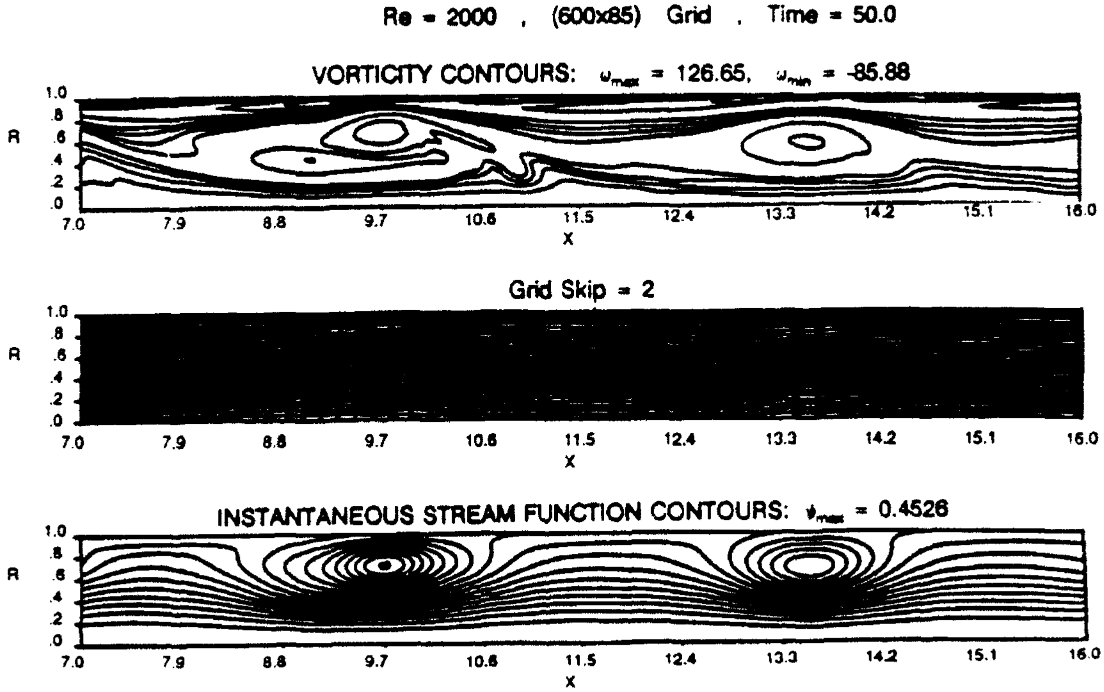

a. τ = 50.0.

Figure C.15: Unsteady flow adaption, downstream region, Re = 2000, XSL = 2.0, ACR = 0.75, (600 × 85) grid.

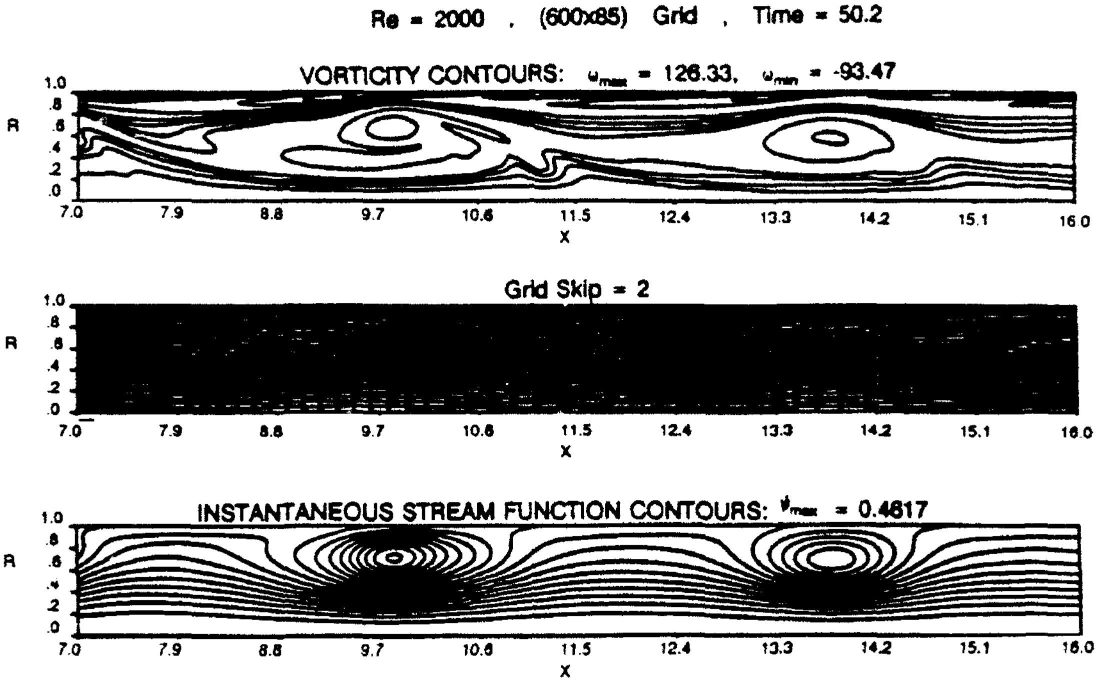

b. τ = 50.2.

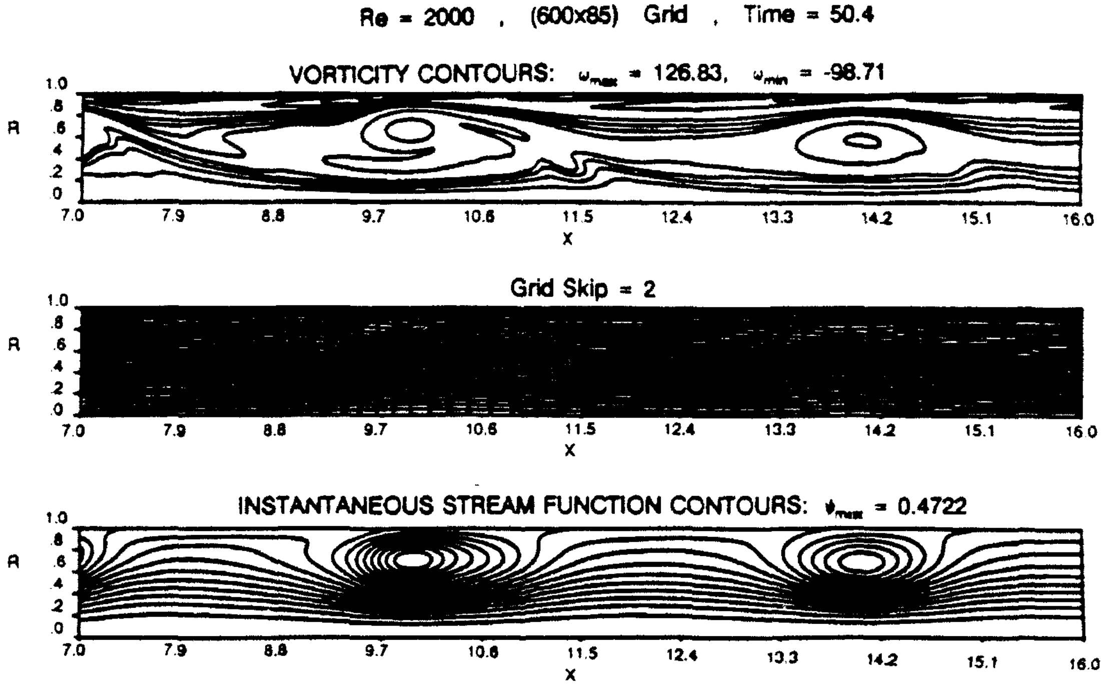

c. τ = 50.4.

Figure C.15: Continued.

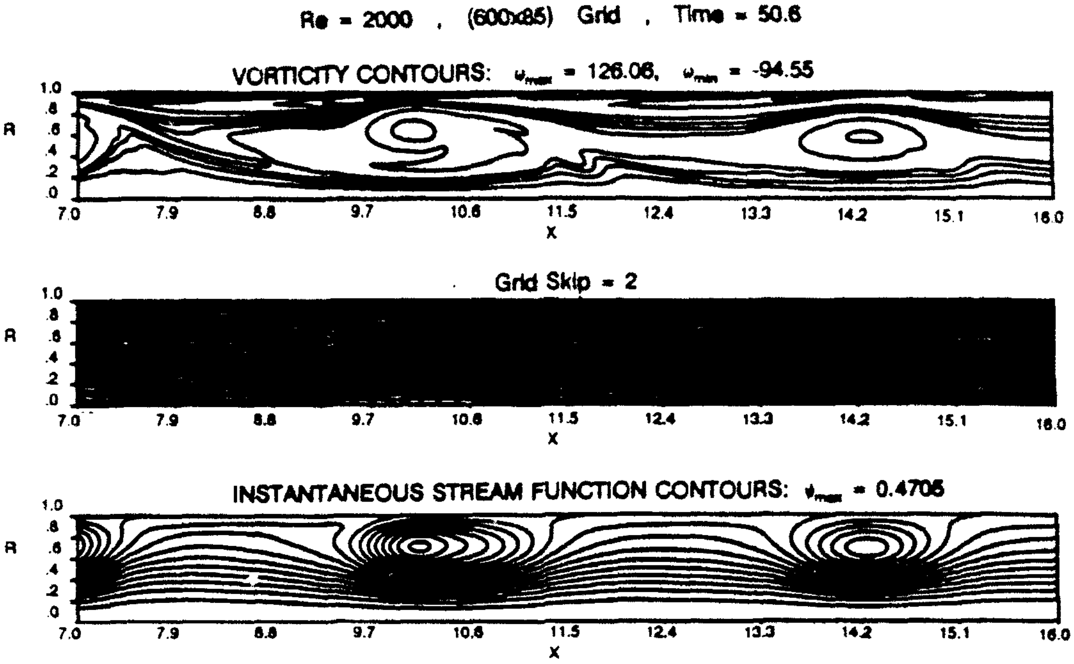
Re = 2000 , (600x85) Grid , Time = 50.6

VORTICITY CONTOURS: ω_{max} = 126.06, ω_{min} = -94.55

Grid Skip = 2

INSTANTANEOUS STREAM FUNCTION CONTOURS: ψ_{max} = 0.4706

d. τ = 50.6.

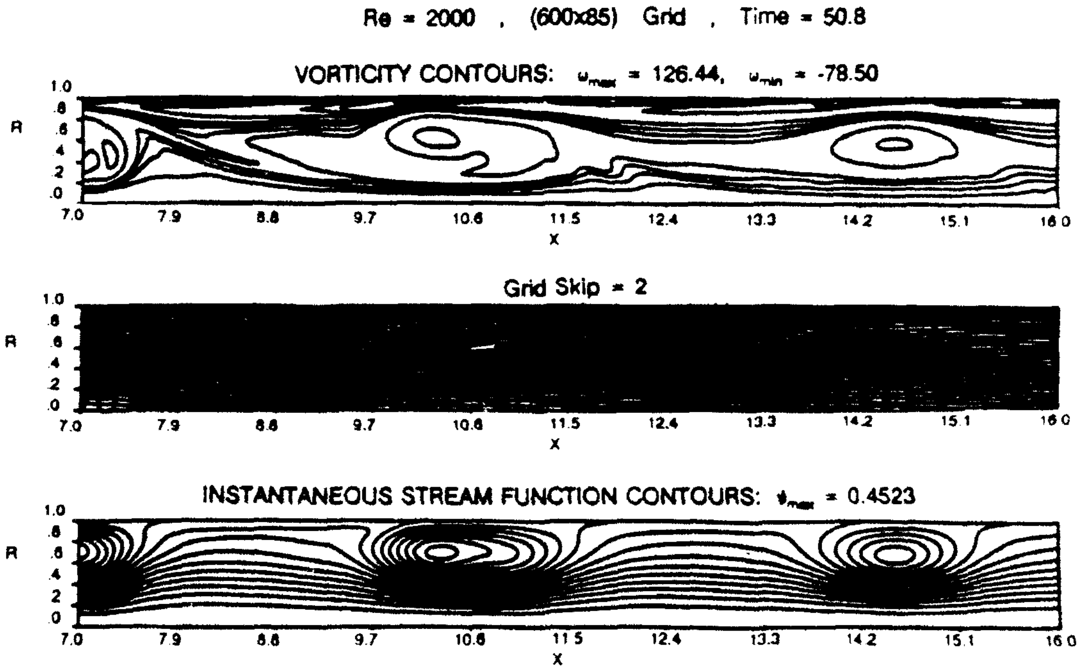
Re = 2000 , (600x85) Grid , Time = 50.8

VORTICITY CONTOURS: ω_{max} = 126.44, ω_{min} = -78.50

Grid Skip = 2

INSTANTANEOUS STREAM FUNCTION CONTOURS: ψ_{max} = 0.4523

e. τ = 50.8.

Figure C.15: Continued.

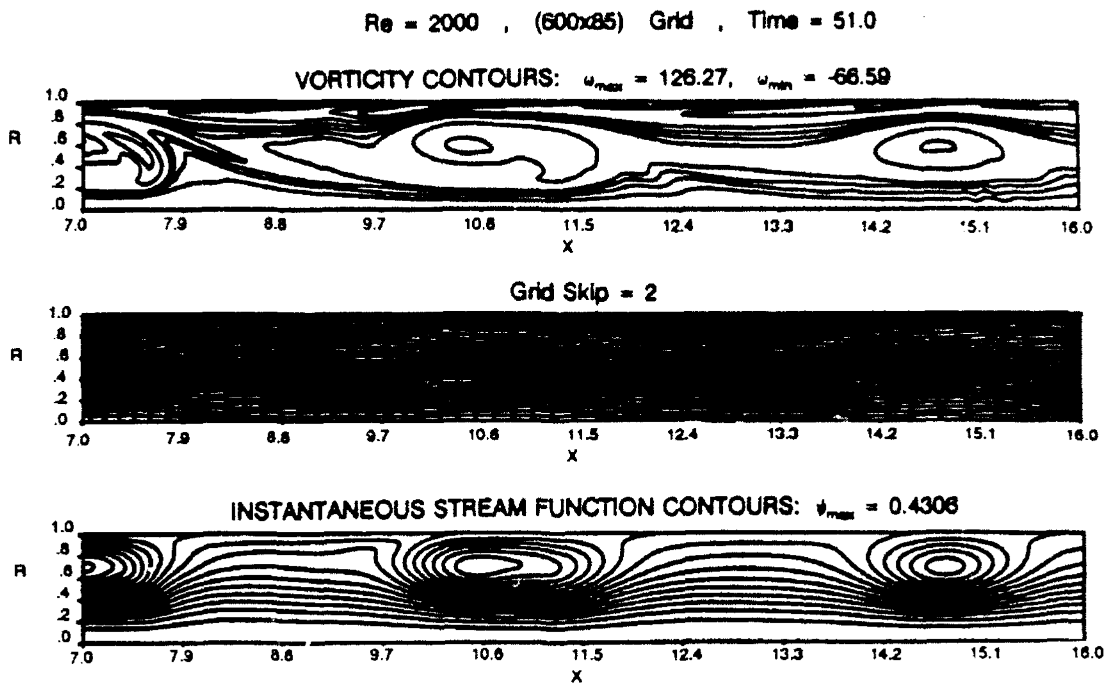

f. τ = 51.0.

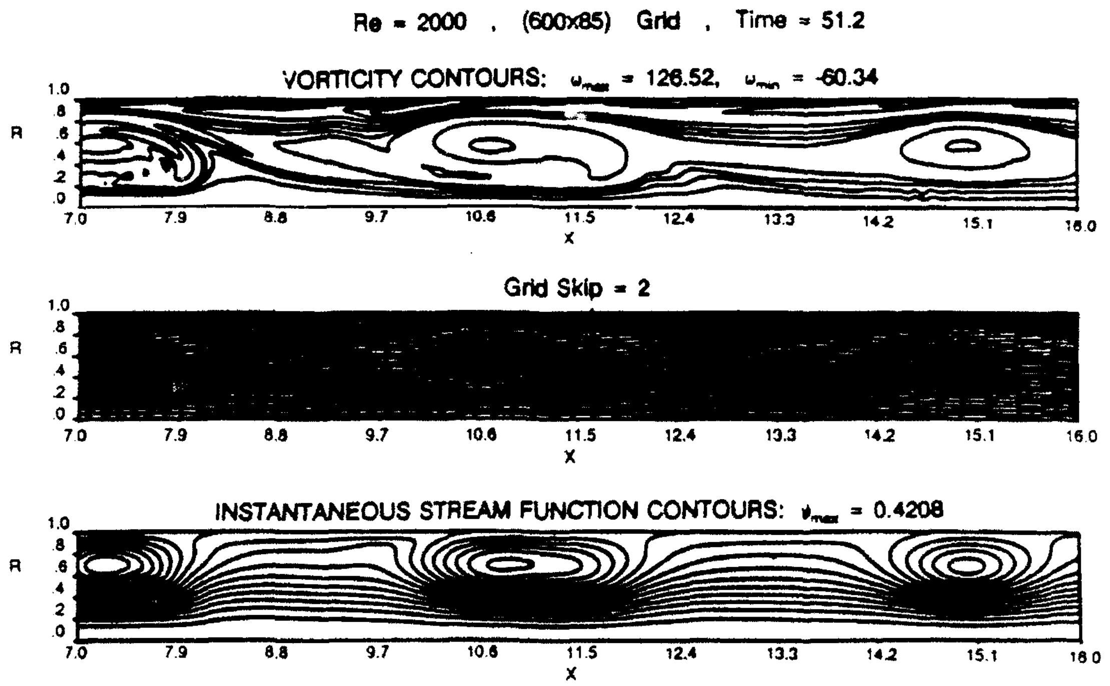

g. τ = 51.2.

Figure C.15: Continued.

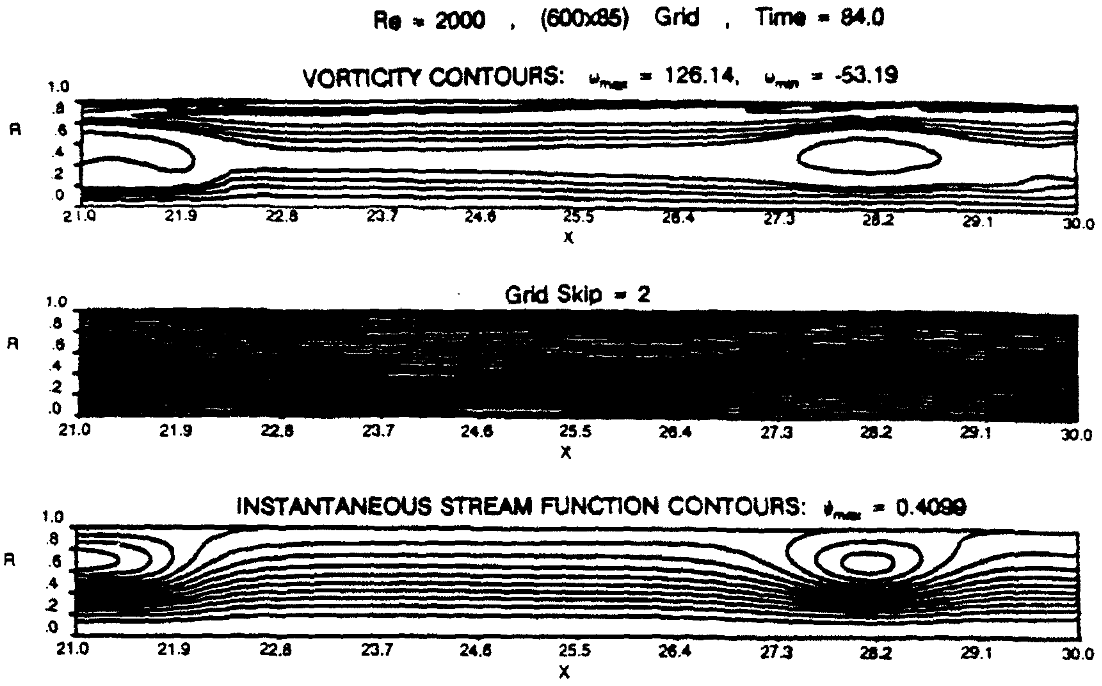

Figure C.16: Flow and adapted grid at outlet. XSL = 2.0, ACR = 0.75, (600 × 85) grid, Re = 2000, time = 84.0.

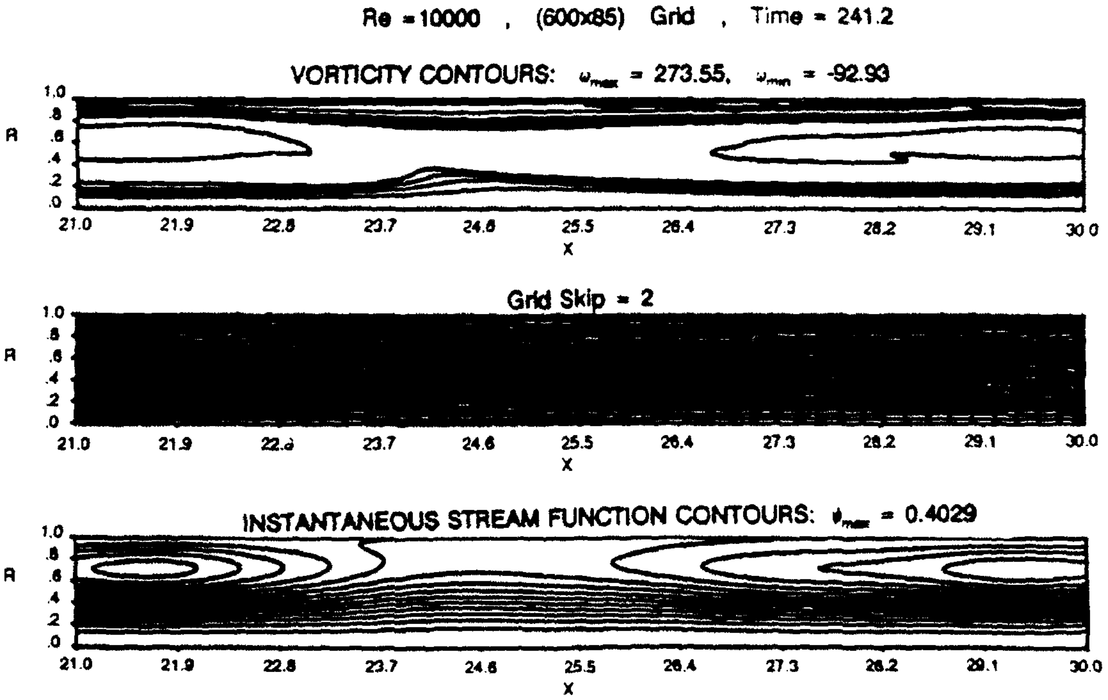

Figure C.17: Flow and adapted grid at outlet. XSL = 2.0, ACR = 0.75, (600 × 85) grid, Re = 10000, time = 241.2.